



TAMPEREEN TEKNILLINEN YLIOPISTO
TAMPERE UNIVERSITY OF TECHNOLOGY

HENRI LIIKANEN
MODELLING, SIMULATION AND PATH-FOLLOWING CONTROL
OF HEAVY-DUTY WHEELED MOBILE ROBOTS

Master of Science Thesis

Examiner: Professor Jouni Mattila
Examiner and topic approved by the
Faculty Council of the Faculty of
Engineering Sciences
on 28th March 2018

ABSTRACT

HENRI LIIKANEN: Modelling, Simulation and Path-Following Control of Heavy-Duty Wheeled Mobile Robots

Tampere University of Technology

Master of Science Thesis, 75 pages, 16 Appendix pages

July 2018

Master's Degree Programme in Automation Technology

Major: Fluid Power Automation

Examiner: Professor Jouni Mattila

Keywords: Path-Following, Wheeled Mobile Robot, Modelling, Simulation, Articulated-Frame-Steering, Hydrostatic Transmission, Bézier, Ponsse Caribou S10, Haulotte 16 RTJ PRO

Autonomous vehicles have been studied at least since the 1950s. During the last decade, interest towards this field of study has grown imposingly. Path-following control is one of the main subjects among autonomous vehicles. The focus in path-following control is in controlling of the pose of the vehicle to match with the desired pose, which is provided by a specified path or trajectory. Usually the pose is represented in a two-dimensional world frame by the means of x and y coordinates and angle of heading.

The methods used in this thesis are modelling and simulation (M&S). M&S of physical systems is a well-recognized field of expertise among engineering sciences. Rapid system prototyping, control designing, or studying an existing system by the means of M&S provide possibilities for observing, developing, and testing under risk-free environment. In this thesis, using the M&S methods provides possibilities for fast and economical evaluation of the designed algorithms before considering prototype testing with actual systems under real environments.

Objectives of the thesis are to implement dynamic robot models of two vehicles, design high-level controller structures for their actuators, implement a path-following controller, and study the behaviour of the robots during various autonomous path-following scenarios. The vehicles to be modelled are Ponsse Caribou S10 and Haulotte 16RTJ PRO. The exact study vehicles are owned by Tampere University of Technology.

Results from closed loop path-following control of the modelled robots denoted accurate path-following under well-behaved path curvatures, generally with a mean absolute lateral position error less than 0.1 m. In the best simulation results, mean position errors were under of 0.05 m. The implemented controllers proved to be effective at the whole velocity range of the forwarder Ponsse Caribou S10. The implemented high-level inverse kinematic controllers succeeded in synchronous commanding of the robots' actuators. Due to the forming of the inverse kinematics, the path-following controller was able to output identical control signals independent of the steering structure of the vehicle, thus permitting a possibility for future development among more advanced path-following control.

TIIVISTELMÄ

HENRI LIIKANEN: Raskaiden pyörällisten mobiilirobottien mallinnus, simulointi ja radanseuranta

Tampereen teknillinen yliopisto

Diplomityö, 75 sivua, 16 liitesivua

Heinäkuu 2018

Automaatiotekniikan diplomi-insinöörin tutkinto-ohjelma

Pääaine: Fluid Power Automation

Tarkastaja: professori Jouni Mattila

Avainsanat: radanseuranta, mobiilirobotti, mallinnus, simulointi, runko-ohjaus, hydrostaattinen ajovoimansiirto, Bézier, Ponsse Caribou S10, Haulotte 16RTJ PRO

Autonominen ajoneuvo on ollut tutkimuksien kohteena ainakin 1950-luvulta lähtien. Viimeisen vuosikymmenen aikana kiinnostus aihealuetta kohtaan on kasvanut huomattavasti. Radanseuranta on yksi autonomiseen ajoneuvon liittyvistä päätutkimusalueista. Keskeisintä radanseurannassa on ajoneuvon sijainnin ja orientaation ohjaaminen vastamaan referenssiarvoja, jotka saadaan generoitavasta reitistä tai radasta. Yleisesti sijainti ja orientaatio esitetään kaksiulotteisessa koordinaatistossa arvoilla x ja y -sijainnit ja suuntakulma.

Työssä käytetyt tutkimusmenetelmät ovat mallinnus ja simulointi. Fysikaalisten järjestelmien mallinnus ja simulointi ovat tunnustettuja osaamisaloja insinööritieteiden keskuudessa. Nopea järjestelmäprototyypin kehittäminen, ohjausjärjestelmän suunnittelu tai olemassa olevan järjestelmän tutkiminen mallintamisen ja simuloinnin avulla mahdollistaa suunnittelun, tarkkailun ja kehityksen riskivapaassa ympäristössä. Tässä työssä kyseisten menetelmien käyttö mahdollistaa algoritmien nopean ja kustannustehokkaan kehittämisen ja arvioimisen ennen niiden käyttöönottoa aidossa järjestelmissä ja ympäristöissä.

Työn tavoitteina on mallintaa kahden ajoneuvon dynaamiset robottimallit, suunnitella korkean järjestelmätason ohjausjärjestelmä niiden toimilaitteille, toteuttaa radanseurantaohjain ja havainnoida robottien käyttäytymistä monipuolisissa radanseurantaolosuhteissa. Mallinnettavat ajoneuvot ovat Ponsse Caribou S10 ja Haulotte 16RTJ PRO. Kyseiset tutkimuksen ajoneuvoyksilöt omistaa Tampereen teknillinen yliopisto.

Simuloidut radanseuranta tulokset osoittivat mallinnettujen robottien tarkkaa radanseuranta kaarteiltaan hyvin suunnitelluilla radoilla, keskimääräisen absoluuttisen lateraalisen virheen ollessa alle 0,1 metriä. Parhaimmissa tuloksissa keskimääräiset virheet olivat alle 0,05 metriä. Toteutettu radanseurantaohjain osoitti tehokkuutensa ajoneuvon Ponsse Caribou S10 koko nopeusalueella. Suunnitellut korkean tason käänteiset kinematiikkaohjaimet onnistuivat robottien toimilaitteiden synkronisessa säädössä. Käänteisten kinematiikkaohjainten implementoinnin ansiosta reitinseuranta-algoritmi pystyi ohjaamaan samoja suureita riippumatta ajoneuvon ohjaustavan rakenteesta, mahdollistaen siten pohjan tulevaisuudessa mahdollisesti kehitettävälle kehittyneemmälle radanseuranta-algoritille.

PREFACE

First, I would like to express my sincere gratitude to Professor Jouni Mattila for providing me a chance to work among such interesting topics, both during the thesis and other projects, and for supervising and examining the thesis. I also want to thank my colleagues and staff at the Laboratory of Automation and Hydraulics for providing a supportive and friendly working atmosphere. Special thanks also go to M. M. Aref for supporting and guiding me at my work.

I want to thank my family, directly speaking, for providing me the best possible environment to grow, learn, and become the person I am now, and for caring and supporting me through all these years. Special thanks also go to my girlfriend for supporting and being there for me during this project and throughout the past years.

Tampere, 26.07.2018

Henri Liikanen

CONTENTS

1.	INTRODUCTION	1
1.1	Modelling and Simulation of Wheeled Mobile Robots	1
1.2	Path-Following of Wheeled Mobile Robots	2
1.3	Methods, Objectives and Structure of the Thesis.....	3
2.	MATHEMATICAL PRELIMINARIES AND MECHANICAL DEFINITIONS....	6
2.1	Kinematics of Different Steering Architectures	6
2.1.1	Articulated-Frame-Steering	7
2.1.2	Two-Wheel Drive and Steering	9
2.1.3	Four-Wheel Drive and Steering	10
2.2	Hydrostatic Power Transmission	11
2.2.1	Main Components	11
2.2.2	Control	13
2.2.3	Dimensioning	14
2.3	Modelling of Hydraulic Components.....	16
2.3.1	Hydraulic Cylinder.....	16
2.3.2	Hydraulic Proportional Valve	18
2.4	Mechanical Steering Structures.....	18
2.4.1	Hydrostatic Wheel Steering	18
2.4.2	Hydraulic Articulated-Frame-Steering	20
2.5	Modelling of Physical Systems in Matlab Simscape Environment	22
2.5.1	Construction Blocks and Physical Connections.....	22
2.5.2	Tire-Terrain Interaction.....	23
2.6	Path-Following Control of Wheeled Mobile Robots	26
2.6.1	Review on Different Path-Following Control Methods.....	26
2.6.2	Nonlinear Path-Following Control Law	28
2.7	Path Generation	30
2.7.1	Cubic Bézier Curves	30
3.	MODELLING OF THE STUDIED SYSTEMS.....	32
3.1	Modular System Architecture	32
3.2	Ponsse Caribou S10.....	33
3.2.1	Hydrostatic Power Transmission	35
3.2.2	Articulation Hydraulics.....	37
3.2.3	Physical Vehicle Model	38
3.3	Haulotte 16RTJ PRO.....	40
3.3.1	Hydrostatic Power Transmission	42
3.3.2	Hydrostatic Wheel Steering	44
3.3.3	Physical Vehicle Model	44
3.4	Implementation of the Path Generator	45
3.5	Path-Following Controller	47
3.6	Inverse Kinematics Controllers.....	48

3.6.1	Articulated-Frame-Steering	48
3.6.2	Car-like Steering	49
4.	SIMULATION STUDIES	51
4.1	Verification of Dynamic Simulation Models	51
4.2	Verification of the Open Loop Control	54
4.3	Closed Loop Control Examination of Path-Following	56
4.3.1	Path-Following on a Well-Behaved Path.....	56
4.3.2	Path-Following with Bounded Steering Actuators	59
4.3.3	High-Speed Path-Following.....	62
4.3.4	Four-Wheel Drive and Steering and Path-Following	65
5.	CONCLUSIONS AND FUTURE WORK	68
	BIBLIOGRAPHY	71

APPENDIX A: PONSSE CARIBOU S10 MAIN DIMENSIONS

APPENDIX B: HAULOTTE 16RTJ PRO MAIN DIMENSIONS

APPENDIX C: PONSSE CARIBOU S10 HIGH-LEVEL MODEL STRUCTURE

APPENDIX D: HAULOTTE 16RTJ PRO HIGH-LEVEL MODEL STRUCTURE

APPENDIX E: PONSSE CARIBOU S10 HYDROSTATIC TRANSMISSION CALCULATIONS

APPENDIX F: OPEN LOOP CONTROL RESULTS

APPENDIX G: CLOSED LOOP PATH-FOLLOWING RESULTS OF PONSSE CARIBOU S10

APPENDIX H: CLOSED LOOP PATH-FOLLOWING RESULTS OF HAULOTTE 16RTJ PRO

LIST OF ABBREVIATIONS AND SYMBOLS

AFS	Articulated-Frame-Steering
COR	Centre of Rotation
CP	Control Point
DOF	Degree of Freedom
IK	Inverse Kinematics
M&S	Modelling and Simulation
PF	Path-Following
PID	Proportional, Integral and Derivative control
POC	Point of Contact
WMR	Wheeled Mobile Robot
2WDS	Two-Wheel Drive and Steering
3D-CAD	Three-Dimensional Computer Aided Design
4WDS	Four-Wheel Drive and Steering

Kinematic parameters

d	distance between wheel centre and control point [m]
$l_f = l_1$	distance between front wheel axle and articulation point [m]
$l_r = l_2$	distance between rear wheel axle and articulation point [m]
L	distance between front wheel axle and control point, wheel-steered vehicle [m]
r	wheel radius [m]
s	path parameter [-]
R	turning radius of the vehicle [m]
v	speed of the control point [m/s]
V	speed of the control point, Articulated-Frame-Steering [m/s]
x	x-coordinate [m]
x_e	longitudinal position error [m]
y	y-coordinate [m]
y_e	lateral position error [m]
$\beta = \gamma$	articulation angle [rad]
\emptyset	angle of heading [rad]
\emptyset_e	heading error [rad]
φ_i	steering angle of the i -th wheel, wheel-steered vehicle [rad]
ω	rate of the heading angle [rad/s]
ω_f	rate of the heading angle of front unit, Articulated-Frame-Steering [rad/s]
\mathbb{Z}_+	subset of positive integers [-]
$\{\mathbf{b}\}$	frame attached to the control point of the robot [-]
$\{\mathbf{d}\}$	reference frame, Frenet-Serret frame [-]
$\{\mathbf{s}\}$	world frame [-]

Hydraulic parameters

A	flow area [m ²]
b	viscous friction coefficient [-]
B_e	effective bulk modulus [Pa]
C_d	viscous friction coefficient [-]
C_f	Coulomb friction coefficient [-]
C_q	flow coefficient [-]
C_s	laminar slip coefficient [-]
e	opening coefficient, hydraulic pump or motor [-]
F_{max}	maximum traction force [N]
F_S	static friction force [N]
F_C	Coulomb friction force [N]
F_μ	friction force [N]
i_g	gear ratio [-]
K	slope of the hyperbolic tangent [-]
K_v	fixed size orifice gain under constant fluid density [-]
L	length of piston stroke [m]
M	moment produced by a hydraulic unit [Nm]
n	rotation speed of a hydraulic unit [r/s]
p	hydraulic pressure [Pa]
P_p	output power of hydraulic pump [W]
Q	hydraulic flow [m ³ /s]
T_m	output torque of hydraulic motor [Nm]
v_s	Stribeck velocity [m/s]
V	volume of a hydraulic component [m ³]
μ	dynamic viscosity coefficient [-]
η_g	efficiency coefficient of gear [-]
η_{hm}	hydro-mechanical efficiency coefficient of a hydraulic unit [-]
η_t	total efficiency coefficient of a hydraulic unit [-]
η_v	volumetric efficiency coefficient of a hydraulic unit [-]
ρ	liquid density [kg/m ³]

Tire-terrain interaction parameters

b	damping coefficient [N/(m/s)]
F_n	normal force [N]
F_f	friction force [N]
k	stiffness coefficient [N/m]
v_{pen}	deformation velocity of the tire [m/s]
v_{poc}	point of contact velocity [m/s]
v_{th}	threshold velocity [m/s]
z_{pen}	deformation of the tire [m]
μ_f	kinetic friction coefficient [-]
μ_s	static friction coefficient [-]

1. INTRODUCTION

1.1 Modelling and Simulation of Wheeled Mobile Robots

Modelling and simulation (M&S) of physical systems is a conventional and rapidly expanding area among engineering sciences. In machine automation and robotics, M&S programs and tools provide the possibilities for developing rapid system prototypes, applying theory to the target system under risk-free simulation environment, and studying the behaviour of the designed control system under specific and various circumstances.

Various mathematical models developed by different authors for M&S of wheeled mobile robots (WMRs) have been presented in a review of four case studies [1]. The implemented models describe the constraints and properties of different steering structures used for controlling the heading and velocity of the WMRs. In the review, authors categorize the WMRs into five classes:

- class (3,0), omnidirectional robots with full mobility.
- class (2,0), zero steerable wheels.
- class (2,1), zero fixed wheels.
- class (1,1), n fixed and n steerable wheels, $n \in \mathbb{Z}_+$.
- class (1,2), zero fixed wheels.

Omnidirectional robots (3,0) possess full mobility. These robots are usually equipped with Swedish or active caster wheels, which provides the possibility for the robot to move in any direction without need for reorientation. Zero steering wheels robots (2,0) have no steerable wheels and the heading of the robot is controlled by varying the velocities of the wheels or tracks on different side of the robot. Both no fixed wheels classes (2,1) and (1,2) share a common feature, where all wheels of the robot are steerable. The difference of the classes is that in (2,1) the number of total wheels must be greater than zero and in (1,2) the robot must have more than one steerable wheel. [1]

Steering structures of these kind of WMRs possess many interesting, advanced and beneficial properties due to the versatile movements they offer. However, the two robots studied and modelled in the study cannot be fully categorized in any of these four classes. Two example WMRs from classes (3,0) and (2,0) are presented in figure 1 on the following page.

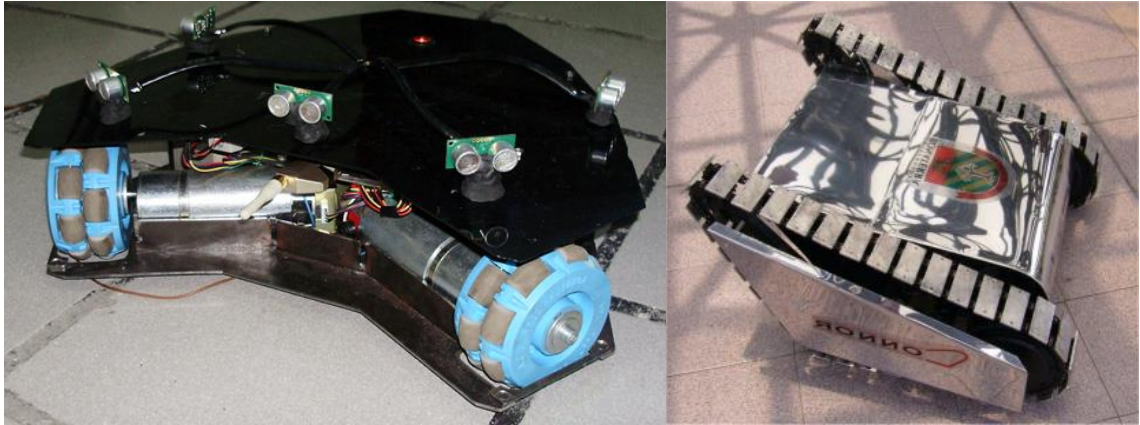


Figure 1: Example WMRs. Class (3,0) omnidirectional robot with Swedish wheels on the left. On the right is a class (2,0) differentially driven robot with zero steerable wheels. [1]

The fifth class of the WMRs presented by the authors in [1] is the class (1,1). These robots have one or several fixed wheels on a common axle and one or several steering wheels on another axle, which is not located at the same location as the fixed wheel axle. The most popular of these kinds of a steering structures is the car-like steering structure, where the front wheels of the vehicle are steerable and rear wheels are fixed. [1]

The wheeled mobile robots studied in the thesis can be categorized into classes (1,1) and (1,2). Although the steering structures of the study robots function differently, they also share common properties, which can be linked to these classes and to nonholonomic constraints. For the sake of clarity, the study vehicles are nonholonomically constrained in a way similar to car-like steering structure, in which the vehicle cannot move sideways without reorienting. Even though the steering structure such as articulated-frame-steering contains only fixed wheels, the properties of the structure function very similar to car-like steering. On the other hand, another one of the studied robots possess a drive mode of four-wheel drive and steering (4WDS), which can be categorized to the class (1,2) of the WMRs.

1.2 Path-Following of Wheeled Mobile Robots

Understanding how different WMRs move with respect to the control inputs they receive is essential in controlling of the robots. In path-following control, the control inputs of the robot's actuators are determined based on the steering structure of the robot. Therefore, the kinematic steering architecture of the robot must be defined before the path-following controller can be designed. Defining the inverse kinematics of different steering structures provides a possibility for designing a generic path-following controller, which is independent of the steering structure of the robot. In this study, these kinematic structures are referred as *inverse kinematics* high-level controllers.

The nonholonomically constrained WMRs of the study can be controlled by the means of two control inputs, linear velocity and rate of heading. High-level schematic presentation of the system to be designed is presented in figure 2. The high-level controllers construct of path-following controller and inverse kinematics of the WMR, as presented in the previous paragraph. Regardless of the structure of the robot, path-follower outputs control signals for the linear velocity and rate of the heading, which depend on the desired input values of the reference path, localization, and structure of the path-follower and its gains.

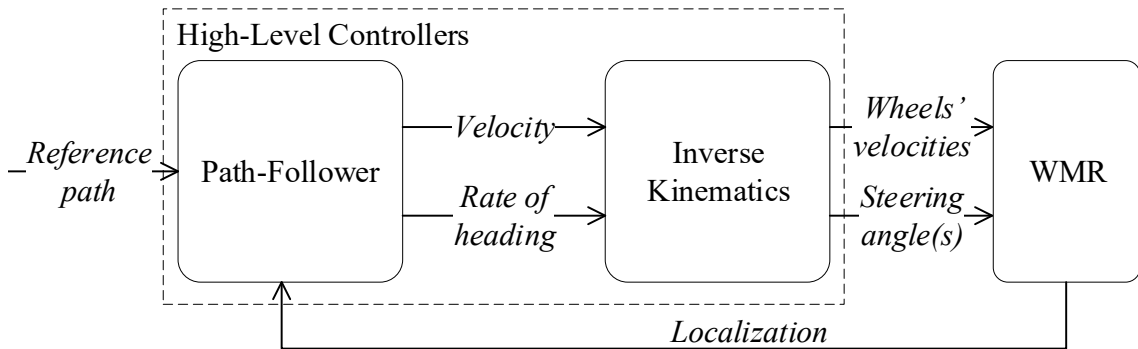


Figure 2: High-level schematics of the control architecture to be designed.

Developing a path-following controller for the robot under M&S environment is a fast way to rapidly prototype the system architecture, test different path following scenarios, and monitor the control response under different circumstances. However, several problems can occur while developing a control structure for real vehicle under simulation environment [2]. Modelling of all physical laws in numerical simulation is extremely hard [2]. During the modelling of dynamic robot models, simplifications must be made to achieve one of the main purposes of M&S, rapid prototyping. Another source of problems are the physical sensors, which in real life may deliver uncertain values and commands for the actuators of the robot, whereas in simulation environment the sensors are almost ideal and extremely robust with a small, or zero, delay.

1.3 Methods, Objectives and Structure of the Thesis

The *methods* used in the study are modelling and simulation. The *objectives* of the study are to create dynamic simulation models for two different wheeled mobile robots using Matlab¹ Simulink and Simscape environments, design high-level inverse kinematic controller structures for their actuators, implement a path-following controller, and study the behaviour of the robots during autonomous path-following. The development phase is executed under simulation environments for fast and economical evaluation of the designed algorithms before prototype testing with the actual systems under real environments.

¹ The official homepage of Matlab: <https://se.mathworks.com/products/matlab.html>

The robots to be modelled represent two vehicles, Ponsse Caribou S10 and Haulotte 16 RTJ PRO, which are presented in figure 3. The forwarder Caribou S10 is a forestry vehicle used for loading, carrying, and unloading logs. Haulotte is a boom lift mainly used for temporary and flexible access purposes during, for example, a maintenance. Both of these vehicles are located at the outdoor laboratory of Tampere University of Technology.



Figure 3: *The vehicles of the study. Haulotte 16RTJ PRO on the left and Ponsse Caribou S10 on the right.*

In the beginning of chapter 2, background theories of different steering kinematics are presented. Kinematic models used for describing different steering structures have been presented and developed at least since the 1990s [3, 4]. The focus in kinematic level is to study and implement inverse kinematics for two different steering structures. Inverse kinematics function as high-level controllers adjusting the control commands for driving and steering actuators of the robot.

Modelling of the vehicles' internal driving and steering dynamics is one of the main objectives of the thesis. This type of modelling provides more realism and added value to the simulation results gained from the path-following control of the study vehicles. By this, all driving and steering joints of the physical robot receive either torque or force as an input, instead of straight, robust, and instantaneous angular velocity control commands.

The power transmissions of both study vehicles are implemented by using hydrostatic transmissions (HSTs). Use of HST in heavy-duty vehicles is justified for its great power-weight relation and good efficiency [5, 6]. The theories behind hydrostatic transmission, its components and control, are presented in section 2.2. In the following section 2.3, mathematical preliminaries for modelling of hydraulic cylinders and valves are presented. These models are used for providing power and control for different mechanical steering

structures. Mechanical and hydraulic architectures of the steering structures of the study vehicles are presented in section 2.4.

Physical models of the vehicles are designed in Matlab Simscape environment. Simscape environment provides tools for rapid modelling of advanced physical systems. Simscape provides also visualization features, which can be easily used for observing the behaviour of the modelled system. Fundamental principles of modelling physical systems using Matlab Simscape environment are presented in section 2.5.

Design of path-following control for wheeled mobile robots is another one of the main objectives of the thesis. A short literature review on different path-following methods is conducted in section 2.6. After the review, the path-following controller implemented and used in the thesis is derived. In section 2.7, the main principles of path generation are presented. While the path generation is not considered in detail in this thesis, it is, however, a crucially needed factor for producing smooth and exact paths for the robots to follow.

The modelling of the complete system is conducted in chapter 3. The dynamic vehicle models and their internal dynamics and powering systems are the first subjects to be discussed. After deriving the vehicle models, implementations of the path generator and path-following controller are presented, followed by the implemented inverse kinematics controllers of different steering architectures.

Verification and validation of the models is conducted in chapter 4. In the chapter, open loop scenarios are being driven to observe the open loop control of the HSTs and the results are compared to well-known mathematical theories, previous publications and technical properties reported by the manufacturers. Next, properties and behaviour of the low-level actuators control is monitored by the means of three specific open loop path following scenarios. After these verifications, the path-following controller is enabled, and several closed loop path-following cases are being driven to observe the behaviour of the robots under different scenarios.

Conclusions and proposals for upcoming future work are presented in the end of the study in chapter 5. First, a concise summary concerning the structure of the thesis is drawn. Next, the main outcomes of the thesis are discussed, followed by the key points suggested to be focused on in the future research and development. Finally, the ending paragraph summarizes the main achievements and concludes the thesis.

2. Mathematical Preliminaries and Mechanical Definitions

2.1 Kinematics of Different Steering Architectures

Different steering structures require different kinematic equations for describing the motions of the WMRs correctly. However, all nonholonomic WMRs with constrained centre of rotation (COR) possess the same property of differential drive [7]. In differential drive, the driving wheels of the vehicle are set to be perpendicular with respect to the COR. With this kind of kinematic constraint, the linear velocities of the driving wheels can be presented as illustrated in figure 4, where the heading angle θ is the angle between the velocity vector v and x-axis of the world frame $\{s\}$. [7]

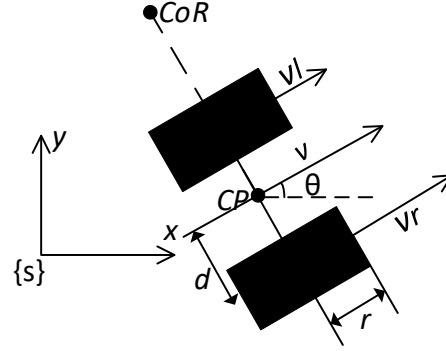


Figure 4: Illustrating figure of the principle of differential drive.

According to [7], the angular wheel velocities with respect to the linear velocities of v_l and v_r in differential drive can be presented as a function of control point's (CP) linear velocity (v), rate of the heading ($\dot{\theta}$), the distance d between the CP and the centre of the wheel, and the wheel radius r

$$\begin{bmatrix} u_l \\ u_r \end{bmatrix} = \begin{bmatrix} \frac{v - \dot{\theta}d}{r} \\ \frac{v + \dot{\theta}d}{r} \end{bmatrix}. \quad (2.1)$$

The presented equation is dominantly used in deriving wheel velocities throughout the thesis. Another key feature based on constrained COR is the calculation for the turning radius, which can be respectively presented as a ratio of the linear velocity and rate of the heading

$$R = \frac{v}{\dot{\theta}}. \quad (2.2)$$

Determining the minimum turning radii for the robots is vital when the command limitations of path-following control are to be considered, as will be presented in section 3.5.

2.1.1 Articulated-Frame-Steering

Different methods for describing the steering kinematics of articulated-frame-steering (AFS) vehicles have been presented at least since the 1990s. One of the first presented steering models for describing articulation kinematics is called the bicycle model [3]. The bicycle model is derived under assumption of no slipping and rolling motion constraints of nonholonomic robots are considered. According to [3], the equations for calculating the derivatives of the time depended Cartesian coordinates x , y , and heading ϕ can be expressed as

$$\begin{bmatrix} \dot{x}(t) \\ \dot{y}(t) \\ \dot{\phi}(t) \end{bmatrix} = \begin{bmatrix} V \cos(\phi) \\ V \sin(\phi) \\ \frac{v \tan(\frac{\gamma}{2})}{l} \end{bmatrix} \quad (2.3)$$

where γ presents the articulation angle, V is the speed of the control point, and $l = l_1 = l_2$ is the distance between the wheel axles and articulation point. For these equations to be respectfully valid, the articulation angle and velocity of the vehicle are assumed to be constant, and the distances between the wheel axles and articulation point to be equal. [3]

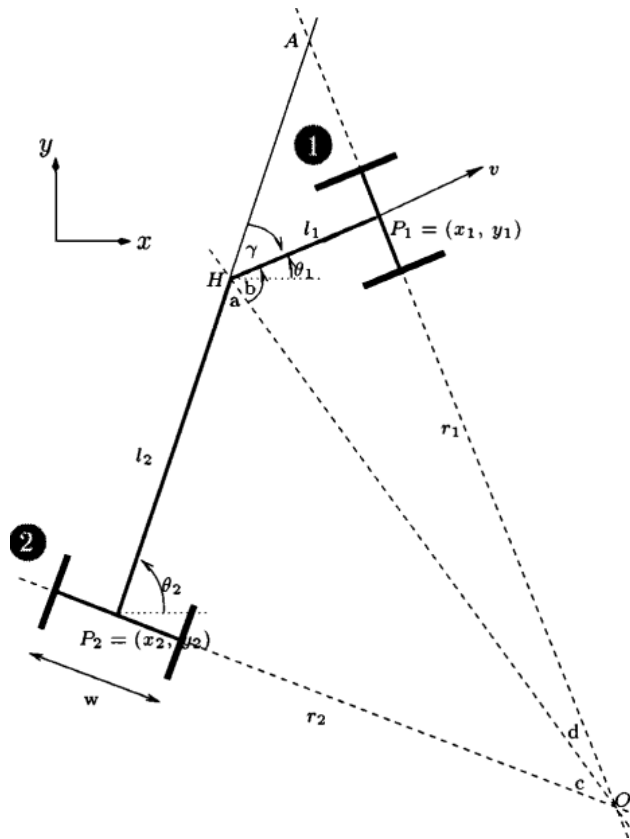


Figure 5: Steering kinematics of articulated frame steering. [3]

In the papers [4] and [8], a steady-state models for AFS were presented, which included the possibility of a nonsymmetric vehicle. During a steady-state steering with constant velocity and steering rate, the two halves of the vehicle will follow circles with different radii, as illustrated in figure 5. Radii can be presented as a function of the articulation angle γ , and lengths l_1 and l_2 as

$$R_1 = \frac{l_1 \cos(\gamma) + l_2}{\sin(\gamma)} \quad (2.4)$$

$$R_2 = \frac{l_2 \cos(\gamma) + l_1}{\sin(\gamma)}. \quad (2.5)$$

A more developed kinematic model for AFS is proposed by the authors in [9] and [10]. The configuration for presenting the movements of the front unit in the proposed kinematic model can be summarized with following equations

$$\begin{bmatrix} \dot{\phi} \\ \dot{x} \\ \dot{y} \end{bmatrix} = \begin{bmatrix} 0 & 1 \\ \cos \varphi & 0 \\ \sin \varphi & 0 \end{bmatrix} \begin{bmatrix} v_f \\ \omega_f \end{bmatrix} \quad (2.6)$$

$$\omega_f = \frac{l_r \dot{\beta} + v_f \sin \beta}{l_f \cos \beta + l_r} \quad (2.7)$$

where ω_f and v_f are the rate of the heading angle and speed of the front unit, respectively, β is the articulation angle of the vehicle, and l_f and l_r are the distances between front and rear wheels axles and the articulation joint, respectively. The presented properties are illustrated in figure 6.

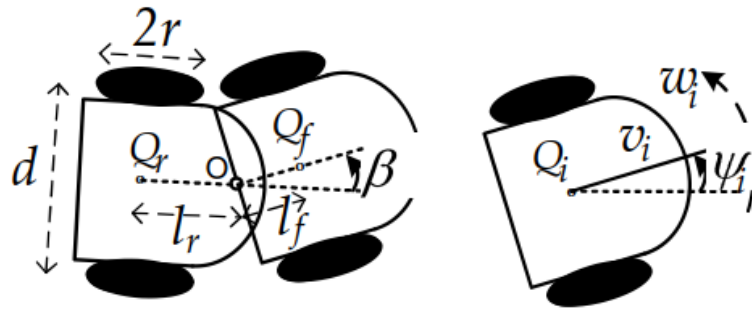


Figure 6: One of the proposed methods for kinematic structure of AFS. [9]

The effect of the rate of articulation is considered in the previous equations. According to the equation, the rate of the front unit's heading is depending on the rate of the articulation and velocity of the vehicle. In practice, with higher velocities and rate of the articulation, wheel slippage is increasing, which affects to the heading rate quite significantly. In steady state, the equation is similar to the previously presented bicycle model. [9]

2.1.2 Two-Wheel Drive and Steering

Car-like steering is the most common steering structure in the world. Typically, in car-like steering the front wheels of the vehicle are steered to achieve the desired heading direction. Bicycle model is one of the most commonly used model to describe car-like steering kinematics. The model is based on Ackermann steering [7]. In Ackermann steering, the steering angle of the wheel inside the turn is controlled to have a value larger than the steering angle of the wheel outside the turn. The principle is used to prevent tire slippage in cornering situations where the wheels follow circular paths with different radii.

The most important kinematic constraint to be satisfied, especially in the bicycle model of car-like steering, is to maintain identical COR for all wheels. For front wheel-steered vehicle, the COR is usually selected to be perpendicular with respect to rear wheels axle of the vehicle. As illustrated in figure 7 below, the Ackermann steering with this type of COR constraint is presented. Coordinate frame $\{s\}$ represents the world frame. [7]

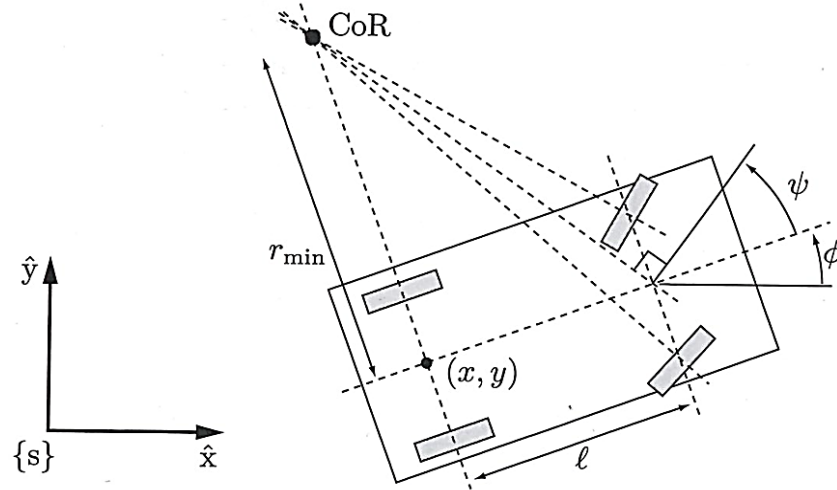


Figure 7: Illustrating figure of the bicycle model with Ackermann steering. [7]

According to [7], when the COR is constrained to be perpendicular with respect to the rear wheels axle of the vehicle, the simplified kinematics for car-like steering structure can be written as

$$\dot{q} = \begin{bmatrix} \dot{\phi} \\ \dot{x} \\ \dot{y} \\ \dot{\phi} \end{bmatrix} = \begin{bmatrix} (\tan \phi)/L & 0 \\ \cos \phi & 0 \\ \sin \phi & 0 \\ 0 & 1 \end{bmatrix} \begin{bmatrix} v \\ \omega \end{bmatrix} \quad (2.8)$$

where v and ω are speed and heading rate of the control point (x, y) , respectively, ϕ is the steering angle of the virtual middle wheel, and L is the distance between the CP and front wheel axle of the vehicle. When the steering angle of the virtual wheel is known, the steering angles of left and right front wheels can be presented by using simple geometry

$$\varphi_r = \begin{cases} \operatorname{atan} 2 \left(\frac{\dot{\phi}L}{v+d\dot{\phi}} \right), \dot{\phi} > 0 \\ \operatorname{atan} 2 \left(\frac{\dot{\phi}L}{v-d\dot{\phi}} \right), \dot{\phi} < 0 \end{cases} \quad (2.9)$$

$$\varphi_l = \begin{cases} \operatorname{atan} 2 \left(\frac{\dot{\phi}L}{v-d\dot{\phi}} \right), \dot{\phi} > 0 \\ \operatorname{atan} 2 \left(\frac{\dot{\phi}L}{v+d\dot{\phi}} \right), \dot{\phi} < 0. \end{cases} \quad (2.10)$$

When calculating the steering angles separately for both front wheels, the signum of the heading rate must be considered as shown. [7]

2.1.3 Four-Wheel Drive and Steering

For four-wheel drive and steering (4WDS), one of the easiest ways to locate and constraint the COR is to set it perpendicular with respect to the middle point of the longitudinal axle of the vehicle. By this way, the steering angles for front wheels can be derived similarly compared to the bicycle model, and the steering angles of the rear wheels are mirrored with respect to these angles. [11] The derived kinematic structure of the symmetrical 4WDS is presented in figure 8.

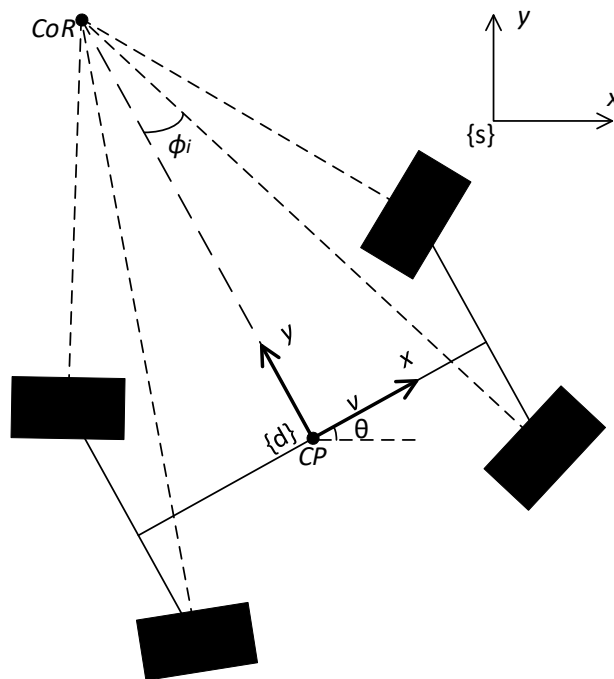


Figure 8: *Steering kinematics of four-wheel steering with constrained COR.*

For the symmetrically mirrored four-wheel drive and steering, the kinematics can be presented by using equations of the bicycle model (2.8), (2.9), and (2.10). However, the steering angles of the front wheels are now calculated by using the distance between front wheels and the new control point set in the middle of the longitudinal axle. [11]

2.2 Hydrostatic Power Transmission

2.2.1 Main Components

Hydrostatic transmission (HST) is widely used in mobile working machines due to its multiple beneficial features, such as great power-weight relation, freedom in designing system layouts, and accurate and smooth positioning of hydraulic actuators. Hydrostatic transmission generally consists of three main components: diesel engine, hydraulic variable displacement pump, and hydraulic variable displacement motor. [5] An illustrating figure of hydrostatic transmission, and operating variables and parameters of different components are presented in figure 9.

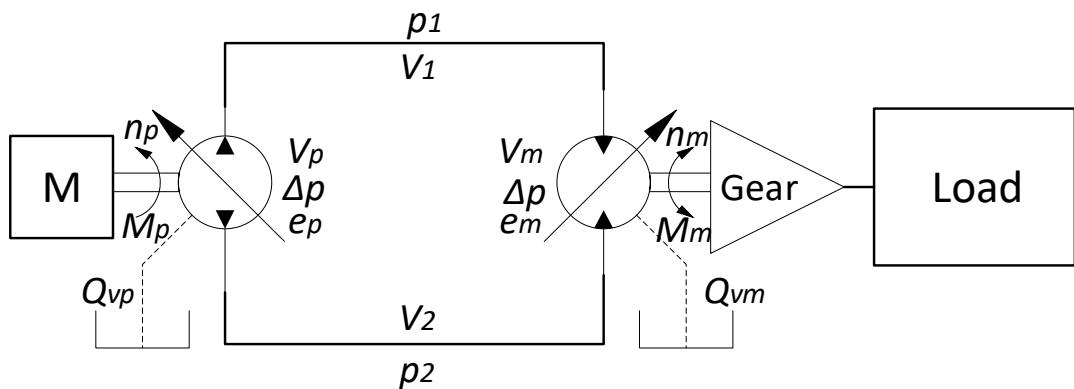


Figure 9: Main principles figure of a closed circuit hydrostatic transmission system. Structure of the figure is adapted from [5].

The most common types of hydraulic pumps and motors used in HST are axial piston pumps with variable displacement. The displacement of the pump or motor is usually adjusted by tilting the swashplate. In bent axis type units, the displacement is varied by swivelling the cylinder barrel. Hydraulic pump and motor are joined together with hydraulic hoses. Usually in a system analysis, the volumes V_1 and V_2 of the hoses are assumed to be equal and the pressure in the low-pressure side of the circuit to be constant. [5, 6]

Variable Displacement Units

According to the author in [5], equations for describing the flow and torque produced by the variable displacement hydraulic pump can be presented as

$$Q_p = e_p V_p n_p - Q_{vp} \quad (2.11)$$

$$M_p = e_p \Delta p_p \frac{V_p}{2\pi} + M_{hp} \quad (2.12)$$

where V_p is the maximum displacement of the pump, n_p is the rotational speed of the pump, Δp_p is the pressure difference over the pump, and e_p is a coefficient for describing

the displacement of the pump in range of $[-1,1]$. Functions Q_{vp} and M_{hp} are used for describing the flow and torque losses, respectively. [5]

Equations describing the input flow and the torque produced by the hydraulic motor can be presented similarly compared to hydraulic pump

$$Q_m = e_m V_m n_m + Q_{vm} \quad (2.13)$$

$$M_m = e_m \Delta p_m \frac{V_m}{2\pi} - M_{hm} \quad (2.14)$$

where V_m is the maximum displacement of the motor, n_m is the rotational speed of the motor, Δp_m is the pressure difference over the motor, and e_m is a coefficient for describing the displacement of the motor in range of $[-1,1]$. Flow and torque losses of the motor are presented by using functions Q_{vm} and M_{hm} . [5]

In this study, the losses for flow and torque are defined by using Wilson's models presented in the study of Huhtala [5]. The loss in the hydraulic flow produced by the pump can be presented as a function of the pressure difference over the pump

$$Q_{vp} = C_s \frac{V_p \Delta p_p}{2\pi\mu} + Q_R \quad (2.15)$$

where μ is the dynamic viscosity of the fluid, C_s is the laminal slip coefficient, and Q_R is the constant leakage flow. In this study, previously presented coefficients are defined according to sources [5] and [6].

Torque losses present in hydraulic units according to Wilson can be separated into three distinct categories: Coulomb friction, dry friction, and constant friction. Equation proposed by Wilson to describe these losses in a hydraulic pump can be presented as

$$M_{hp} = C_f \frac{V_p \Delta p_p}{2\pi} + C_d \mu V_p n_p + M_c \quad (2.16)$$

where C_f is the Coulomb friction coefficient, C_d is the viscous friction coefficient, and M_c is the constant torque loss. Friction coefficients implemented in the study are defined based on research in [6].

Previously presented equations are formed for describing the losses of hydraulic pump. Due to the similarities of the pump and motor, they can be considered as similar hydraulic units, but with opposite directions of operation. Therefore, the previously presented losses for flow and torque function similarly with both components, but with opposite directions of effect, as it is presented by using the signs before the terms Q_{vp} , Q_{vm} , M_{hp} and M_{hm} introduced in the previous equations (2.11-2.14).

Pressure Lines

According to [5], the rate of the pressure change in the high-pressure line of the closed hydraulic circuit \dot{p} , and the pressure difference over the hydraulic pump and motor Δp are based on following equations

$$\dot{p} = \frac{B_e}{V_1} (Q_p - Q_m) \quad (2.17)$$

$$\Delta p = \int \dot{p} dt - p_{low} \quad (2.18)$$

where B_e is the bulk modulus of the hose, V_1 is the volume of the hose, and Q_p and Q_m represents the hydraulic flows entering and leaving the hose, respectively. The system pressure in the low-pressure side of the closed circuit is described by p_{low} term. [5]

Auxiliary Components

In addition to the three main components, HST system contains many auxiliary components. The main pump usually contains an auxiliary pump, which is used for compensating the leakages in the closed circuit and provide the flow for controlling the displacement of the hydraulic pump. HST contains also other components, such as flushing and pressure relief valves, tank, and heat exchanger, which is being used to cool down the fluid entering the closed circuit. [5, 6]

2.2.2 Control

Before dimensioning of HST, the control strategy which is used for controlling the HST is to be considered. Two different, yet straightforward, control strategies widely used in the mobile industry are called traditional control and secondary control. Similar in both control methods is that the rotation speed of the diesel engine is strived to be held constant, while the displacements of either the hydraulic pump or motor are being varied. [5] The author in [5] describes also a third control strategy called adaptive control, where the running speed of the diesel engine is also controlled. However, the adaptive control strategy of HST is left out of the scope of this thesis.

Traditional Control

Traditional control of HST focuses on constraining the rotation speed of the diesel engine at certain value. When the engine speed is constant, the rotation speed of the pump is constant, and the velocity of the vehicle is controlled by controlling the displacements of the hydraulic pump and motor. The principles of the traditional control are illustrated in figure 10 on the following page. [5, 6]

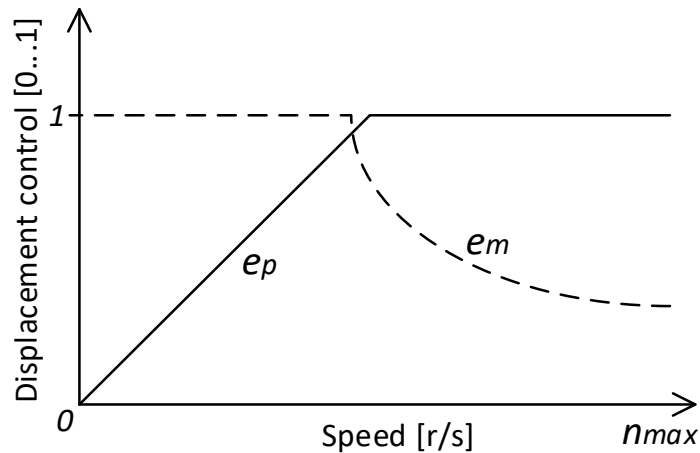


Figure 10: Traditional control of HST.

At the start of the movement, the displacement of the hydraulic pump e_p is increased, while the motor is at its maximum displacement. When the pump has achieved its maximum displacement, the displacement of the motor e_m is decreased, until the desired velocity of the vehicle is achieved. As presented in the figure, the displacement of the pump is linearly controlled, and the displacement of the motor is controlled with inverse relation with respect to the speed. [6]

Secondary Control

Secondary control is the best control strategy for achieving best dynamic response due to small moving inertia. In secondary control, the hydraulic pump is controlled to maintain a specific constant system pressure, and the speed of the vehicle is controlled by adjusting the displacement of the motor. The displacement of the motor is not proportional to the speed of the vehicle, but to the torque needed from the shaft of the motor. In practice, this implies that when the vehicle is moving with same velocity on a flat surface and during hill climb, the displacement of the motor is different and proportional to the needed motor's shaft torque. [5, 6]

2.2.3 Dimensioning

According to the author in [12], conversion ratio of the HST system is the first parameter to be considered in dimensioning of HST driveline. Conversion ratio indicates whether the HST can be designed with a fixed hydraulic motor or is a variable displacement motor needed for the system to achieve the desired traction force and maximum velocity with given system input power. The calculation of conversion ratio R is based on equation

$$R = \frac{v_{max} F_{max}}{P_p \eta_g \eta_{t,p} \eta_{t,m}} \quad (2.19)$$

where v_{max} and F_{max} are the desired maximum velocity and traction force of the vehicle, P_p is the available output power of the hydraulic pump, η_g is the efficiency coefficient of the gear ratio between hydraulic motor and the wheels, and $\eta_{t,p}$ and $\eta_{t,m}$ are total efficiency coefficients of hydraulic pump and motor, respectively. For a conversion ratio greater than 3:1, a variable displacement motor must be considered to fulfil the desired maximum traction force and velocity. An illustrating figure of the corner power theory is presented below. [12]

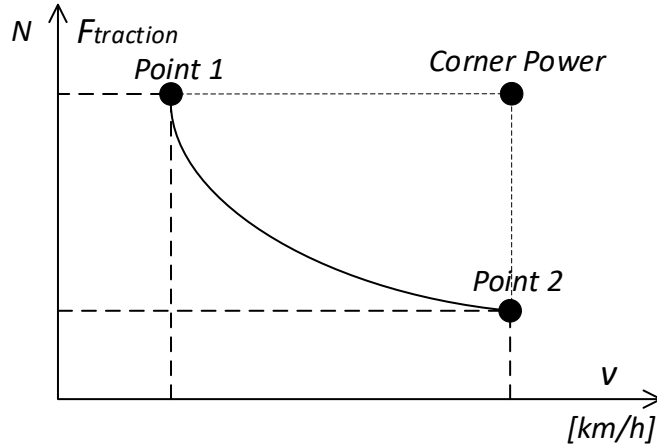


Figure 11: Illustrating figure of the Corner Power Theory. [12]

According to [12], when the corner power is known, the main hydraulic pump and motor can be dimensioned with equations

$$V_{gp} = \frac{v_{max} F_{max}}{n_p \Delta p_{max} \eta_{t,p} \eta_{t,m} \eta_g R_m} \quad (2.20)$$

$$V_{gm} = \frac{F_{max} 2\pi r_{wheel}}{\Delta p_{max} \eta_{hm} i_g \eta_{gear}} \quad (2.21)$$

where Δp_{max} is the maximum pressure level of the system, v_{max} and F_{max} are the desired maximum velocity and traction force, R_m is the calculated conversion ratio of the hydraulic motor, r_{wheel} is the radius of the wheel of the vehicle, n_p is the rotation speed of the pump at maximum velocity, and i_g is the gear ration between the hydraulic motor and the wheels of the vehicle. [12]

With traditional HST control, the nominal values in point 1 of the figure 11 for the flow rate $Q_{p,p1}$ and displacement of the pump $V_{gp,p1}$, rotational speed of the hydraulic motor $n_{m,p1}$, torque produced by the hydraulic motor $T_{m,p1}$, and maximum velocity of the vehicle at maximum traction force $v_{max,p1}$ are, respectively, based on following equations

$$Q_{p,p1} = \frac{P_p}{\Delta p_{max}} \eta_{t,p} \quad (2.22)$$

$$V_{gp,p1} = \frac{Q_{p,p1}}{n_p \eta_{v,p}} \quad (2.23)$$

$$n_{m,p1} = \frac{Q_{p,p1} \eta_{v,m}}{V_{gm}} \quad (2.24)$$

$$T_{m,p1} = \frac{V_{gm} \Delta p_{max}}{2\pi} \eta_{hm,m} \quad (2.25)$$

$$v_{max,p1} = \frac{n_{m,p1} 2\pi r_{wheel}}{i_g} \quad (2.26)$$

Similar performance values of the HST and the vehicle at point 2 with traditional control can be summarized with equations

$$Q_{p,p2} = V_{gp} n_p \eta_{v,p} \quad (2.27)$$

$$\Delta p_{p2} = \frac{P_p \eta_{t,p}}{Q_{p,p2}} \quad (2.28)$$

$$V_{gm,p2} = \frac{Q_{p,p2} \eta_{v,m}}{n_{m,p2}} \quad (2.29)$$

$$T_{m,p2} = \frac{V_{gm,p2} \Delta p_{p2}}{2\pi} \eta_{hm,m} \quad (2.30)$$

$$F_{max,p2} = \frac{T_{m,p2} i_g \eta_g}{r_{wheel}} \quad (2.31)$$

where in addition to equations of point 1 $V_{gm,p2}$ is the displacement of the hydraulic motor, Δp_{p2} is the pressure difference over the motor, and $F_{max,p2}$ is the maximum available traction force at maximum velocity of the vehicle. [12]

2.3 Modelling of Hydraulic Components

2.3.1 Hydraulic Cylinder

Mathematical model of a hydraulic cylinder constructs of two volume models. Volume model is the part of a hydraulic system, in which the pressure can be assumed to be equal at each point, for example, in a chamber of hydraulic cylinder. [13]

In subsection 2.2.1, volume for the high-pressure hose of HST was defined with equations (2.17) and (2.18), where the rate of the pressure was defined based on volume and bulk modulus of the hose, and the difference between the flows entering and leaving the hose. Quite similarly to the previously described, the author in [13] presents a universal state equation for the volume as

$$\frac{dp}{dt} = \frac{B_{eff}}{V} \left(\sum Q - \frac{dV}{dt} \right) \quad (2.32)$$

where B_{eff} is the effective bulk modulus of the volume V , $\frac{dV}{dt}$ is the change of the volume with respect to time, and $\sum Q$ is a sum of the flows entering and leaving the volume. Functionalities of the equation can be summarized in a following way:

- $\sum Q > \frac{dV}{dt} \rightarrow \text{Pressure increases}$
- $\sum Q < \frac{dV}{dt} \rightarrow \text{Pressure decreases}$
- $\sum Q = \frac{dV}{dt} \rightarrow \text{Volume is in equilibrium} \rightarrow Q = vA$

As conclusion, the difference between the flow entering the circuit and in rate of volume change defines the behaviour of the pressure inside the volume. When the difference is zero, volume is in equilibrium, and the well-known equation for continuity stands. [13]

In addition to previously described, a friction model to describe the losses present in hydraulic cylinder is usually implemented into the cylinder model. According to [13], when crawling of the cylinders is not an issue, as it is not in the steering structures of the study, a hyperbolic friction model presented in equation (2.33) can be used. This model is popularly used with hydraulic cylinders due to its simplicity, and therefore more efficient calculation properties [13].

$$F_{\mu} = \tanh(K\dot{x}) \left(F_C + (F_S - F_C)e^{-\left(\frac{\dot{x}}{v_s}\right)^2} \right) + b\dot{x} \quad (2.33)$$

In the equation, F_S and F_C represent static and Coulomb friction forces, v_s is a Stribeck velocity, b is a viscous friction coefficient, and K is the slope of the hyperbolic tangent. Velocity of the cylinder in the equation is marked as \dot{x} . [13]

In defining of the various friction parameters, datasheets of the different hydraulic components have proven to be insufficient [13]. According to [13], certain thumb rules for defining the friction model parameters can be used:

- Static friction is approximately 5-10 % of the maximum force of the cylinder
- Coulomb friction is approximately 10-40 % smaller than static friction force
- Viscous coefficient in [Ns/m] is approximately same as unit value of static friction
- Minimum friction presents at velocity approximately between 3 and 15 mm/s
- Hyperbolic gain is usually set between 2000-20000

The friction parameters for the cylinder models of the study are defined according to these guide lines combined with empirical observations on the system behaviour.

2.3.2 Hydraulic Proportional Valve

Modelling of proportional valve is based on modelling of the ports of the valve. Ports can be modelled as orifices. Orifice is a section in the flow path, which has a certain cross-sectional area significantly smaller than on the rest of the path. In the following equation and modelling of the study, flow through the orifice can be either laminar or turbulent, depending on the pressure magnitude. Based on [13], the flow through the orifice can be written as

$$Q = \begin{cases} K_v \operatorname{sgn}(p_1 - p_2) \sqrt{|p_1 - p_2|} & , |p_1 - p_2| > p_{tr} \\ \frac{K_v(p_1 - p_2)}{2\sqrt{p_{tr}}} \left(3 - \frac{|p_1 - p_2|}{p_{tr}} \right) & , |p_1 - p_2| \leq p_{tr} \end{cases} \quad (2.34)$$

where $|p_1 - p_2|$ represents the absolute value of the pressure difference over the orifice and K_v is the gain for fixed size orifice under constant fluid density. The gain is based on equation

$$K_v = C_q A \sqrt{\frac{2}{\rho}} \quad (2.35)$$

where C_q is the flow coefficient, A is the area of the orifice, and ρ is the density of the liquid. The flow coefficient is usually approximated between 0.6 and 0.8. [13]

In the equation (2.34), the signum calculated from the pressure difference provides the possibility for the flow to move towards both possible directions. Transient pressure p_{tr} defines the pressure level from which the higher pressure difference causes the flow to be turbulent and in lower pressure levels the flow can be considered to be laminar. [13]

Dynamics of the valve are approximated using 2nd order transfer function and transport delay. Characteristic angular velocity, damping, and the delay between control and spool movement are parameters, which are usually experimentally separately defined for each valve type. The delay of the valve is usually defined by step response measurements. [13] In this study, these parameters are empirically tuned until respectively valid behaviour from the component is achieved.

2.4 Mechanical Steering Structures

2.4.1 Hydrostatic Wheel Steering

Hydrostatic steering is widely used in heavy-duty mobile industry. Steering is usually implemented with one or two hydraulic cylinders. The cylinders are connected to a mechanical structure, which transmits the steering to the wheels of the vehicle as a function of the cylinders' displacements. [14]

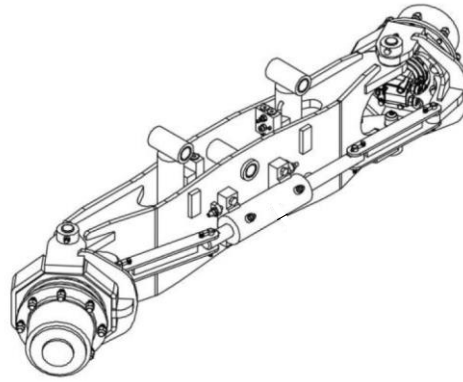


Figure 12: Steering cylinder and mechanism of Haulotte 16RTJ PRO. [15]

In one of the study vehicle, Haulotte 16RTJ PRO, steering of both the front and rear wheels are executed with one symmetric cylinder on each wheel axle. The cylinders are connected to a mechanism presented in figure 12. The structure of the mechanism is designed under principle of Ackermann steering. By controlling the displacement of the cylinder, the mechanism rotates the wheel inside the turn more than the wheel outside the turn. [15] If the mechanism is perfectly designed, the steering angles of the wheels under different vehicle speed and rate of heading should be equal compared to the calculations based on equations (2.9) and (2.10) presented in subsection 2.1.2.

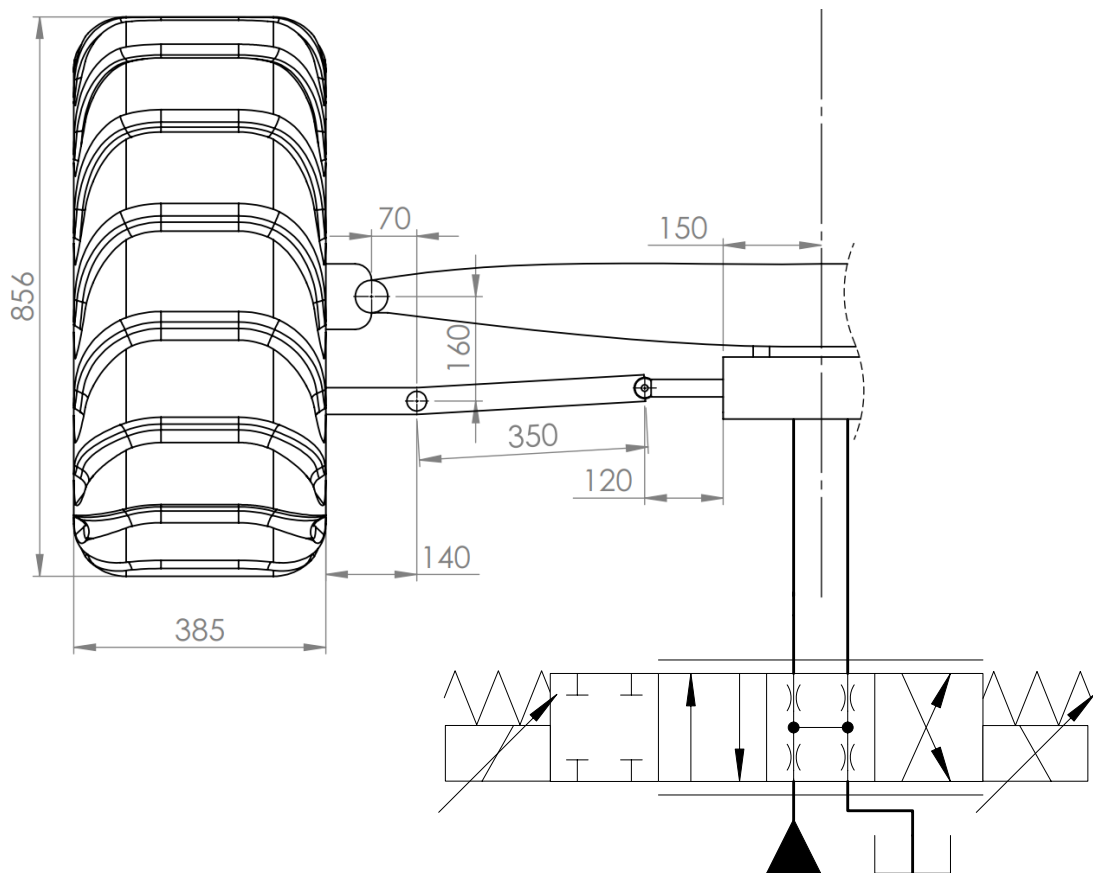


Figure 13: Dimensioned steering mechanism and simplified steering hydraulics of Haulotte 16RTJ PRO.

The dimensioned steering mechanism, steering hydraulics, and one wheel of Haulotte are presented in figure 13. The measurement unit in the figure is *mm*. Due to the lack of real manufacturer data, the measurements are executed by the author at the outdoor laboratory of Tampere University of Technology. The dashed line perpendicular to the steering cylinder implies that the steering structure is symmetrical with respect to the line. The circular marks of the structure represent 1 DOF (Degree of Freedom) joints that rotate with respect to the displacement of the cylinder. The displacement of the cylinder is controlled with a 4-way proportional valve presented in the figure. On the left, the first position of the valve is a safety position, in which the valve can be switched to in a case of any kind of failure. In the study vehicle, both front and rear wheels of the vehicle are steered by using identically dimensioned mechanical and hydraulic steering structures [15].

2.4.2 Hydraulic Articulated-Frame-Steering

Articulated-frame-steering is a system where front and rear body of the vehicle are connected together with a vertical hinge. In heavy-duty mobile machines, the steering of the machine is usually implemented with one or two hydraulic cylinders, which are connected to both rear and front body of the vehicle. [4, 8]

In the experiment vehicle Ponsse Caribou S10, articulation is executed by controlling piston strokes of two asymmetrical hydraulic cylinders presented in figure 14 [17]. When the articulation is executed with two identical cylinders, it simplifies the control of the articulation, because especially during constant tire-terrain conditions the needed actuator forces are equal to both articulation directions. Ideally, the two cylinders therefore function as a one symmetric cylinder. The vertical hinge connecting the front and rear bodies of the vehicle is presented between the cylinders in the figure.

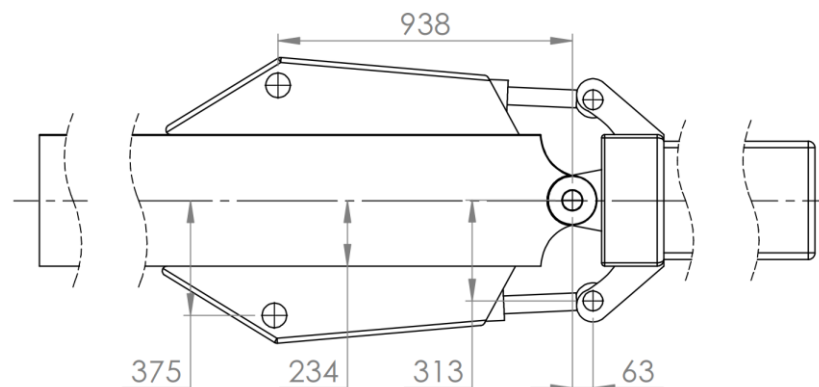


Figure 14: *The modelled articulation mechanism of Ponsse Caribou S10.*

The dimensions of the presented articulation structure are in *mm*. Due to the lack of real manufacturer data, the measurements were conducted by the author at the outdoor laboratory of Tampere University of Technology. The measured main base dimensions of the vehicle are presented in appendix A.

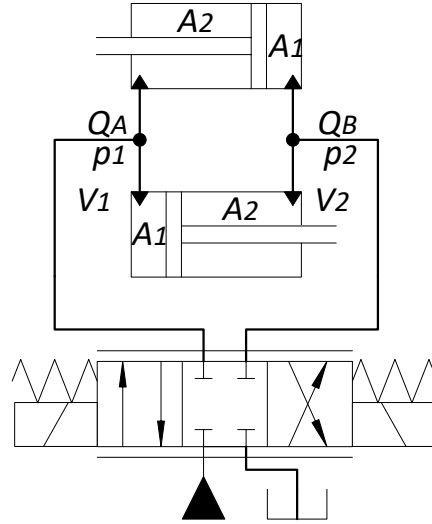


Figure 15: Articulation hydraulics of Ponsse Caribou S10.

The main structure of the articulation hydraulics is presented in figure 15. The cylinders are cross-connected to each other [17]. This provides the possibility for symmetrical steering control, as presented in the previous paragraphs. Proportional valve with four ports and three positions is being used for controlling the movements of the cylinders. The power source of the system consist of variable displacement pump with a load sensing property [17]. For simplification purposes, in this study the pressure source of the system is modelled as a constant pressure source.

The hydraulic cylinders are connected to a common moving mechanism. This kind of a mechanical linkage between the cylinders and articulation joint constraints the linear velocities of both of the cylinders to be equal, but towards opposite moving directions. With this kind of constraint and when the cylinders are cross-connected, by using the continuity equation (2.32) the pressure derivatives of the two volumes can be formed as

$$\frac{dp_1}{dt} = \frac{B_{eff}}{V_1} (Q_1 - A_1\dot{y}_1 - A_2\dot{y}_2) \quad (2.36)$$

$$\frac{dp_2}{dt} = \frac{B_{eff}}{V_2} (Q_2 + A_1\dot{y}_1 + A_2\dot{y}_2). \quad (2.37)$$

In the equations, Q_1 and Q_2 respectively represent the flows Q_A and Q_B presented in figure 15. Cylinder velocities are presented as derivatives of their positions y_1 and y_2 . The volumes presented in the equations construct of the hoses' volumes and the chambers volumes, and those can be presented as

$$V_1 = V_h + A_1y_1 + A_2(L - y_2) \quad (2.38)$$

$$V_2 = V_h + A_1y_2 + A_2(L - y_1) \quad (2.39)$$

where V_h is the constant volume of the hose and L is the length of the piston stroke.

2.5 Modelling of Physical Systems in Matlab Simscape Environment

2.5.1 Construction Blocks and Physical Connections

Physical models of the vehicles are implemented under Matlab Simscape environment. Specific parts, such as wheels and bodies of the vehicles, are generated using Three-dimensional Computer Aided Design (3D-CAD) program SolidWorks². Visualizations of the modelled vehicles are presented in figure 16.



Figure 16: Visualizations of the modelled vehicles.

The vehicles are modelled with top-to-ground principle. Mechanical structures of the models are mainly constructed of three different building blocks: solid structures, rigid transformations, and joints. Visualizations of these blocks are presented in figure 17.

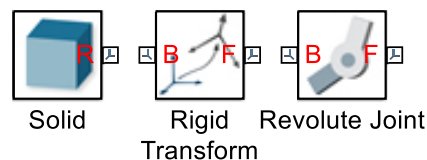


Figure 17: The main building blocks of Simscape environment.

² The official homepage of SolidWorks: <https://www.solidworks.com/>

All visible parts of the model are solid structures. Solid structures pose certain geometry, which is either defined in the block parametrization, or imported from an external file, such as the wheels of the models presented in figure 16. The inertia of the solid is calculated either from geometry of the part, or it can be considered as a point mass.

Rigid transforms are used to connect solid structures. Rigid transforms have two main properties: translation and rotation. Frame B is the base frame of the translation and frame F can be rigidly translated and rotated with respect to frame B. Rigid transformations are simple and effective way to model the geometric properties of the vehicles.

Joints provide all possible movements between rigid structures of the model. The most commonly used joint is called revolute joint, which provides a revolution motion around the z-axis of the joint's coordinate frame. Revolution joints are used in wheel rotation, frame-articulation, and wheel-steering of the modelled vehicles.

Joints can receive either torque, force, or motion as an input. Depending of the input, the joint either calculates the motion caused by the input torque or force, or torque or force caused by the motion command. In this study, all internal dynamics for driving, steering and articulation are modelled. Therefore, all joints which are controlled and effect on determining the pose of the physical robot receive either force or torque as an input. These inputs are determined by the hydraulic steering and driving power transmission systems.

2.5.2 Tire-Terrain Interaction

Accurate modelling of tire-terrain interaction is a challenging real-life phenomenon to model. When the vehicle is moving straight forward without wheel slippage, modelling of the interaction can be simplified into a two-dimensional case, where a certain traction force is required for a wheel to move forward with constant velocity.

With many steering structures, such as articulated-frame- and skid-steering, slippage of wheels is inevitable. In the research [3], slippage angles for the wheels in articulated steering were presented. According to the results, with high velocities and fast steering, the slippage angles affected significantly to the actual heading of the vehicle [3].

In this study, the tire-terrain interaction is modelled by using Simscape Multibody Contact Forces Library [16]. The library is generated for free use by Steve Miller, who is responsible for the technical marketing of the Simscape products at MathWorks. Miller has been working as an Application Engineer developing Matlab, and especially Simscape products at MathWorks since 2005. [16]

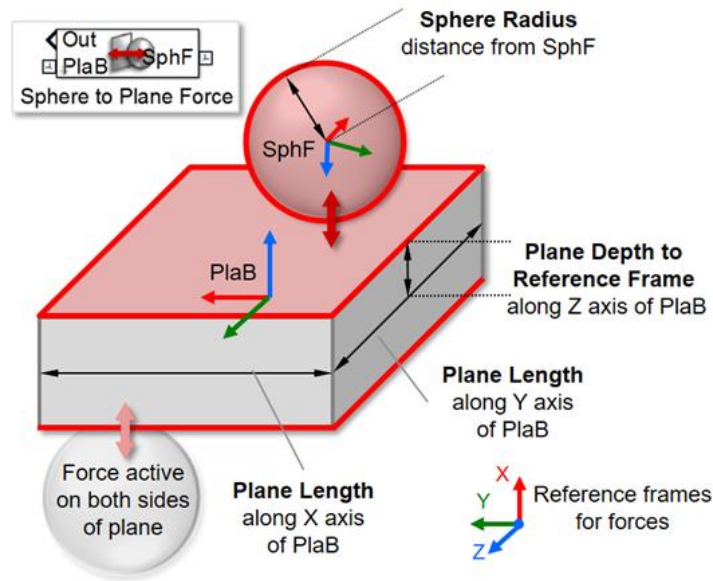


Figure 18: Sphere to Plane Contact Force block provided by MathWorks. [16]

The high-level properties of the contact force block used for modelling the tire-terrain interaction is presented in figure 18. Volume of the sphere is defined according to the diameter of the tire of the robot. The contact between tire and terrain is modelled as a specific point of contact (POC) in the middle of the tire's contact patch. The block constructs of two separate sections: models for contact force law and friction force law. [16]

Contact Force Law

Contact force law implemented in the Sphere to Plane block is illustrated in figure 19. Frames $\{B\}$ and $\{F\}$ represent base and follower frames presented in figure 18. In the block, a linear spring-damper force is modelled to resist the penetration. In this study, penetration can be seen as deformation of the tire during acceleration or cornering.

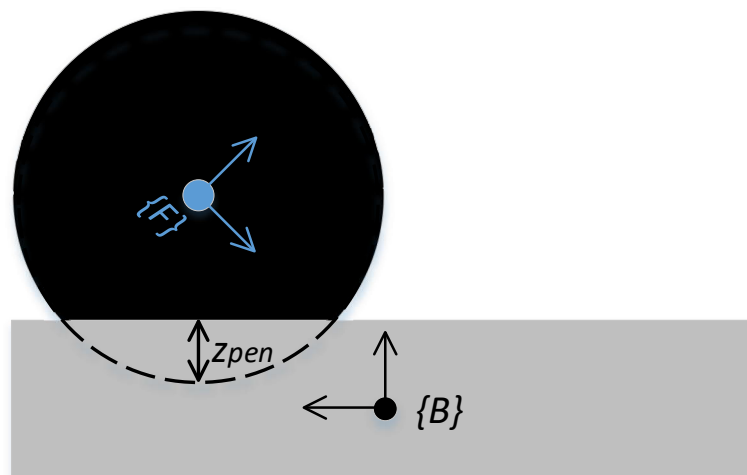


Figure 19: Illustrating figure of the contact force law implemented in the Sphere to Plane block. Figure is adapted from [16].

According to [16], the modelled contact force between tire and terrain is based on the equation

$$F_z = \begin{cases} kz_{pen} + bv_{pen}, & z_{pen} > 0, v_{pen} > 0 \\ kz_{pen}, & z_{pen} > 0, v_{pen} < 0 \\ 0, & z_{pen} \leq 0 \end{cases} \quad (2.38)$$

where v_{pen} is the velocity of the deformation z_{pen} , respectively. In the case of increasing velocity and deformation, the generated force is based on both spring and damping term. Coefficient k represents the stiffness between tire and terrain and b is the coefficient for damping factor. When the deformation velocity decreases, only the spring term effects on the generated force. When the deformation is zero or less, there is no contact between the tire and terrain. In practice, the tire is in the air due to, for example, a bump on a road. During a contact, the magnitude of deformation is always more than zero.

Friction Force Law

Coordinate systems used in friction force law implemented in the Sphere to Plane block are presented in figure 20. Friction force law of the block [16] can be presented as a function of normal force F_n multiplied with the coefficient of friction μ .

$$F_f = \mu F_n \quad (2.39)$$

$$\mu = \begin{cases} \frac{v_{poc}\mu_s}{v_{th}}, & v_{poc} < v_{th} \\ \mu_s - v_{poc} \frac{\mu_s - \mu_k}{0.5v_{th}}, & v_{th} \leq v_{poc} \leq 1.5 v_{th} \\ \mu_k, & v_{poc} > v_{th} \end{cases} \quad (2.40)$$

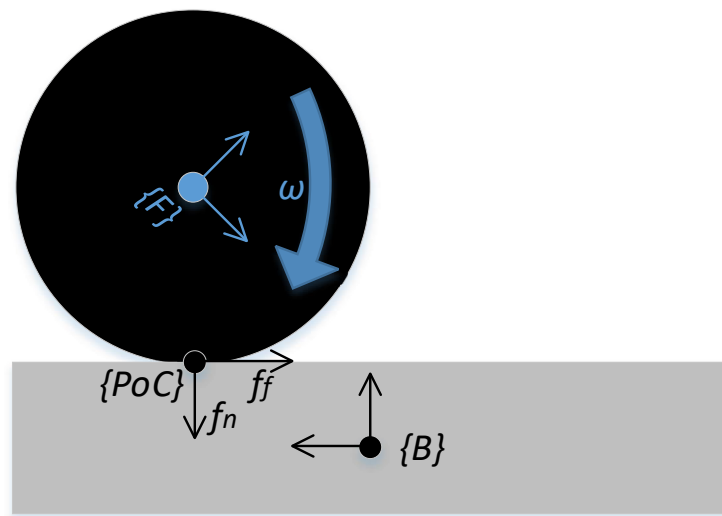


Figure 20: Illustrating figure of the friction force law implemented in the Sphere to Plane block. Figure is adapted from [16].

The friction coefficient of equation (2.40) is a function of the relative velocity at the POC. When the contact point velocity v_{poc} is smaller than threshold velocity v_{th} , the coefficient is a static friction coefficient μ_s multiplied with ratio of the velocities. For POC velocities in $v_{th} \leq v_{poc} \leq 1.5 v_{th}$, the coefficient is a function of both velocities and friction coefficients, static and kinematic μ_k . When the POC velocity is higher than the threshold velocity, coefficient of the friction force is the kinematic friction coefficient. [16]

2.6 Path-Following Control of Wheeled Mobile Robots

2.6.1 Review on Different Path-Following Control Methods

In this subsection, a short review of different path-following methods is conducted. Most of the gathered results are based on the review of the state of the art in path-following control conducted in November 2016 by the authors in [18].

Follow the Carrot

One of the first developed path-following controllers is called *Follow the Carrot*. In this approach, instantaneous goal point with a specific distance is selected from the path. After the point is selected, orientation of the selected point and vehicle with respect to the world frame is measured, and the error signal of the heading is being formed based on these measurements. With a simple proportional controller, the error is pursued to be driven to zero. The principle of Follow the Carrot is presented in figure 21. [18]

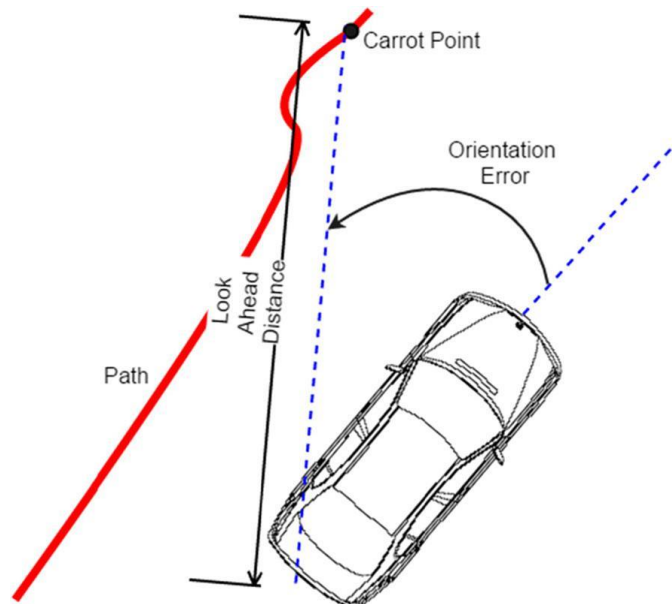


Figure 21: Follow the Carrot control method. [18]

Pure Pursuit

The most common controllers used in path-following are based on the *Pure Pursuit* method. Pure Pursuit is quite simple, yet very effective method, where a vehicle is considered pursuing a specific reference point moving on a specific path. In addition to calculating heading error as previously described in the Follow the Carrot method, Pure Pursuit strives to achieve smooth steering by forming a circular path between the control point of the vehicle and reference point on the path. Pure Pursuit control was first time implemented in the end of the 1960s. The strategy was first used for missile tracking, where the heading of the missile was controlled for the missile to fly towards a certain goal point. [18]

According to the authors in [18], the very first implementation of Pure Pursuit in mobile robots was conducted by R. Wallace et al. in [19]. In their publication, the authors developed control strategies based on the principle of Pure Pursuit and visual feedback for two mobile robots. The systems were tested both indoor and outdoor. The best test result according to the authors was a travelled path of 20 meters at speed of 2 cm/sec. [19]

In the 1990s, author from Carnegie Mellon University in [20] compared the Pure Pursuit method against methods such as quantic polynomial fitting and “Control theory”, and proved that Pure Pursuit was the most robust and reliable path-following control method of that era. A technical report [21] from the same university reported the main property of the Pure Pursuit, called look-ahead distance, which effects the most to the reliability and stability of the control. According to the authors, too short look-ahead distance will cause oscillation and for the robot to overshoot from the path at certain tight or fast cornering situations. On the other hand, too long distance will cause the robot to cut corners while trying to follow the reference frame and maintain the desired distance. [21]

In the present century, Pure Pursuit has established its position as the main benchmark for researchers when proposing new path-following controllers. Many different controllers with various adjustments [22, 23, 24] are all build on the base of Pure Pursuit. Due to its simplicity, wide popularity, and proven effectiveness, the path following controller implemented in this study is also partly based on the method of Pure Pursuit. The implemented controller is presented in the next subsection 2.6.2.

Stanley Method

Stanley method is a control structure detailed by Hoffmann et al. [25]. The method was developed for DARPA Grand Challenge in 2005³, which was a race designed for autonomous mobile robots. Winner of the race in 2005 was a team from Stanford University, and their winning autonomous vehicle was named as Stanley. [18]

³ See: <https://www.darpa.mil/about-us/timeline/-grand-challenge-for-autonomous-vehicles>

The structure of the controller is based on measuring and controlling of two different errors. The heading error of the vehicle is determined with respect to the trajectory heading, similarly as in pure pursuit. The lateral error is defined by measuring the distance between the closest point of the trajectory and the steering axle of the vehicle. Based on [25], the equation of the control strategy for the steering command can be derived as

$$\delta(t) = (\theta - \theta_{traj}) + \arctan\left(\frac{ke(t)}{v(t)}\right), -\delta_{max} < \delta(t) < \delta_{max} \quad (2.41)$$

where θ is the measured heading of the vehicle, θ_{traj} is the heading of the trajectory, $e(t)$ is the measured lateral error, and $v(t)$ is the velocity of the control point of the vehicle. The steering control is saturated according to steering limitations as presented. The structure of the controller in [25] also contained additional terms for example stabilizing controller during low velocities and compensating the dynamic properties of the vehicle. However, these terms were never implemented and used in the race [18].

Model-Based Control

Model-based controllers (MBC) are designed to take the overall vehicle model into consideration while determining the output control signals. The interests towards model-based controllers are increasing due to the increasing availability of super computers, which provide enough computational power for the complex algorithms, in which these controllers rely on. [18]

Model predictive controller (MPC) is one of the implemented MBC methods used in path-following. In the MPC, the model usually has a specific optimization process, which the model uses for determining the optimal value for the control output. Many studies have been done that implement MPC controllers. [26, 27]

2.6.2 Nonlinear Path-Following Control Law

Path-following controller implemented in the study is mainly based on a book [7] written by K.M. Lynch and F.C. Park in 2017. The variables used throughout deriving the controller are presented on the following page in figure 22. In the figure, $\{s\}$ represents the world frame, frame $\{d\}$ represents the configuration frame driving along the defined path, and $\{b\}$ is a frame attached to the control point of the robot. [7]

The reference frame $\{d\}$ moving along the path can be referred to as the Frenet-Serret frame. The frame is designed to describe the kinematic properties of a point moving along a continuous, differentiable curve. In a two-dimensional case such as the path-following of wheeled mobile robots, variables \mathbf{t} and \mathbf{n} are used to describe the tangential and normal unit vectors, respectively, present at that exact point of that exact path curvature. For the sake of clarification, the tangential vector points towards the direction of the heading and the normal vector is perpendicular with respect to the curve at that exact point. [7]

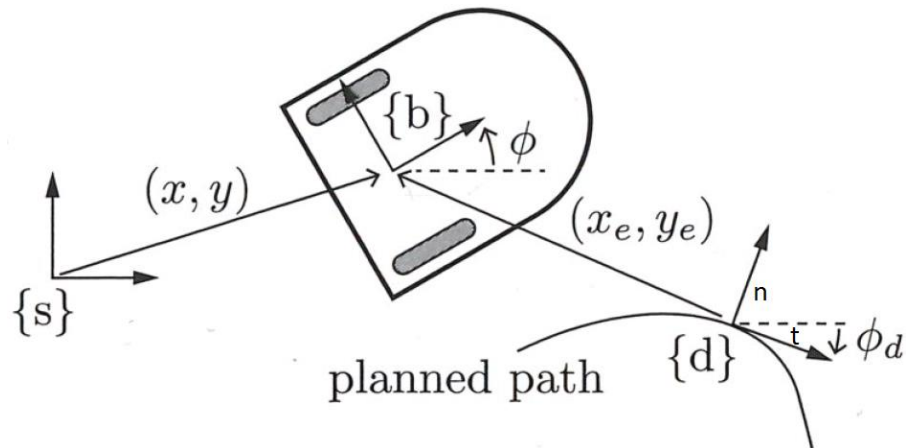


Figure 22: Illustrating figure of the coordinate frames and variables used in the control law. The figure is adapted from [7].

Whereas the original pure pursuit method measures the tracking error as a straight distance from the vehicle control point to the closest point on a path, the tracking error coordinates of the control law in [7] are expressed in the configuration frame $\{d\}$ as

$$\begin{bmatrix} \phi_e \\ x_e \\ y_e \end{bmatrix} = \begin{bmatrix} 1 & 0 & 0 \\ 0 & \cos\phi_d & \sin\phi_d \\ 0 & -\sin\phi_d & \cos\phi_d \end{bmatrix} \begin{bmatrix} \phi - \phi_d \\ x - x_d \\ y - y_d \end{bmatrix} \quad (2.42)$$

where the position errors x_e and y_e are presented along vectors \mathbf{n} and \mathbf{t} shown in the figure. Similar to the Pure Pursuit method, the error for the heading is the difference between the current measured heading and the desired heading. [7]

For given errors, the nonlinear control laws for velocity and angular velocity of the vehicle can be presented as

$$\begin{bmatrix} v \\ \omega \end{bmatrix} = \begin{bmatrix} (v_d - k_1|v_d|(x_e + y_e \tan\phi_e))/\cos\phi_e \\ \omega_d - (k_2 v_d y_e + k_3 |v_d| \tan\phi_e) \cos^2\phi_e \end{bmatrix} \quad (2.43)$$

where v and ω are the command signals for linear and angular velocity of the control point of the robot, respectively. First thing to be noted about the controller is that in addition to feedback, the controller is also using feedforward. In practice, for zero error, the control signals are the desired control values v_d and ω_d . Different terms of the control laws have different functionalities. Before explaining these functionalities, for clarification, the terms can be presented as follows:

- **Term 1:** $k_1|v_d|x_e/\cos\phi_e$
- **Term 2:** $k_1|v_d|y_e \tan\phi_e/\cos\phi_e$
- **Term 3:** $k_2 v_d y_e \tan\phi_e \cos^2\phi_e$
- **Term 4:** $k_3 |v_d| \tan\phi_e \cos^2\phi_e$

The first term is used purely on the reduction of tangential error by increasing or decreasing the velocity of the robot [7]. In path-following, this can be considered the least important factor, since the main goal of path-following can be considered to be to stay on the given path as accurately as possible, ergo the prior goal is to minimize the normal y error distance. The second and third term of the control law try to reduce this measured normal error. The second term reduces the error by using the component of the forward or backward velocity that impacts normal error. The third term can be said to act as predictive control term, which tries to reduce the normal error in the future by controlling the heading direction of the robot. The fourth term of the control laws attempts to reduce the heading error. [7]

2.7 Path Generation

2.7.1 Cubic Bézier Curves

In path generation, the main goal is to generate a smooth path from the desired start pose to the desired end pose. The smoothness of the path is a crucial factor for path-following controllers, especially for controllers based on Pure Pursuit, which were presented in section 2.6.

Bézier curve is a parametric curve developed by a French engineer Pierre Bézier. Bézier curves are used to model smooth curves, especially in computer graphics. One of the major advantages in using Bézier curves for path generation is the parametrization property of the curve, which is presented in the following paragraphs. [28]

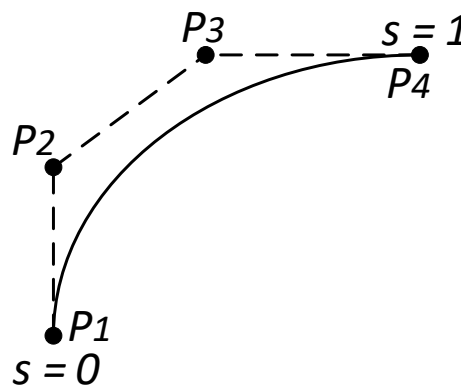


Figure 23: Fourth order cubic Bézier curve and its control points.

Bézier curve can be defined with set of points from P_0 to P_n , where n represents the order of the curve. Fourth order cubic Bézier curves are being used in this thesis. Principle figure of a cubic Bézier curve is presented in figure 23. Cubic Bézier curve can be presented as a function of the curve parameter s

$$B(s) = (1 - s)^3 P_1 + 3(1 - s)^2 s P_2 + 3(1 - s) s^2 P_3 + s^3 P_4 \quad (2.44)$$

where P_1 and P_4 represent the initial start and end points of the curve, and P_2 and P_3 define the headings of the curve at these points, respectively. [28] In path generation, the points construct of x and y coordinate pairs $[x, y]^T$ represented with respect to the world frame.

During path-following, the desired angle of heading can be obtained from the derivative of the cubic curve. According to [28], the derivative of fourth order Bézier curve with respect to curve parameter s can be defined from equation

$$B'(s) = 3(1 - s)^2(P_2 - P_1) + 6(1 - s)s(P_3 - P_2) + 3s^2(P_4 - P_3). \quad (2.45)$$

The curve parameter s is defined as $0 \leq s \leq 1$. As presented in figure 23, at the start point of the curve s equals 0 and at the end s is 1. By controlling the rate of the progress of s , the reference speed of the path generation can be controlled. The implementation of the matter is presented more deeply in the path generation modelling section 3.3.

3. MODELLING OF THE STUDIED SYSTEMS

3.1 Modular System Architecture

Modular architecture of the implemented simulation model is presented in figure 24. The model constructs of four main segments: Control Points from Database, Path Generator, High-level Controllers and two studied Vehicle Models. The following sections of the chapter are divided based on the last three of these segments. Modelled robots and their internal dynamics and physical structures are dealt separately in sections 3.2 and 3.3. Implementation of the path generator is presented in section 3.4.

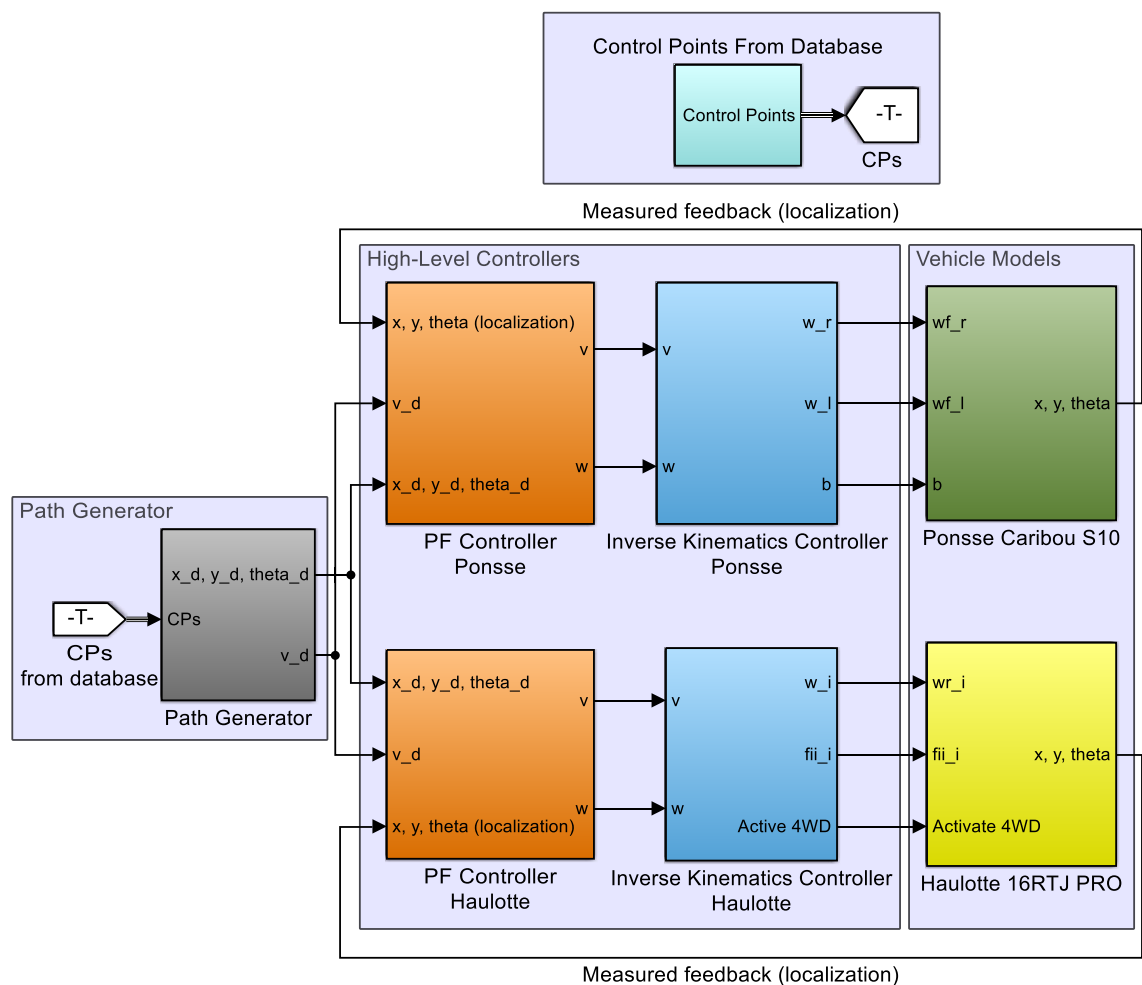


Figure 24: Modular structure of the designed system model.

High-level controllers construct of path-following controllers and inverse kinematics of different steering architectures. Path-following controllers are designed to be independent of steering architecture of the vehicle. Therefore, inverse kinematics of different steering structures are considered as high-level controllers, which are used for adjusting the steer-

ing and velocity commands of the vehicle actuators based on inputs from the path-follower. Because of the wide scopes of the subjects, modelling of path-following controller and inverse kinematics are considered separately in sections 3.5 and 3.6.

3.2 Ponsse Caribou S10

High-level schematics of the implemented simulation model of Ponsse Caribou S10 – its driveline, steering hydraulics, and main physical components and their connections – are illustrated in figure 25. Rear and front units describe the physical rear and front bodies of the vehicle, which are connected together by means of the articulation mechanism and joint. Hydraulics and mechanical structure of the articulation are implemented as presented in chapter 2. All hydraulic systems and the physical structure of the robot model are covered more deeply in the following subsections.

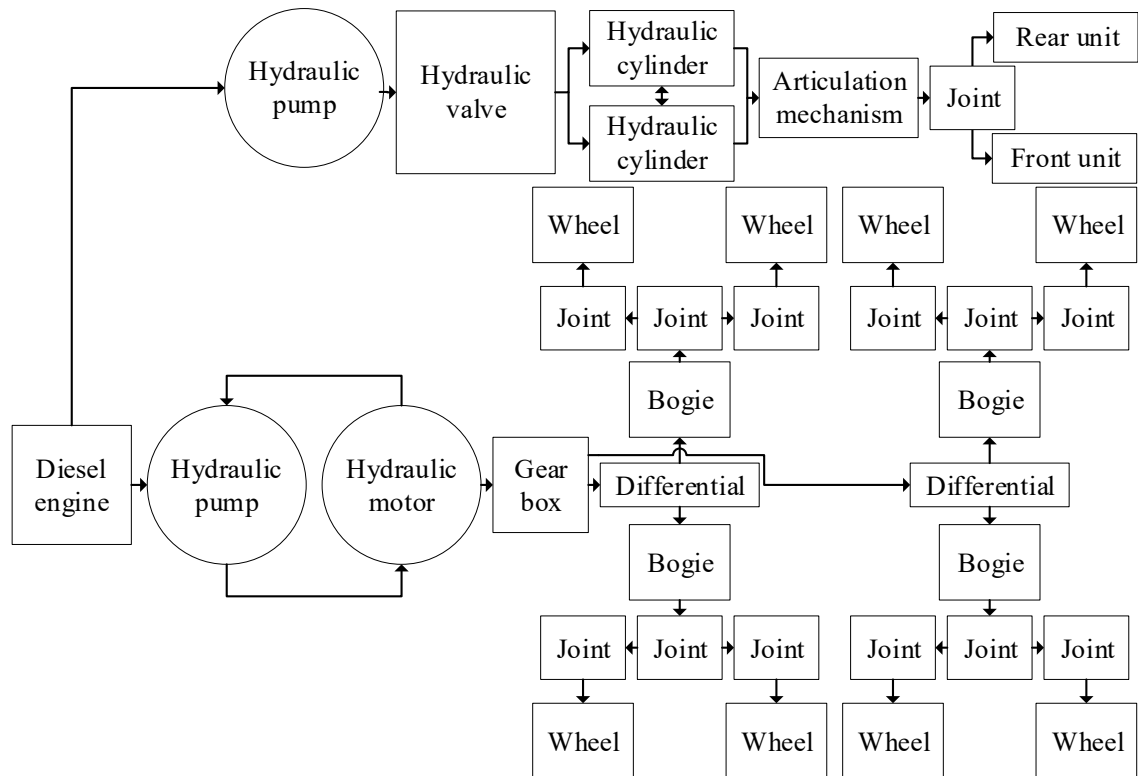


Figure 25: High-level schematics of the Ponsse Caribou S10 simulation model.

The main driveline components and their properties are presented in table 1 on following page. Knowledge of the main components used in hydrostatic transmission is crucial for implementing a valid simulation model. The other main dimensions and functional properties of the vehicle, such as maximum traction force, mass of the vehicle, and maximum allowed external load, are presented in table 2. Most of the properties are obtained from the vehicle’s owner’s manual and catalogues owned by Tampere University of Technology [17]. Specifications of the diesel engine are based on the source [29].

Table 1: Main driveline components of Ponsse Caribou S10 and their properties [17, 29].

Component	Manufacturer	Type	Order code	Technical properties	
Diesel engine	Perkins	4-cylinder diesel engine	1004-40TW Fastram	P [kW] @ 2200 rpm	91
				T [Nm] @ 1450 rpm	430
				n [rpm]	2200
Hydraulic pump	Rexroth Bosch Group	Axial piston variable pump	A4VG-90- EP-D	V_{gmax} [cm ³]	90
				V_{gbp} [cm ³]	19,6
				n_{nom} [rpm]	3050
				Q_{nom} [$\frac{l}{min}$]	275
Hydraulic motor	Rexroth Bosch Group	Axial piston variable motor	A6VM-160	V_{gmax} [cm ³]	160
				n_{nom} [rpm]	3100
				Q_{nom} [$\frac{l}{min}$]	496
				T_{nom} [Nm]	1019

Table 2: Main dimensional and functional properties of Ponsse Caribou S10. [17]

Main dimensions and properties	
Maximum traction force [kN]	130
Maximum system pressure [bar]	340
Weight [kg] + Maximum Load [kg]	11950 + 10000
Maximum speed [km/h]	27
Maximum articulation angle [deg]	45

The structure of the implemented dynamic model containing hydrostatic power transmission, articulation hydraulics, low-level controllers, and main sections of the physical model of the robot is presented in figure 26. In high system level, HST and articulation hydraulics receive angular velocity and articulation control commands ω_{fr} , ω_{fl} and bd from the upper level control. Based on these control signals and measured feedback wheel velocities ($\omega_{frmeas}, \omega_{flmeas}$) and articulation (b_{meas}), the low-level controllers of HST and articulation hydraulics adjust the control signals for displacement of the hydraulic pump and motor, and control signal for controlling the position of the proportional control valve, which adjusts the positions of the articulation cylinders.

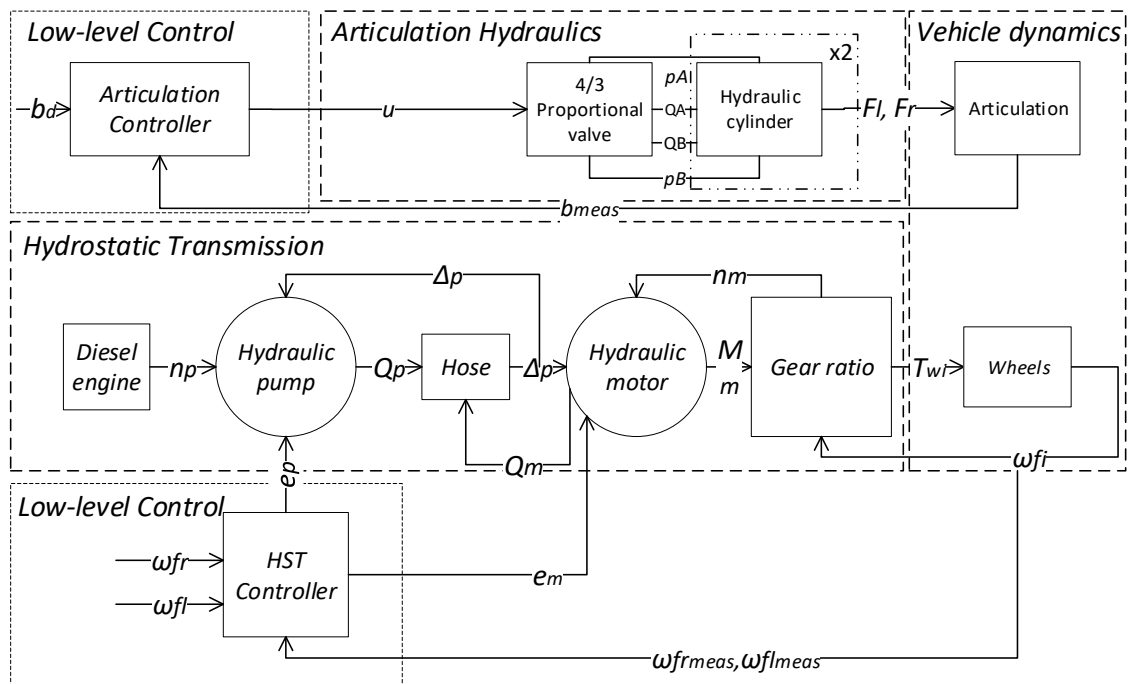


Figure 26: Schematics of the implemented robot model and low-level controllers of Ponsse Caribou S10.

For the sake of clarity, the physical vehicle model presented in the figure is simplified to construct of articulation and wheel dynamics, which are the only subsystems of the physical model that receive external inputs. Due to modelling of hydraulics of the machine, the vehicle model receives only either torque or force as an input. Implementation methods of the physical robot model are presented in subsection 3.2.3.

3.2.1 Hydrostatic Power Transmission

Hydrostatic transmission of Ponsse Caribou S10 constructs of four main components: diesel engine, hydraulic hoses, and hydraulic variable displacement units of pump and motor. The implementation of the modelled HST is presented in figure 27 on the next page. Inputs 1 and 2 represent the displacement commands of the hydraulic motor and pump, which are coming from the low-level HST control. Outputs 1 and 2 are the torque

produced by the hydraulic motor and the pressured difference over both of the hydraulic units, respectively.

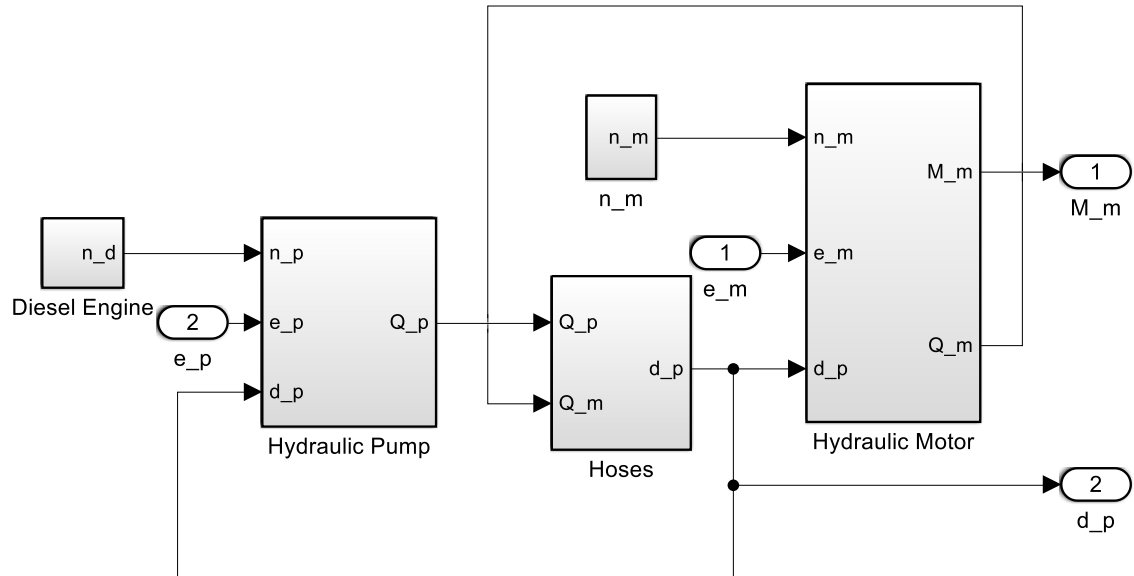


Figure 27: Modelled HST of Ponsse Caribou S10

When the HST is being controlled either with traditional or secondary control, as presented in subsection 2.2.2, the rotation speed of the diesel engine is strived to be held constant. Therefore, the diesel engine is simply modelled as constant, which provides a rotation speed of 2200 rpm for the hydraulic pump. The model of the hydraulic pump is based on equations (2.11) and (2.12). For a given rotation speed and displacement, the pump produces a certain flow. The volumetric efficiency of the pump is modelled as a function of the pressure, as presented in equation (2.15).

Pressure lines between hydraulic pump and motor are implemented using equations (2.17) and (2.18). As inputs, the model receives the output flow of the pump and input flow of the motor. Based on the difference between the flows, and bulk modulus and volume of the hose, the derivative of the pressure can be calculated. When the pressure of the low-pressure side is subtracted from the high pressure, the pressure difference over the hydraulic motor and pump can be calculated.

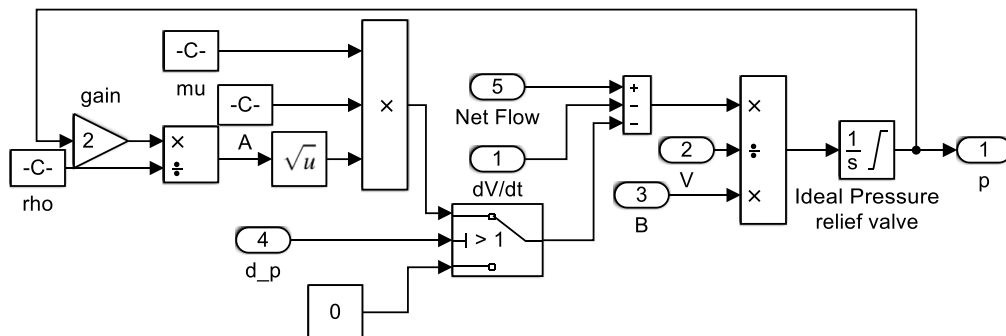


Figure 28: Pressure line model.

A pressure line model used throughout this thesis is presented in figure 28. In addition to previously presented, there are two additional inputs which are subtracted from the net flow presented in the previous paragraph. Input $\frac{dV}{dt}$ presents the change of the hose volume with respect to time. In this study, the change of the volume is neglected, ergo the volume of the pressure line is assumed to be constant. The purpose of the second additional input is to represent the effect of the flushing valve. This function activates only if the line functions as the low-pressure line of the closed HST circuit. The switch in the figure is used to define whether the current line is the high-pressure line or the low-pressure line of the closed circuit. When the flushing valve is active, the valve directs a specific amount of the flow to the tank, which can be seen as decreasing net flow size. The size of the flow is determined so that the low-pressure side will maintain a constant pressure, which is set in the system initialization. In this study, the constant pressure on low-pressure side is set to 20 bar.

Model of the hydraulic motor is based on equations (2.13) and (2.14). The volumetric efficiency is considered to be similar to the pump, as presented in previous sections. The motor output torque is based on the pressure difference and volume of the motor. The torque losses caused by the viscous and Coulomb friction are modelled according to equation (2.16).

3.2.2 Articulation Hydraulics

The modelled hydraulic system for the articulation of the vehicle constructs of two identical hydraulic cylinders and proportional hydraulic valve. As presented in subsection 2.4.2, the cylinders are cross-connected. In theory, this implies that the force required to articulate the vehicle is equal towards both articulation directions.

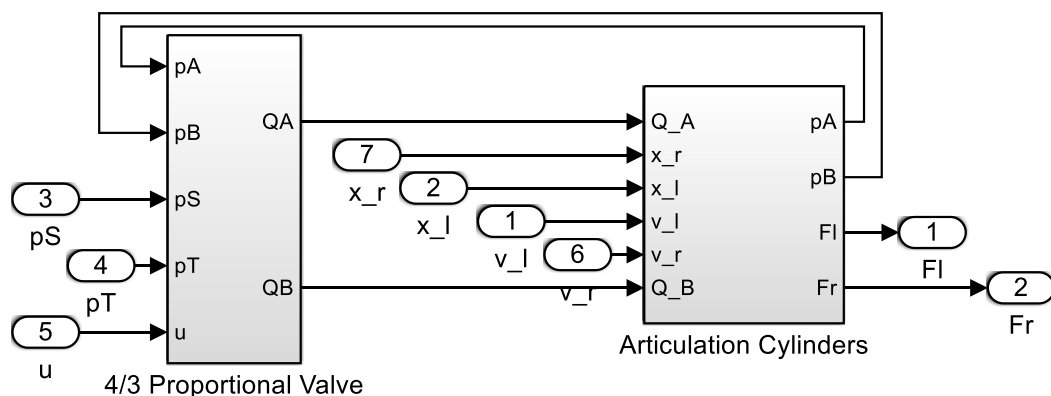


Figure 29: Implemented articulation hydraulics of Ponsse Caribou S10.

Modelled hydraulics of the articulation system containing two cylinders and 4/3-proportional valve are presented in figure 29. The friction model and valve are modelled according to equations (2.33-2.35) presented in section 2.3. The mechanical constraint presented in subsection 2.4.2 implies that the linear velocities of the cylinders are always equal, but

towards opposite directions. Based on this constraint and the cross-connection of the cylinder chambers, the two cylinders and all hoses from the valve to them can be modelled as two separate volumes by using equations (2.36-2.39).

The proportional valve's inputs p_S , p_T , and u are the pressure produced by the ideal pressure controlled hydraulic pump, the tank pressure, and the control signal for opening of the valve, respectively. The opening of the valve is controlled by using simple PID controller. Controller receives the desired articulation from the inverse kinematics and the measured articulation angle. Based on the input articulation signals, controller adjusts the valve control signal to drive the error between the control and measurement to zero. Inputs 1, 2, 6 and 7 of the figure represents the positions and velocities of the hydraulic cylinders, which are received from the physical robot model. Outputs 1 and 2 represent the forces generated in the left and right steering cylinder, respectively.

3.2.3 Physical Vehicle Model

Physical vehicle model is implemented using Matlab Simscape environment. The structure of one of the four physical links from a wheel axle to the tire-terrain interaction is presented in figure 30 on the following page. The whole vehicle model is implemented by using the same methods. Figures of the whole implemented model, including driving and steering dynamics and their controllers, are presented in appendix C.

Rigid transformations are used for moving from one coordinate frame to another, as presented in the figure. The bogie and wheels section constructs of three separate solid structures. The revolute joints of the wheels are constrained with a gear constraint block. Therefore, the bogie revolute joint is the one which receives the mechanically transmitted torque input from the HST, and the wheels revolutions are determined based on the revolution of this joint. Furthermore, the bogie joints together with the articulation joint provides the possibility for the vehicle to move on an uneven terrain. However, due to the simplicity of the tire model and flat ground profile used at the current phase of the project, this can be considered as an interesting point for the future development.

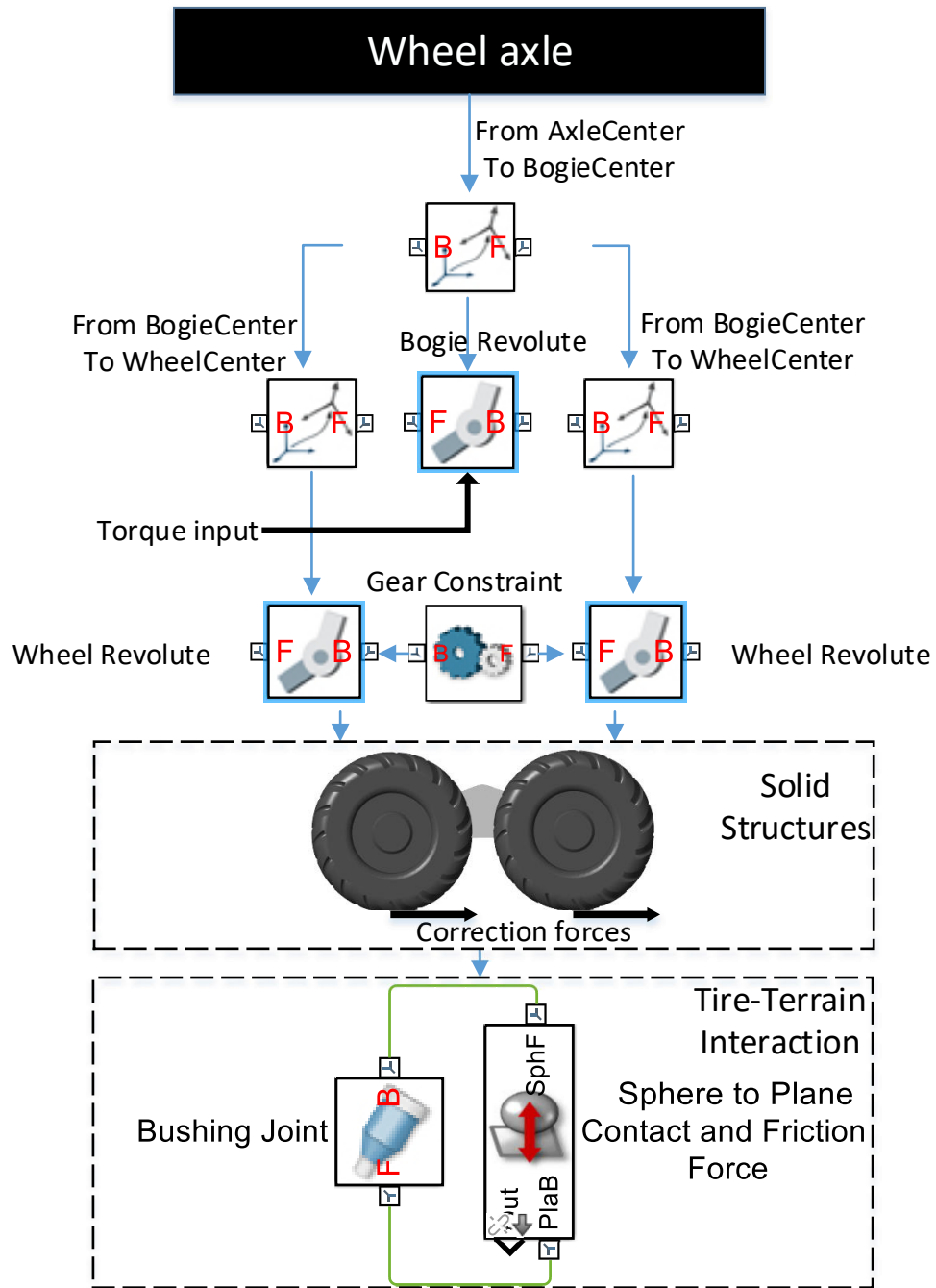


Figure 30: Implementation of the physical structure of one Axle-to-Ground link of Ponsse Caribou S10.

The tire-terrain interaction is implemented using bushing joints and sphere to plane blocks provided by Simscape Multibody Contact Forces Library [16]. By using this kind of structure, pose of the robot is determined based on the forces affecting between the tire and terrain. The physical model receives only either force or torque inputs, which are determined by the implemented hydraulic and mechanical power transmission systems. The correction forces between the tires and terrain illustrate the driving forces caused by the torque input and friction between the tire and terrain.

3.3 Haulotte 16RTJ PRO

High-level schematics of the modelled robot model of Haulotte 16RTJ PRO are presented in figure 31. Principle figure of the steering mechanism was presented in subchapter 2.4. Travel reducers are implemented as constant gear ratios (see the subsection 3.3.1). Hydraulic systems and their components, and the physical robot model are covered more deeply in the following subsections.

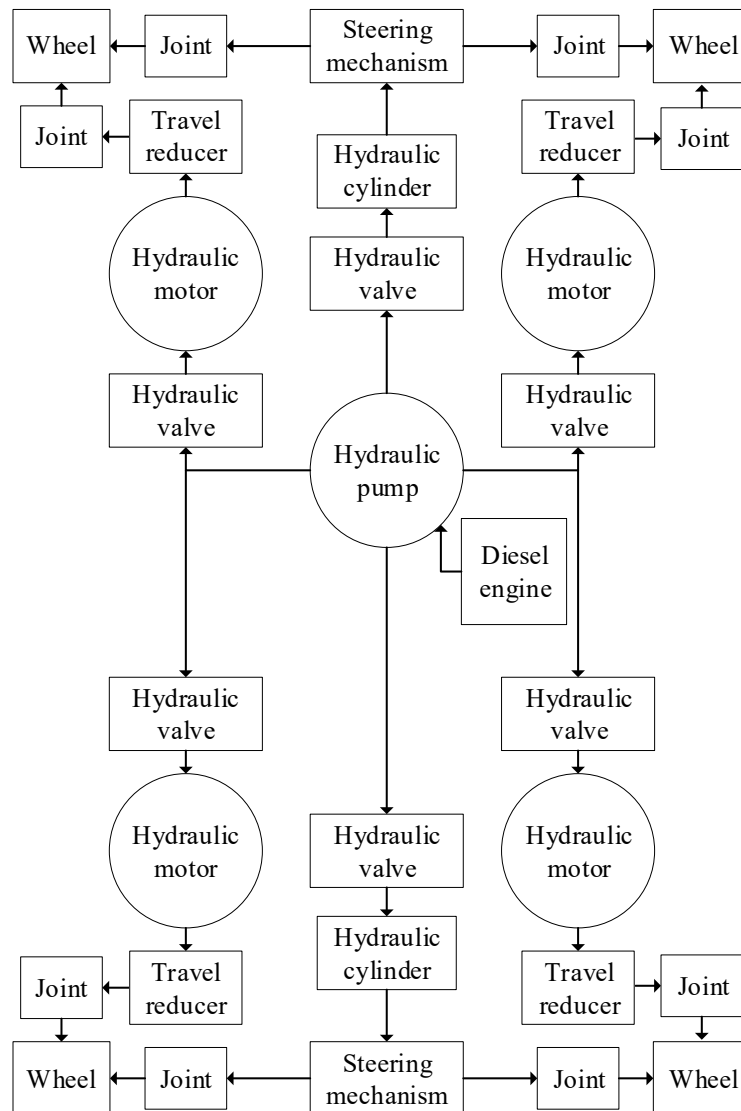


Figure 31: High-level schematics of the Haulotte 16 RTJ PRO simulation model.

Main driveline and hydrostatic steering components of the boom lift Haulotte are presented in table 3. Presented information is based on a research [15] conducted by an employee of the Laboratory of Automation and Hydraulics Engineering at Tampere University of Technology. Main actuators of the vehicle are four fixed displacement hydraulic motors and two symmetrical cylinders. The main difference compared to the traditional HST is the fact that in this vehicle the rotation speeds of the motors are controlled by

using proportional valves, where the amount of flow entering a motor is controlled by adjusting the valve opening. [15]

Table 3: Haulotte's main driveline and hydrostatic steering components and their properties [15].

	Component	Manufacturer	Type	Code	Technical properties	
Hydrostatic Transmission	Diesel engine	Kubota	4-cylinder diesel engine	V1505 E2B	P [kW]	26,5
					n [rpm]	3000
	Hydraulic pump	-	Axial piston variable pump	A4VG-90-EP-D	V_{gmax} [cm ³]	21
					n_{nom} [rpm]	3000
					Q_{nom} [$\frac{l}{min}$]	63
	Hydraulic motor	Rexroth Bosch Group	Axial piston variable motor	A6VM-160	V_{gmax} [cm ³]	100
					n_{nom} [rpm]	3100
					Q_{nom} [$\frac{l}{min}$]	496
					T_{nom} [Nm]	1019
	Hydrostatic Steering	Valve	-	YV150 4/3 electro valve	-	Q_{max} [$\frac{l}{min}$]
Δp_{max} [bar]						240
Valve		-	YV107/108 4/3 electro valve	-	Q_{max} [$\frac{l}{min}$]	12
					Δp_{max} [bar]	240

Schematics of Haulotte's dynamic robot model are presented in figure 32 on the next page. Similar to Ponsse, the desired angular wheel velocities function as inputs of the system. Based on the input velocities (ω_{wi}) and measured angular wheel velocities (ω_{wimeas}), the low-level HST controllers adjust the openings of the valves to maintain the desired flow entering the hydraulic motors. As can be seen from the figure, there are four similar HST - low-level controller combinations separately used for powering and controlling each wheel of the vehicle.

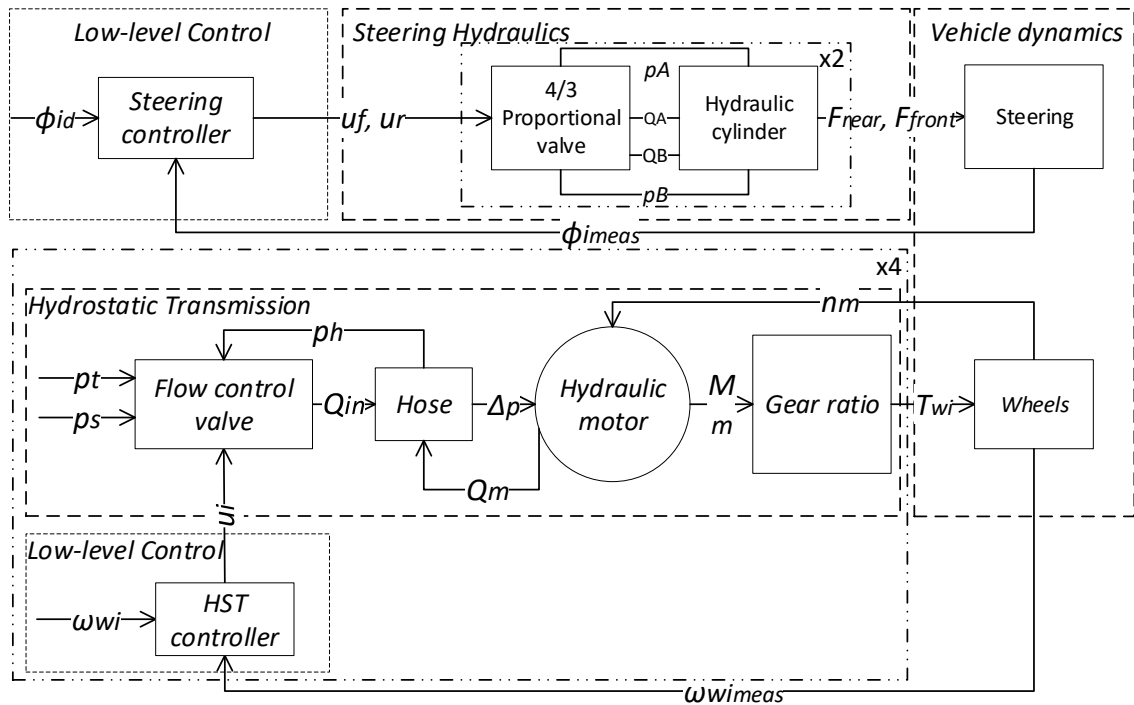


Figure 32: Schematics of the implemented robot model and low-level controllers of Haulotte 16RTJ PRO.

Hydraulics for powering the steering structure are implemented as presented on top of the figure. Proportional valves YV150 and YV107/108 presented in table 3 are used for controlling the amount of flow entering the hydraulic cylinders of front and rear wheel steering, respectively. Spool positions of the proportional steering valves are controlled with low-level PID steering controllers. The steering controllers receive the desired steering angles (ϕ_{id}) for each wheel from the inverse kinematics high-level control. These angles are compared to the measured steering signals of the wheels (ϕ_{imeas}), and openings of the steering valves are controlled accordingly to maintain the desired steering angles.

3.3.1 Hydrostatic Power Transmission

The implemented hydrostatic power transmissions of the rear section of Haulotte are presented in figure 33 on the next page. The structure of each HST constructs of three main components: proportional valve, pressure hose, and fixed displacement hydraulic motor. The fixed travel reducers of the vehicle are modelled as constant gear ratios. According to [15], the gear ratio is set to 17.7. Inputs 2, 3, 1 and 4 represent the desired and measured angular wheel velocities of rear left and rear right wheel, respectively. Outputs 1 and 2 are torque inputs for the wheels of the physical robot model.

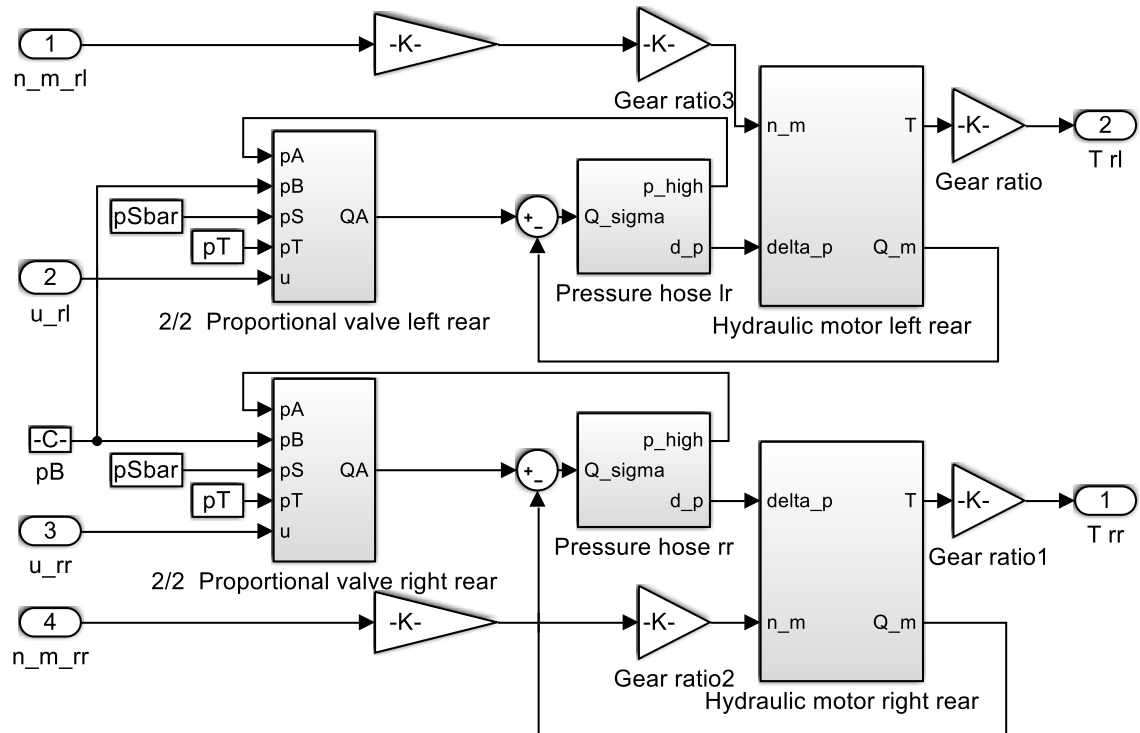


Figure 33: Implemented HST of the rear wheels of Haulotte.

According to [15], velocity of the Haulotte is controlled either varying the displacement of the hydraulic pump or by controlling the displacement of proportional control valve, which controls the amount of flow passed to the drive manifold. The drive manifold divides the flow for the hydraulic motors according to the pressure demands of each motor.

For simplification purposes, the modelling of load sensing hydraulic pump and detailed drive manifold is left out of the scope of the thesis. Therefore, the pressure source of the system is modelled as constant, ideal pressure controlled hydraulic pump, and the flow to each hydraulic motor is separately controlled by varying the opening of the valve. The possible advantages and disadvantages of more specific modelling at this stage of the development are very hard to define, especially before the behaviour of the present modelled robot is more deeply studied and analysed. Also, in one presently on-going project at the Laboratory of Automation and Hydraulics, the hydraulics of the exact study vehicle are being modified more towards this kind of structure, where the velocities of each wheel can be separately controlled.

3.3.2 Hydrostatic Wheel Steering

Implementation of hydrostatic wheel steering constructs of 4/3-proportional valve and 2-way symmetrical hydraulic cylinder. The proportional valve model is constructed based on equations (2.34) and (2.35). The hydraulic cylinder and the friction model is implemented as presented in previous subsection 3.2.2. The structures of the front and rear wheels' hydraulic steering systems are identical.

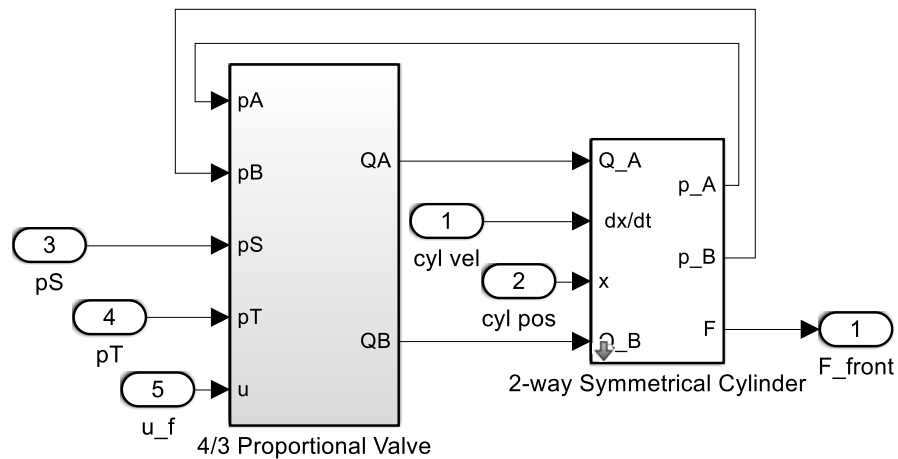


Figure 34: Implementation of the hydrostatic wheel steering hydraulics.

The implemented hydrostatic wheel steering hydraulics of the front wheel axle of Haulotte are presented in figure 34. As its inputs, the proportional valve receives constant pressures for source p_S and tank p_T , respectively. The third input u_f is the control signal for the valve opening, which is being controlled by using a PID controller, as presented in section 3.3. Inputs 1 and 2 of the figure represent inputs coming from the physical robot model. Output 1 is the generated force, which provides the movements of the steering cylinder.

3.3.3 Physical Vehicle Model

Construction methods for implementing the robot models for the both vehicles of the study are the same. Nevertheless, to highlight the differences between the mechanical structures of the vehicles, one Axle-to-Ground link of the Haulotte is presented in figure 35 on the following page.

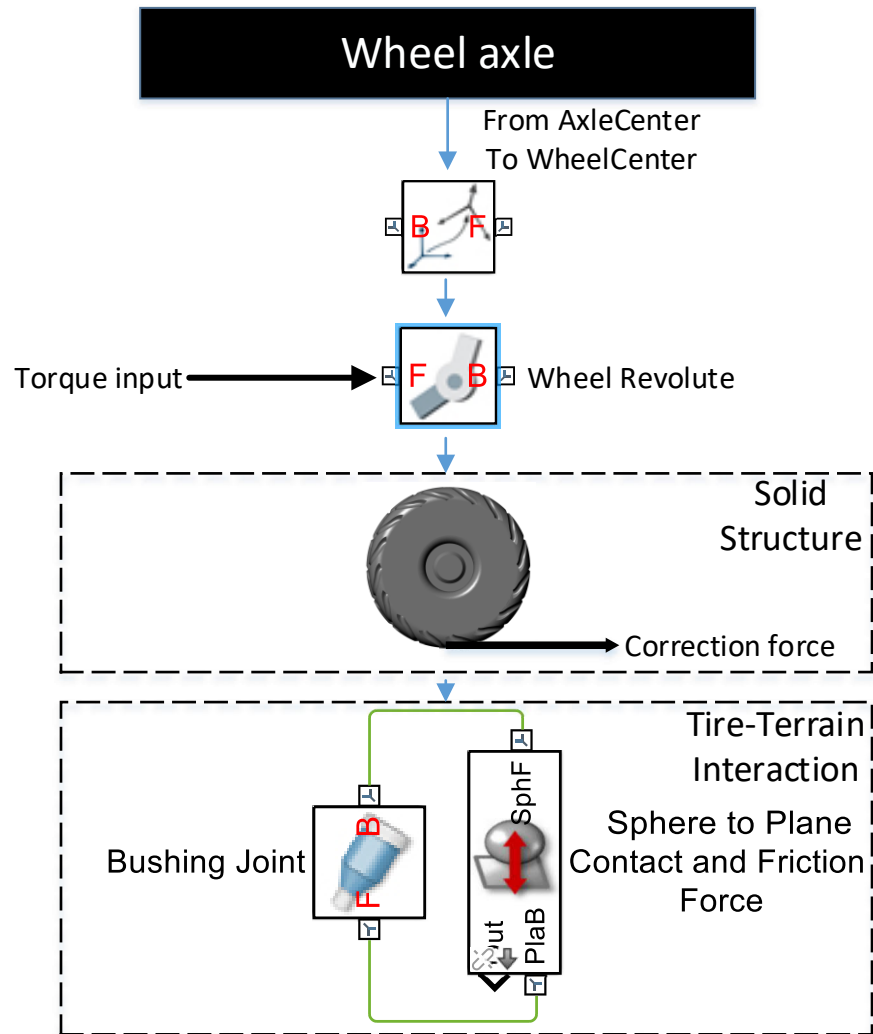


Figure 35: Implementation of the physical structure of one Axle-to-Ground link of Haulotte.

When comparing the link structures between the vehicles, the construction principles can be seen to be similar. However, the structure of the Haulotte is more trivial because of the lack of extra wheels or mechanical gear constraints. Lack of extra physical components also diminish the need for many rigid transformations, when there is no need for transformations between several components. In this illustration, the correction force is also added between the tire and terrain to describe the driving force caused by the torque input and the friction between the tire and terrain.

3.4 Implementation of the Path Generator

Path generator is implemented based on a principle of *Piecewise Continuous Path following Represented by Bézier Curves*. In continuous following, undefined amount of cubic Bézier curves is joined together to form the desired path. Properties and parametrization of a single cubic Bézier curve was presented in subsection 2.7.1.

The path generator is implemented in Matlab using Stateflow. Stateflow is an environment designed for modelling and simulating sequential decision logic systems, for example advanced control systems. The high-level design of the path generator is presented in figure 36.

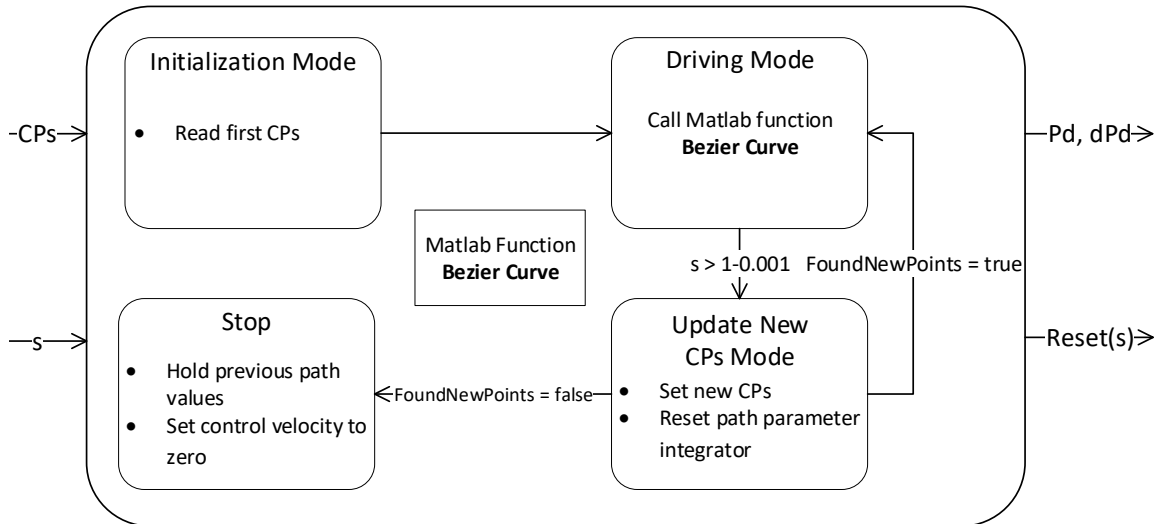


Figure 36: Block diagram of the implemented path generator.

As inputs, the path generator receives control points for the desired Bézier curves and the path parameter s . Outputs of the path generator in time domain are the desired path $Pd(t)$ and its first derivative $dPd(t)$, and in s domain the integrator reset $Reset(s)$. The outputs of the state machine are specific for each time step of the simulation. Hence, the desired path constructs of x and y coordinate pairs defined independently for each simulation step. The reference heading at each time step is received from the first derivative of the curve.

Implemented path generator constructs of four states and one Matlab function named **Bézier Curve**. The function is implemented using equations (2.44) and (2.45). Initialization is the first state of the machine. When the simulation is started, system enters the state and initializes certain values needed for path generation and reads the first four control points for the first part of the path. Starting from the initialization, the high-level functional action sequence of the path generation is following:

- 1) Read first four control points entered by the user.
- 2) Start path generation by calling Matlab function Bézier curve at each time step.
- 3) When current piece is nearly fully generated, set new four control points for the next path piece.
- 4) Reset the path parameter s and continue path generation.
- 5) Repeat sections 3 and 4.
- 6) Enter the stop state when no new control points are available.

After initialization, the path generator starts to generate path according to the first four control points entered by the user. The velocity at which the path is generated is depending on the path parameter s . When the time is increasing, the s is rising from zero to 1 with respect to this parameterization. When the s has achieved a value over 0.999, control points for new part of the path are being set, s is reset to 0, and the generation of the new path part is started. Previously described sequence is repeated as many times as there are new control points to be set. When there are no new control points, the generator enters the stop state, where reference velocity is set to zero and the very last control point is being set as the ending point of the whole path.

Progress speed of the path generation is controlled by controlling the pace of the s rising from zero to one, as presented in section 2.7. In order to control the desired path-following velocity in time domain, the rate of s needs to be normalized. In the thesis, the normalization is conducted with respect to the desired path velocity and first derivative of the current path piece that is currently being generated. In practice, this provides the possibility to set a certain desired path generation speed for each path piece separately, and the velocities can be interpolated with respect to the progress of the path parameter to provide smoother velocity transformations. These properties are significant steps towards more advanced path-following control. However, this kind of normalization only generates the path independently in open loop with the predefined set speed and does not take into account how accurately the current localized pose of the robot matches, in fact, with the generated pose. For more on the subject, see the concluding chapter 5.

3.5 Path-Following Controller

Path-following controller implemented in the study is based on equations (2.42-2.43) presented in subsection 2.6.2. The controller receives as inputs the desired pose (x_d , y_d , θ_d) and velocity of the robot (v_d) at a certain specific time (see figure 37). Based on the desired inputs and current pose of the robot (x , y , θ) received through the localization, the controller adjusts the velocity (v) and rate of the heading (w) commands of the control point of the robot to drive the errors between the poses to zero.

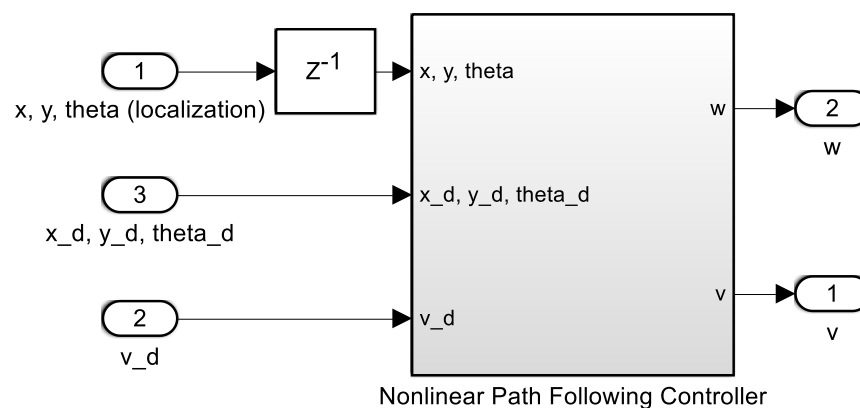


Figure 37: Implemented nonlinear path following controller.

The high-level structure of the implemented controller is presented in figure 37. In addition to the previously described, a delay is added to the localization signal. The purpose of the delay is to avoid algebraic loops during the simulation, and to some extent add more realism into the system. The delay is set to 20 ms.

3.6 Inverse Kinematics Controllers

3.6.1 Articulated-Frame-Steering

Inverse kinematics control for the AFS vehicle Ponsse Caribou S10 are implemented based on equations (2.6) and (2.7). The implemented Simulink structure is presented in figure 38. Actuator limitations are considered by saturating and rate limiting angular velocity commands in both steering (output 3) and driving (outputs 1 and 2) control. Inputs of the inverse kinematics are the path-following controller's outputs for linear (v) and angular (w) velocity of the control point.

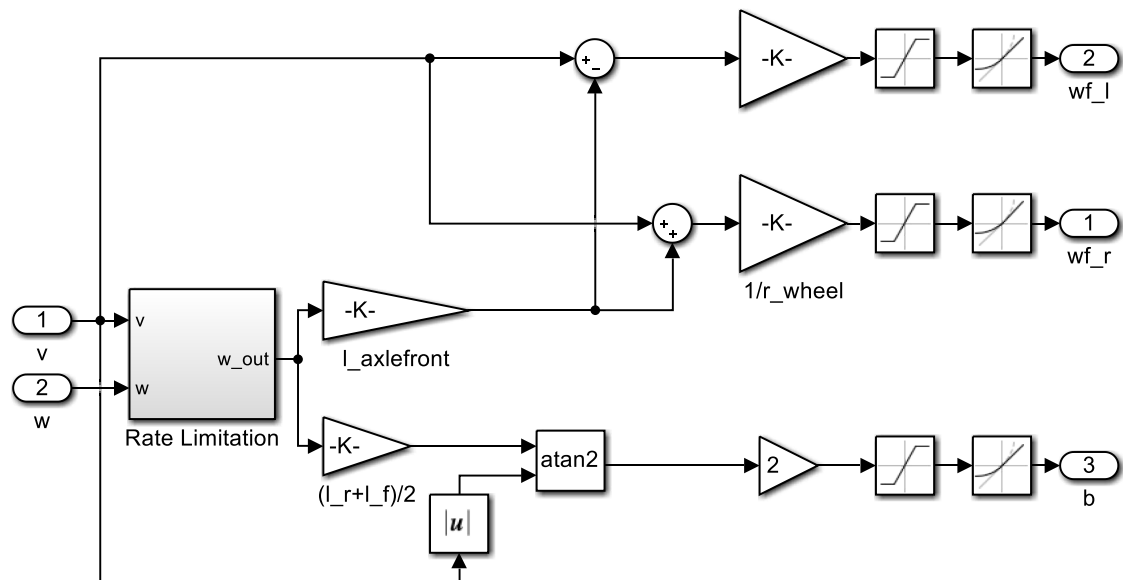


Figure 38: Inverse kinematics controller designed for AFS.

Purpose of the rate limitation block is to constrain the output heading rate based on minimum turning radius of the vehicle. As presented in section 2.1, the turning radius of the control point is proportional to the ratio of the velocity and rate of heading, respectively. As this ratio approach to the pre-defined minimum turning radius, the command for the rate of the heading is constrained so that the high-level control commands do not exceed the structural limitations of the vehicle.

3.6.2 Car-like Steering

Inverse kinematics of Haulotte construct of two different sections. The first section designed for 2WDS is presented in figure 39. The control structures of the steering angles and angular rear wheel velocities are implemented using equations (2.8-2.10) and (2.1), respectively. Actuators velocity and acceleration limitations are considered similarly as presented in previous subsection. Output 2 represents the angular wheel velocity commands. Steering commands for the wheels are given by the output 1.

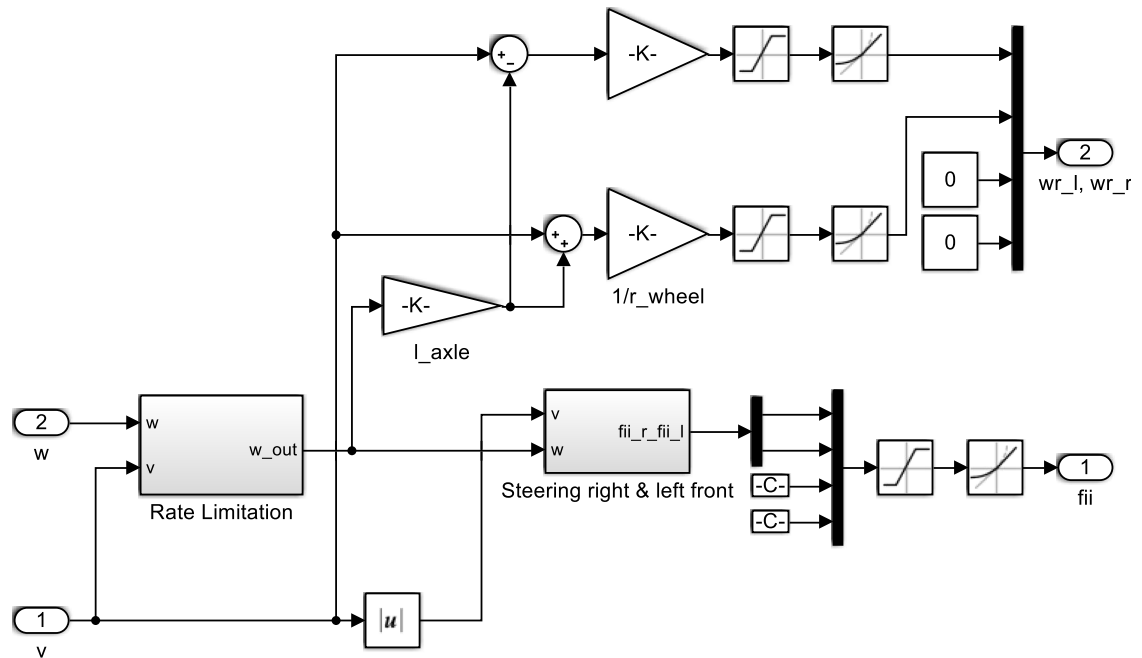


Figure 39: Inverse kinematics controller for 2WDS car-like steering structure.

The rate limitation of the car-like steering is presented in figure 40 on the following page. In addition to previously presented in subsection 3.6.1, the rate limitation of the car-like steering functions also as a block, which enables the 4WDS mode of the robot, when the ratio between the velocity (v) and angular velocity (w) commands, respectively, gets a smaller value than what the initial minimum turning radius allows.

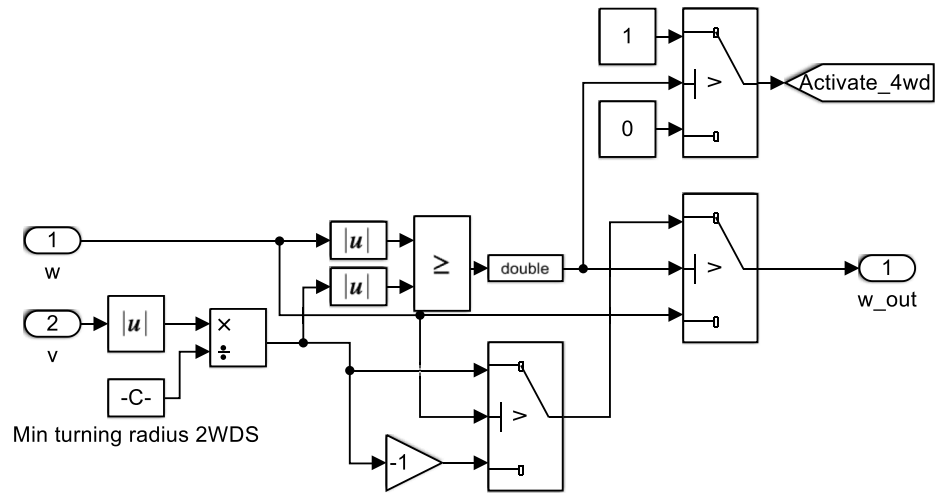


Figure 40: *Heading rate limitation and 4WDS activation.*

When the 4WDS is activated, inverse kinematics controller section 2 activates, and the steering angles and angular wheel velocities for all wheels are determined based on equations (2.8-2.10) and (2.1), respectively, while using the new control point setting at the middle of robot's longitudinal axle. The new CP setting also results in a new distance between the CP and wheel axle, as presented in subsection 2.1.3. The effects caused by these sudden changes of definitions during the path-following and potential future development suggestions on the matter are observed and presented in subsection 4.3.4.

4. Simulation Studies

4.1 Verification of Dynamic Simulation Models

Step and ramp input response simulation results of the modelled mobile robots are presented in this subsection. In order to verify the modelled HSTs in the absence of real measurement data, the results are compared to the previous studies of modelling of HSTs, the data gathered from the vehicles' datasheets, and to the calculated theoretical results, which are based on equations presented in section 2.2. Main results of the verifying process are presented in the following paragraphs.

Ponsse Caribou S10

With the traditional HST of Ponsse Caribou S10, the step input is used to control the displacement of the hydraulic pump. The displacement of the hydraulic motor is held at its maximum value during the whole experiment.

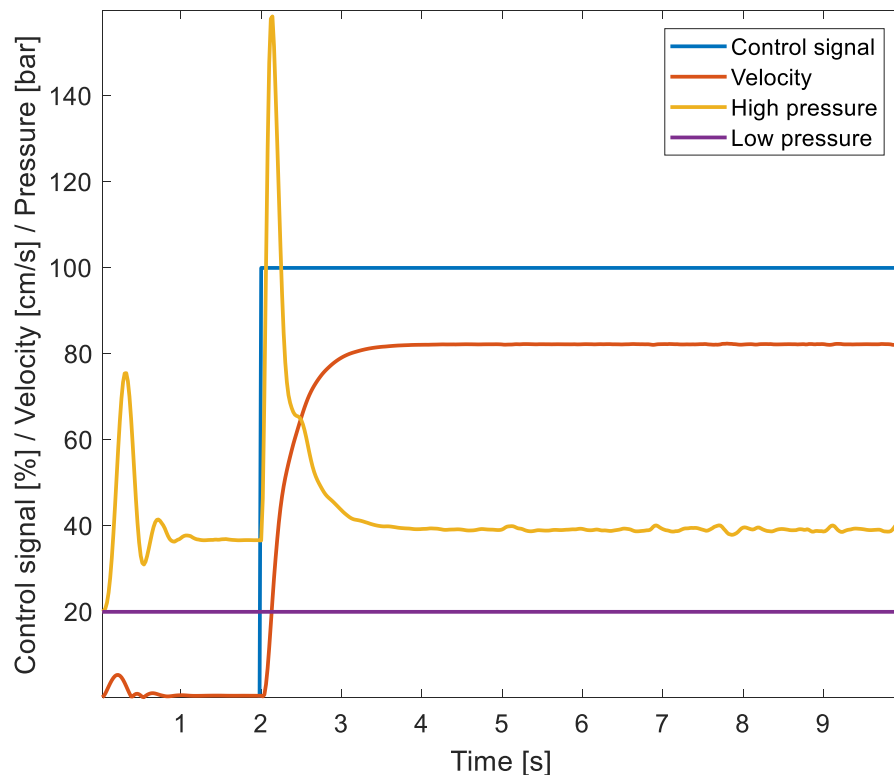


Figure 41: Simulation results of Ponsse Caribou S10 step input response.

The step input response of the model is presented in figure 41. At the 2 second mark, the control signal is set from 0 to 100 %. Based on the dynamics of the hydraulic pump, the displacement of the pump rises from zero to maximum as fast as possible. At the start of

the simulation, the initial system pressure is being set to 40 bar. When the control command of 100 % is set, the system pressure achieves a pressure peak of 159 bar. Due to the high gear ratio of 90, the needed torque input during the acceleration is low enough, so the system pressure never reaches the maximum pressure level of 340 bar. The pressure level on the low-pressure side of the closed circuit is a constant pressure of 20 bar.

Based on calculations in appendix E, theoretical maximum velocity of the vehicle in the low speed area is 0.83 m/s. When the variable displacement units function at their full displacements and the pressure difference over them is small during constant velocity, the leakages of the components are also small. Hence, the theoretical and simulated velocity can be seen to match with reliable accuracy.

In figure 42 a case is presented, in which varying the displacement of the hydraulic motor is incorporated into the previously presented step input scenario. After the step input response, the displacement of the hydraulic motor is reduced with a ramp function with inverse relation to the velocity as presented in section 2.2. The displacement is being reduced to a specific theoretically calculated point, where the velocity of the vehicle should be at its maximum velocity of 27 km/h. The calculation results are presented in appendix E.

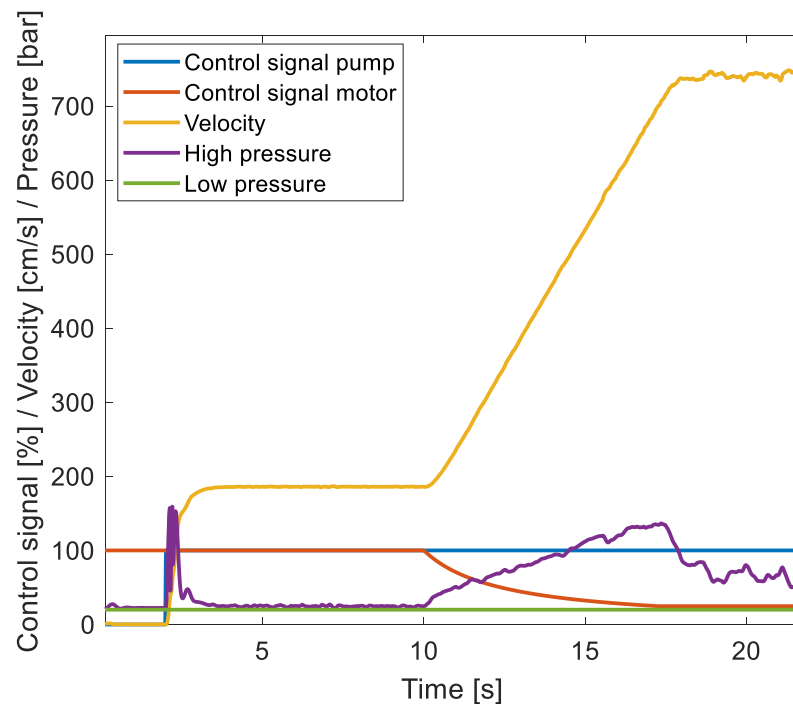


Figure 42: Simulation results of Ponsse Caribou S10 step and ramp input responses.

The open loop control of the displacement of the hydraulic motor is started at the 10 second time point. While the displacement is being decreased, the vehicle accelerates, and the system pressure rises due to the increasing torque demand. At the time point of 17.4 s, the displacement of the motor is saturated to a specific theoretical value, and the

velocity of the vehicle can be seen to reliably match with the theoretical maximum velocity of 27 km/h, which can be presented in a form of 750 cm/s.

Haulotte 16RTJ PRO

Simulation results of the step input response of Haulotte's 2WDS medium speed drive are presented in figure 43. In the simulation, a valve control signal is set from zero to 100 % at the 2 s mark. This implies that the valve spool is being moved from the closed position to the fully open position as fast as the dynamics of the valve allow.

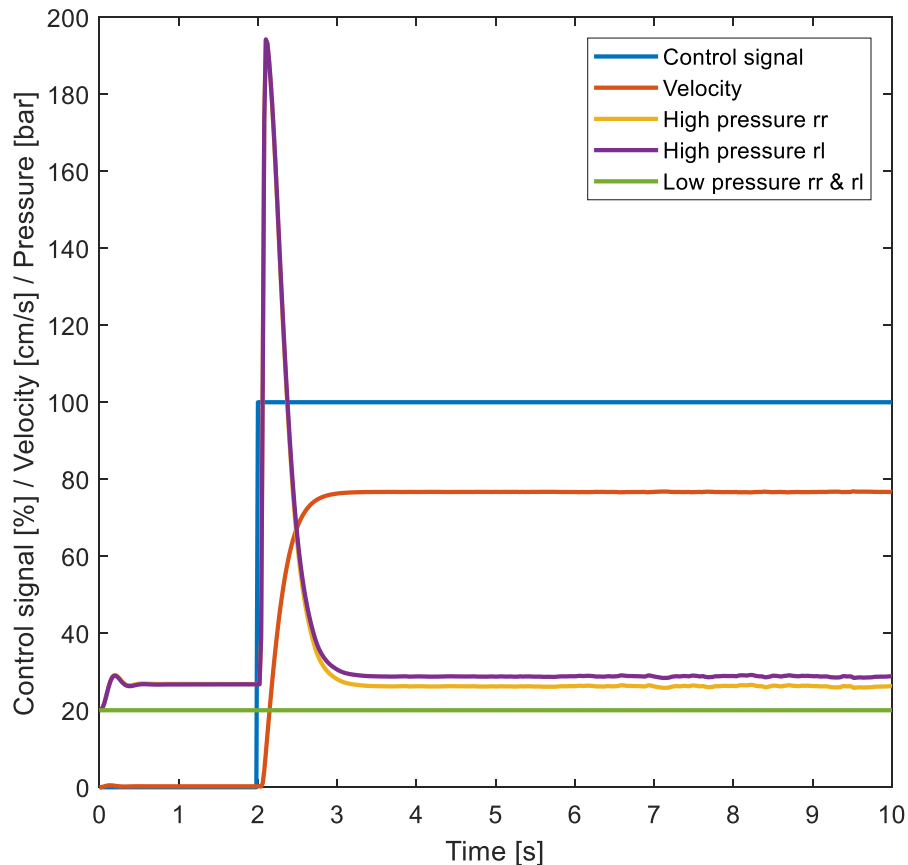


Figure 43: Simulation results of Haulotte RTJ16 PRO step input response.

The results show that the velocity of the vehicle increases to the maximum medium drive speed of 0.77 m/s, as is presented by the author in [15]. Therefore, when the vehicle achieves its maximum medium drive speed with full opening of the valve, and the displacement of the fixed hydraulic motor is known, the nominal flow parameters of the valve can be reliably considered to be correct. The pressures on the high-pressure sides of both rear right rr and rear left rl can be seen to be reliably same. The shape of the pressure curves can be seen to follow the same form as in other researches, which have focused on modelling of HSTs [30, 31]. The low pressure on both of the circuits is been held at constant pressure of 20 bar. According to [15], the maximum system pressure of the HST is 240 bar. As can be seen from the figure, when the vehicle accelerates as fast

as possible, the high pressure reaches a peak pressure of 195 bar, and, thus, the maximum system pressure allowed is not being exceeded.

4.2 Verification of the Open Loop Control

Verifying the high-level inverse kinematics and the robot models under open loop path-following and low-level control is divided into three different scenarios. The first scenario is the forward drive, followed by scenarios of turn left and turn right. More simulation results of the open loop control verifications are tabled in appendix F.

In the first scenario, a specific velocity profile is given for the inverse kinematics and the command for the rate of the heading is set to zero. The inverse kinematics calculates the angular wheel velocity commands and sends them to the low-level actuator controllers. The low-level controllers compare the velocity commands and the measured angular wheel velocities of the vehicle and control the actuators responsible for the velocity adjustment to reach and maintain the desired velocity profile.

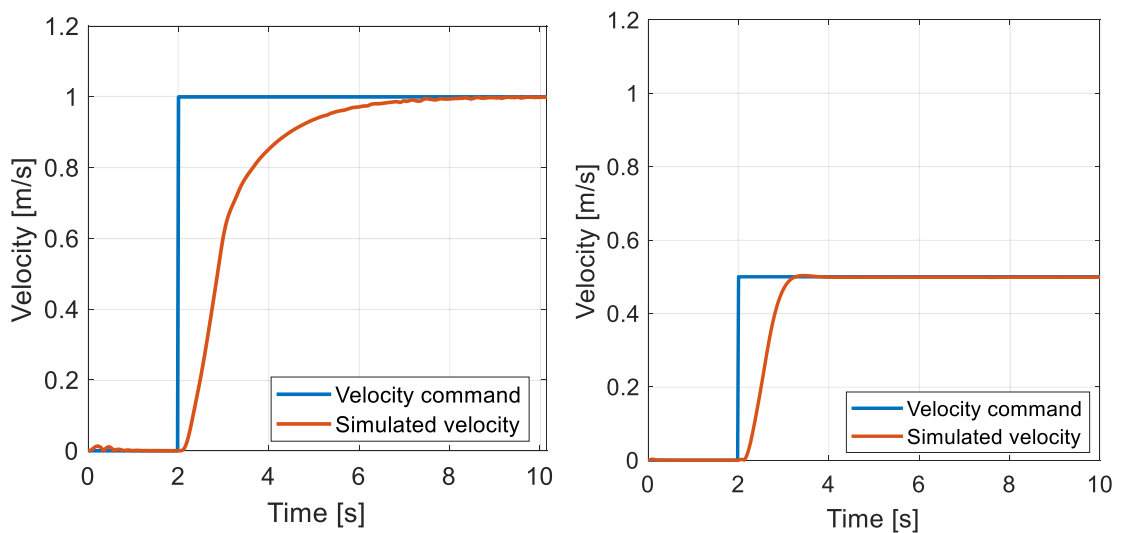


Figure 44: Example case simulation results of the forward drive scenario with low-level control. Result of Ponsse Caribou S10 on the left and Haulotte 16RTJ PRO on the right.

Example simulation results of the low-level velocity control are presented in figure 44. In this forward drive case, a constant velocity command was set to the IK controllers and the actuators low-level controllers' response was monitored. As results show, at first the low-level controllers adjust the actuators to produce a fast acceleration to achieve the command velocity. Then, the actuators are controlled to minimize the steady-state error.

The second scenario designed to verify the models is called the right turn. In this scenario, verifying the models is continued by taking into account the effects caused by direction change. Hence, in addition to the velocity profile, the inverse kinematics receives a profile for the rate of the heading as well. From this point forward, the control chain functions

similarly as explained in the previous section, but in this case the low-level controllers used for controlling the actuators effecting on the steering of the vehicle are also enabled.

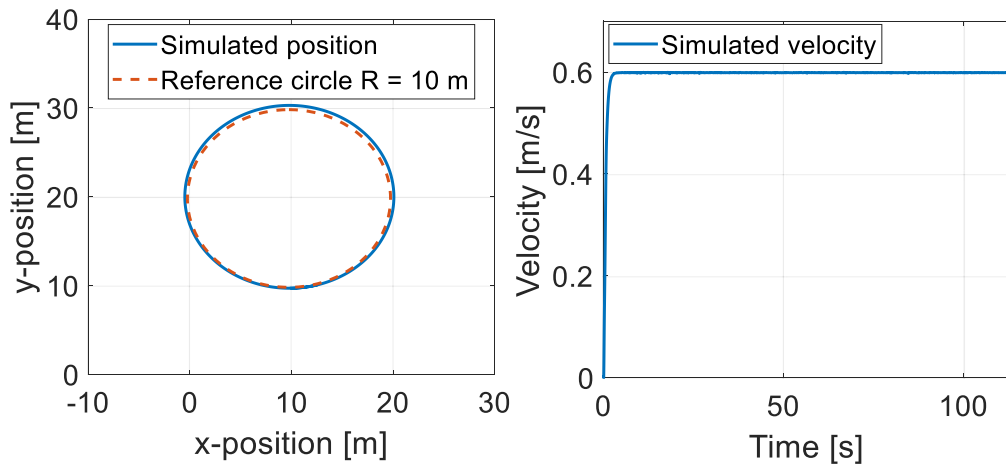


Figure 45: Example simulation results of the scenario 2. Simulation results of Haulotte RTJ16 PRO with command velocity 0.6 m/s and rate of heading 0.06 rad/s.

Example simulation results of the scenario is presented in figure 45 with Haulotte case sample. From the results can be seen how the low-level controllers succeeded in maintain the desired speed command, and how the simulated open loop path is close to the mathematically calculated ideal reference path. The slight difference in the turning radius is being caused by the imprecise dimensioning of the steering structure, which causes the wheel steering angles not to be perfectly based on Ackermann steering geometry presented in equations (2.9) and (2.10). Thus, during open loop control the wheels are slipping, which causes the vehicle to push while cornering and, therefore, results in a circle path longer than the ideal reference path. The opposite effect of the imprecise steering structure dimensioning can be seen in the turn right scenario results of Haulotte presented in appendix F. When the steering angle is measured from the right wheel while turning to both steering directions, in turn right scenario this causes the steering angle of the left wheel to be oversteered. This results in an open loop path with smaller turning radius compared to the theoretical calculations.

Properties of the third scenario are similar compared to the right turn, but in this scenario the robots are controlled to turn left. This scenario is useful for proving that under constant circumstances the control commands for turning with the same velocity and magnitude of the heading rate causes the absolute values of the turning radii to be equal towards both steering directions.

In figure 46 is presented a turn right open loop case of Ponsse Caribou S10. In this simulation, the velocity of the vehicle was controlled to gain and maintain a constant velocity of 0.5 m/s and the rate of the heading command was set to 0.1 rad/s. In addition to the low-level control, the effect of the rate of heading limitation can be seen to have an effect. Based on the vehicle's datasheet [17], the maximum articulation angle of the vehicle is

45 degrees. With the commanded velocity and rate of heading, the desired circular path would have a smaller turning radius compared to the minimum turning radius of the vehicle. Thus, the steering command is saturated during the simulation to command the vehicle to turn with an articulation angle of 45 degrees. For this angle, the reference turning radius of the vehicle is 5.97 m, based on the mathematical equations presented in chapter 2.

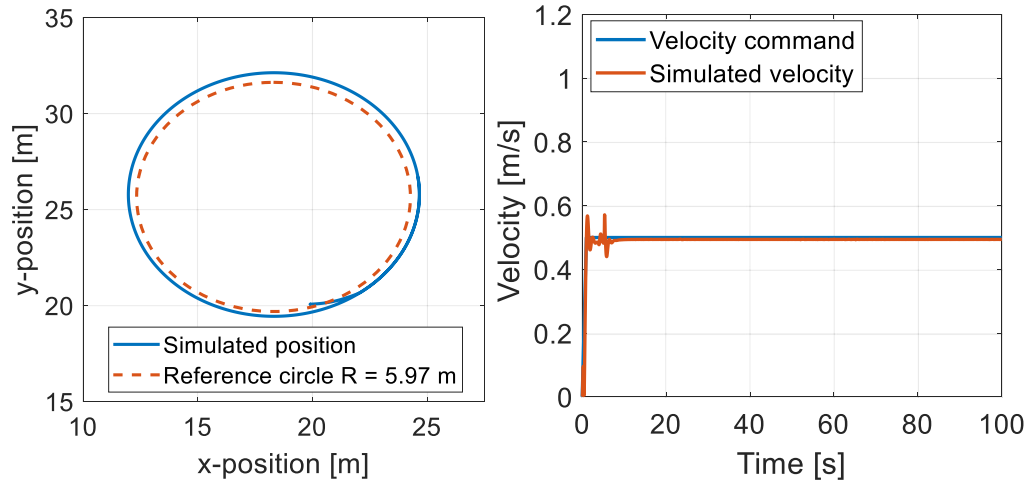


Figure 46: Simulation results of an example case of Ponsse Caribou S10 in the turn left scenario.

Secondary control of the traditional HST was used in this scenario. As the results show, the low-level PID controller adjusts the displacement of the hydraulic motor accordingly, so that the desired velocity value is reached and maintained. The simulated turning radius of the vehicle is 6.4 m. The 43 cm difference between the reference and simulated radii can be explained by the side slipping of the vehicle's wheels. As presented in chapter 2, side slipping of the wheels is inevitable with many steering structures, as it is in AFS. The reference turning radius is ideal and does not take the slipping into account. With the dynamic vehicle model, small amount of wheel slipping is always present. Thus, while turning, the vehicle would be needed to be oversteered, so that the ideal reference radius would be achieved. This phenomenon is present in all the open loop turning scenarios of the vehicle, which are presented in appendix F.

4.3 Closed Loop Control Examination of Path-Following

4.3.1 Path-Following on a Well-Behaved Path

Example results from the path-following control under well-behaved path curvatures are presented in this subsection. In practice, this means that the physical constraints of the robots are taken into account during the path generation. The controllers' response and behaviour of the robots driving and steering actuators are the main objects which effect on the preciseness of the path-following under constant and flat ground profile. More

overall path-following simulation results are presented in appendices G and H. Furthermore, simulation results including visual features were also generated.⁴

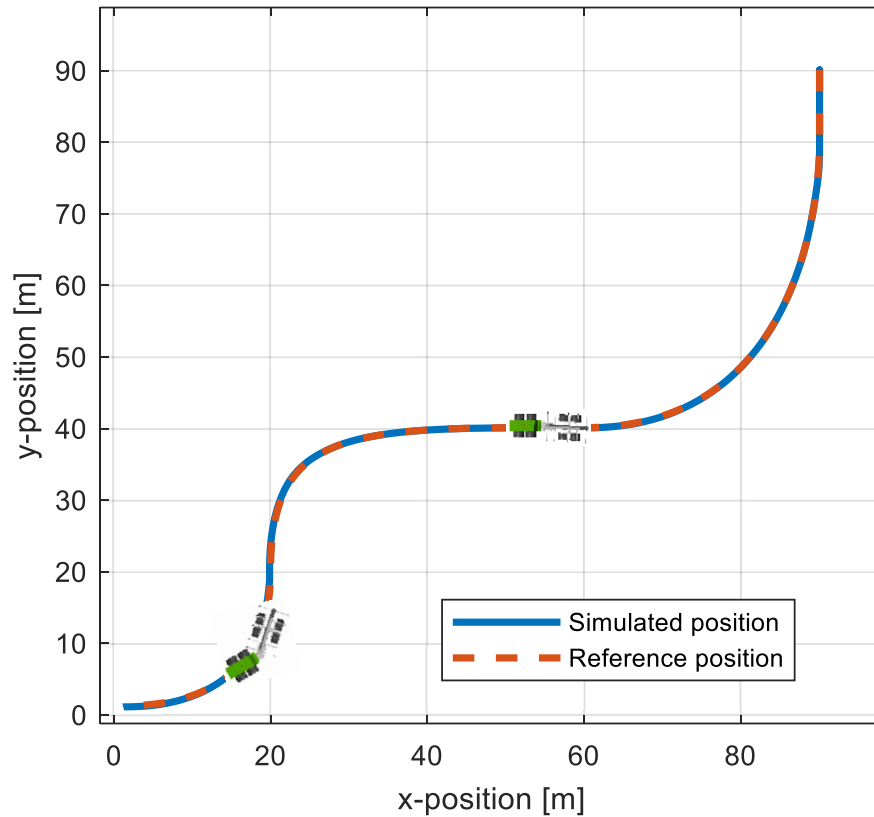


Figure 47: Path-following results from an example case of Ponsse Caribou S10 under well-behaved path curvature.

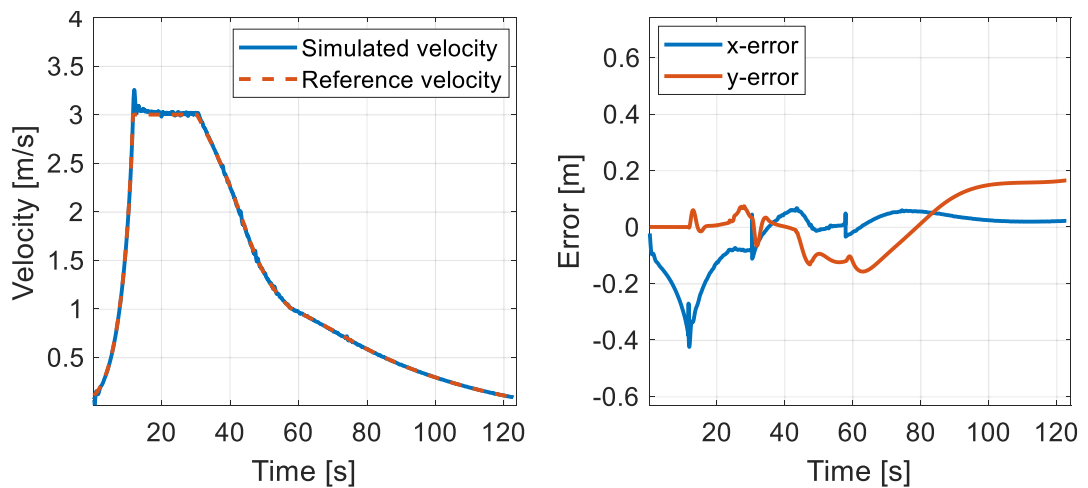


Figure 48: Simulated and reference velocity profile and measured errors of the simulation presented in figure 47.

⁴ Ponsse Caribou S10 Autonomous Path-Following: <https://youtu.be/TF0MCzMu0B0>

Simulation results from a specific path-following scenario of Ponsse Caribou S10 are presented in figures 47 and 48. The reference path and the actual path driven by the robot are presented in figure 47. As the results show, during well-behaved path curvature and constant ground profile the robot follows the reference path accurately with an absolute maximum normal y error of under 0.2 m. Furthermore, the mean absolute lateral y error is 8 cm during the whole path. When the velocity between the control points is interpolated, the simulated velocity profile proved to be smooth and accurate with respect to the reference velocity, thus resulting in a tangential x error less than 0.45 m during the whole simulation. The mean absolute longitudinal x error is 6.5 cm. During the simulation, the velocity profile varied between 0 and 10.8 km/h.

Similar path-following scenario results of Haulotte are presented in figures 49 and 50. At first, the vehicle is driven through a well-behaved path curvature which causes no problems for the controllers to handle. Next, path generator's progress speed is increased with respect to the path parameter to generate the path at maximum reference speed of 1.3 m/s, which is very near at the maximum velocity of the vehicle's maximum high-speed drive of 5.6 km/h.

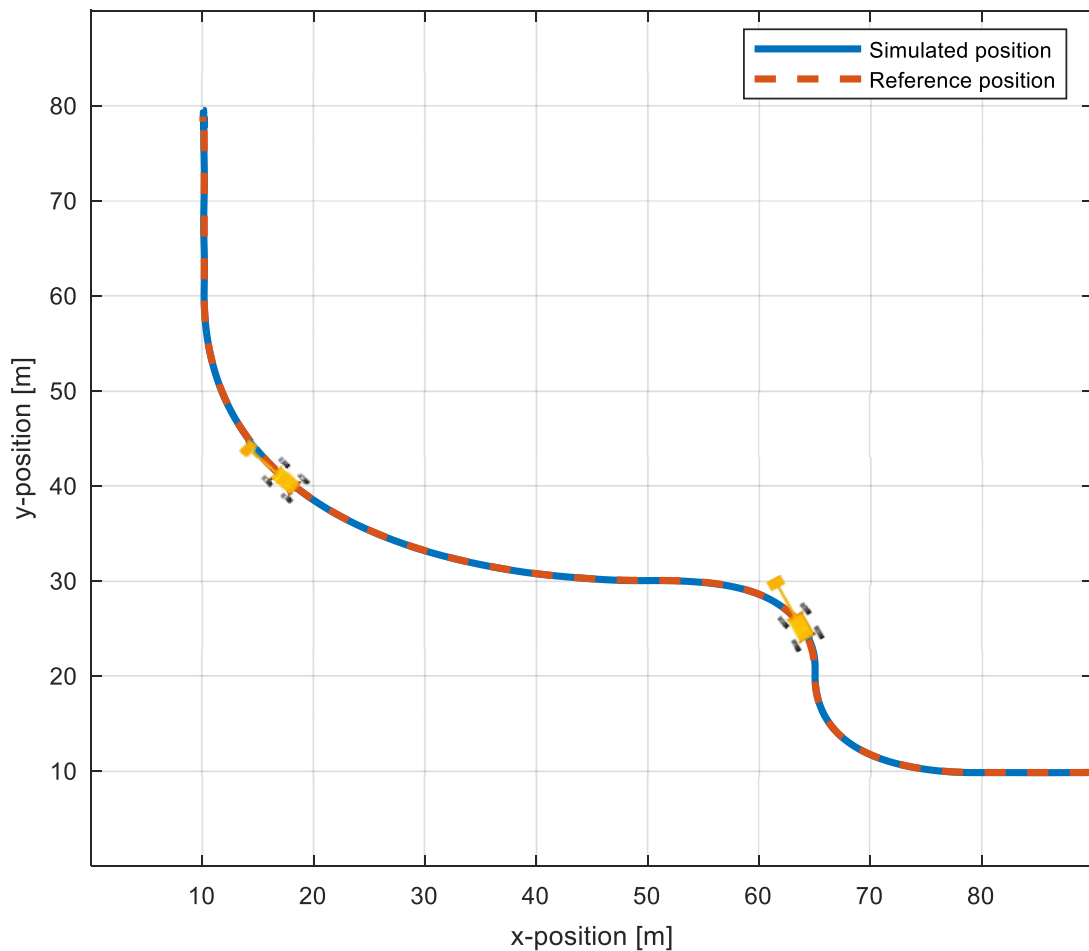


Figure 49: Path-following results from an example case of Haulotte under well-behaved path curvature.

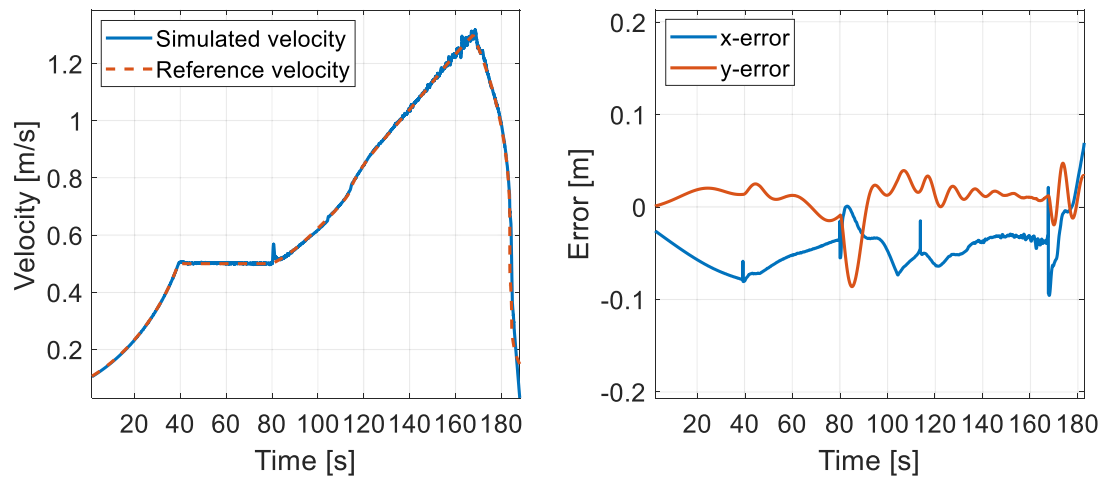


Figure 50: Simulated and reference velocity profile and measured errors of the simulation presented in figure 49.

Path-following results of Haulotte under well-behaved path curvature are excellent. Due to the low speed range of the vehicle and constant ground profile, path-following controller has no problems to accurately control the velocity and heading of the vehicle. Position errors can be seen to be less than 0.1 m during the whole path. Due to the reference velocity interpolation, the accelerations and decelerations of the robot are smoothly executed, which results in a low longitudinal x error and accurate end positioning of the robot. The mean absolute lateral y and longitudinal x errors of the simulation are 2.3 cm and 4.7 cm, respectively.

4.3.2 Path-Following with Bounded Steering Actuators

Path-following in a case of steering angle saturation is a critical scenario to simulate. Saturation of the steering angle during a tight turn will cause the vehicle to turn with a wider turning radius compared to the generated path. This will cause the following errors to grow and the vehicle to depart from the desired path. This kind of simulation scenario will provide answers for at least to the following question: will the vehicle return on the path when the steering control is no longer saturated, and if so, how fast, accurately, and smoothly.

Structural steering limitations and simulation results of this kind of scenario of Ponsse Caribou S10 can be seen from results presented in figure 51. In the figure, simulated and reference position and the specified steering saturation section of the path are presented on top left and right, respectively, and simulated and reference velocity and measured position errors are presented on bottom left and right.

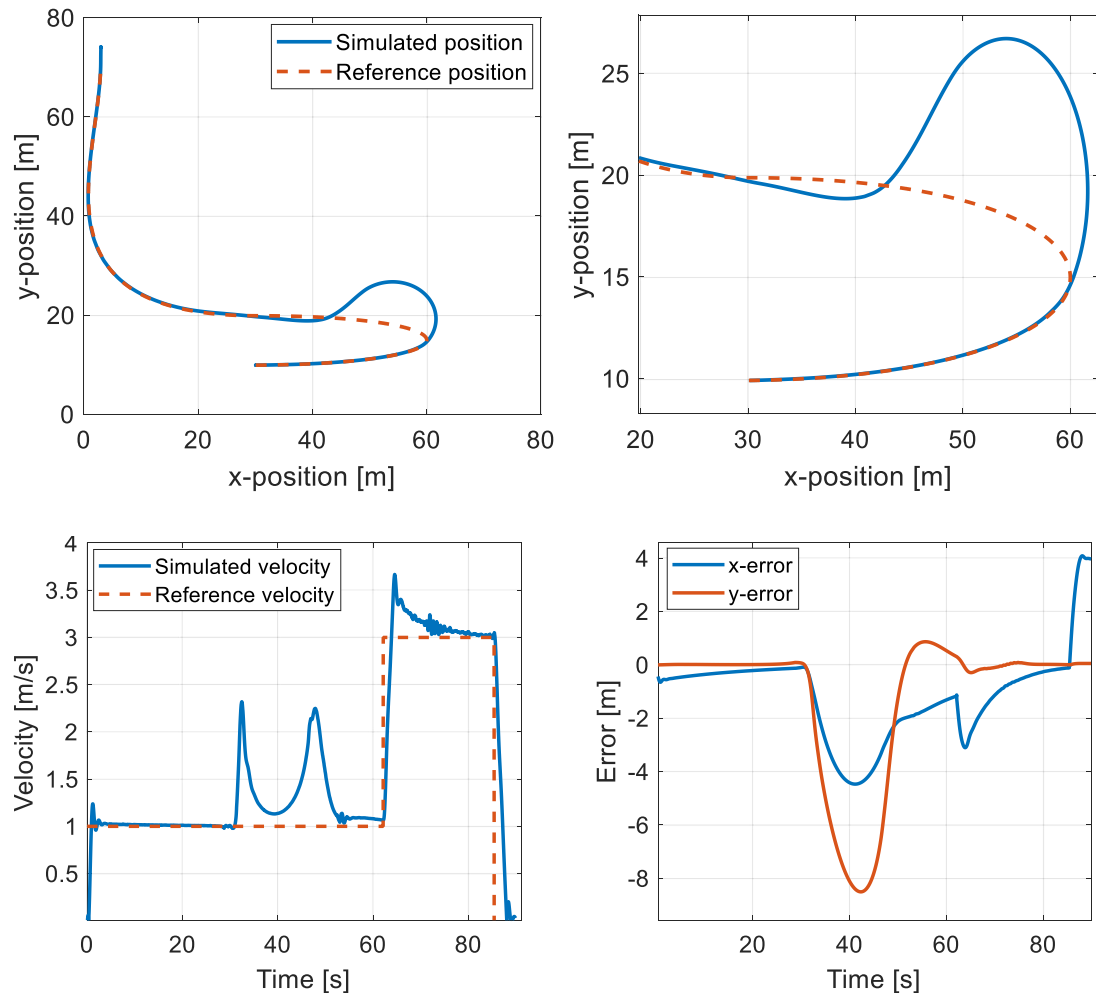


Figure 51: Steering saturation example simulation results of Ponsse Caribou S10.

In this case, a poor path was designed where the minimum turning radius of the vehicle was not considered. This caused the robot to deviate from the path at $[x, y]$ location of $[60, 15]$. When the robot deviated from the path due to the structural steering limitations, high-level inverse kinematics control set the steering angle command at maximum. At point $[50, 26]$, the structural limitations no longer affect, and path-following control adjusts the command signals for the robot to return on the path. From this point forward, the robot took approximately 8 s to return on the path. Due to the highly tuned tangential error control gains, an overshoot of 0.8 m can be seen after the returning. However, no oscillation can be seen after this and the robot continues accurate path-following. The longitudinal overshoot at the end of the path due to the fast velocity reference transformation from 3 to 0 m/s causes the longitudinal x error to rise to 4 m at the end of the path.

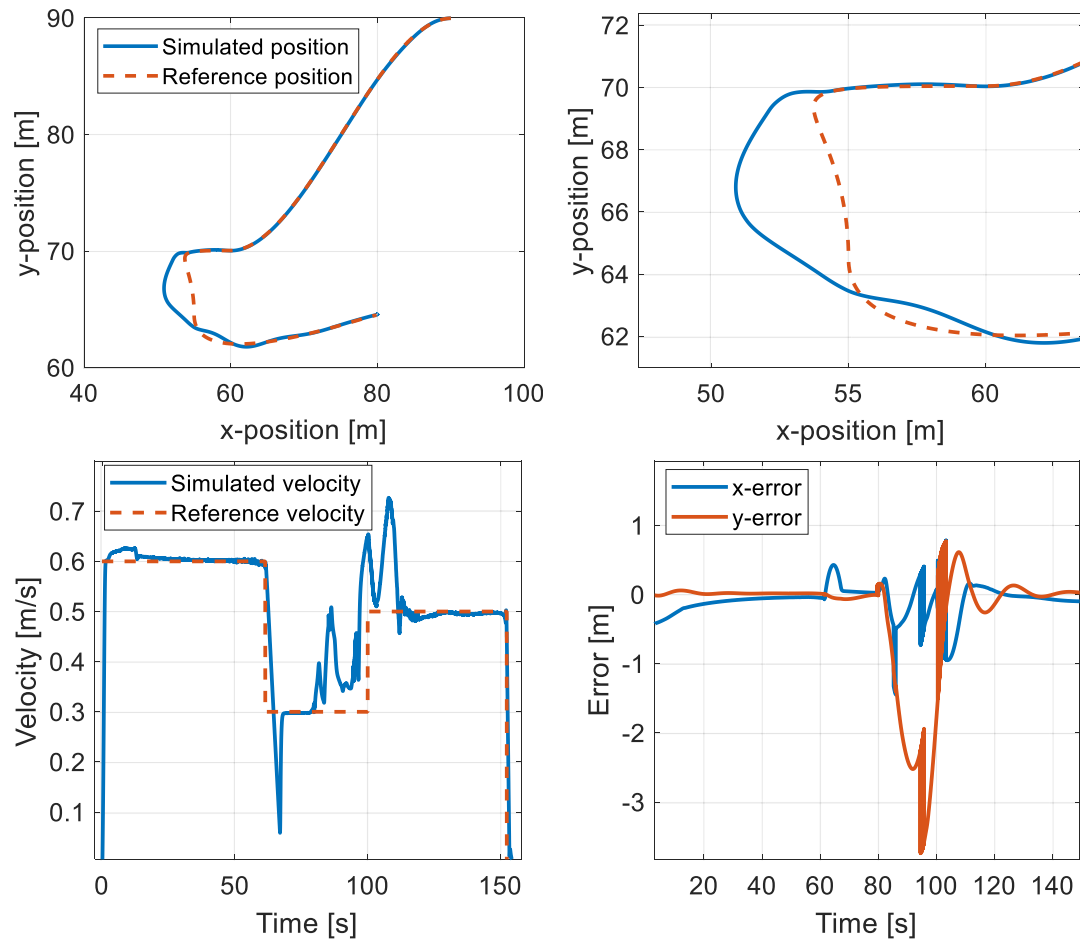


Figure 52: Simulation results of Haulotte's steering saturation case example.

Simulation results of a steering saturation example case of Haulotte are presented in figure 52. From the results can be seen, how the 4WDS mode activated on the tight cornering situation at the location of [53, 69]. Even when the 4WDS provides the vehicle a better opportunity to stay on a tight curvature path, in this simulation the path curvature was nevertheless too strict, and magnitude of the lateral y error increases up to 4 m. The vehicle continues to turn with its minimum turning radius, until it is able to continue following the path. A small oscillation with lateral error magnitude less than 0.5 m can be seen in the error figure before the robot continues precise path-following.

In overall, the example and multiple results show that the robots manage to continue accurate path-following after steering saturation. However, one negative property of the current solution can be seen from the vehicles' velocity profiles. When the path-follower realizes that the robot is falling behind, ergo the x error increases, it commands the vehicle to accelerate, as can be seen, for example, from the velocity in figure 52 at the time point of 80 s. During a tight cornering situation, this can be seen as an unwanted property. The reason for this behaviour is the constant progress of the path generation, where the path is being generated with constant speed independent of the vehicles' actual position. Thus, an advanced communication and control between the path generation and path-follower controller is a crucial factor to be considered in the future development. For more on the

subject, see the concluding chapter 5. More simulation results of the steering saturation case are presented in appendices G and H.

4.3.3 High-Speed Path-Following

Simulating the model under high desired velocity profile is a scenario designed for observing the effects of constant gain values of both high- and low-level controllers under highly varying velocity commands. With this kind of case, it is reasonable to monitor how accurately the nonlinear path-following controller succeeds in path-following control when the desired velocity of the vehicle varies significantly, and if there is a need for specific gain scheduling based on different velocities and path curvatures. Due to the low maximum velocity of Haulotte, all high velocity path-following scenarios are conducted with the AFS Ponsse Caribou S10 forwarder. In this study, it is notable to declare that the term high velocity is used while talking near maximum velocities of Ponsse Caribou S10, approximately from 14 to 25 km/h.

Results of path-following controller's response in a case of driving fast through a relatively tight path curvature are presented in figures 53 and 54 on the following page. In the scenario, the robot was commanded to start motion and accelerate to a velocity of 18 km/h and after that drive through a left turn while decreasing the velocity for the next curve, and then until the end of the desired path. When structural limitations of the robot are not exceeded, results demonstrate that the controller's response is fast and accurate enough. The maximum normal error with magnitude of 0.57 m was caused by the tight curvature after the high velocity path-following, approximately in a point of [70, 115]. During the high-speed cornering, the nominal lateral y error was less than 0.1 m. The mean absolute errors of the simulation for y and x are 12 cm and 13 cm.

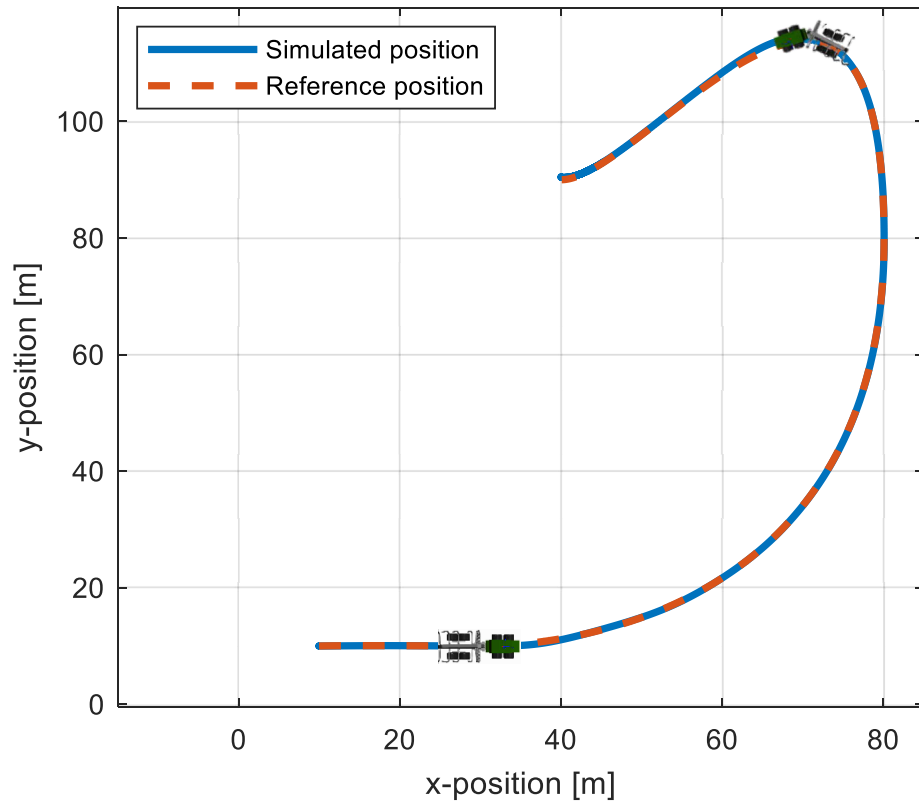


Figure 53: Simulated and reference position from a high velocity variation path-following example scenario of Ponsse Caribou S10.

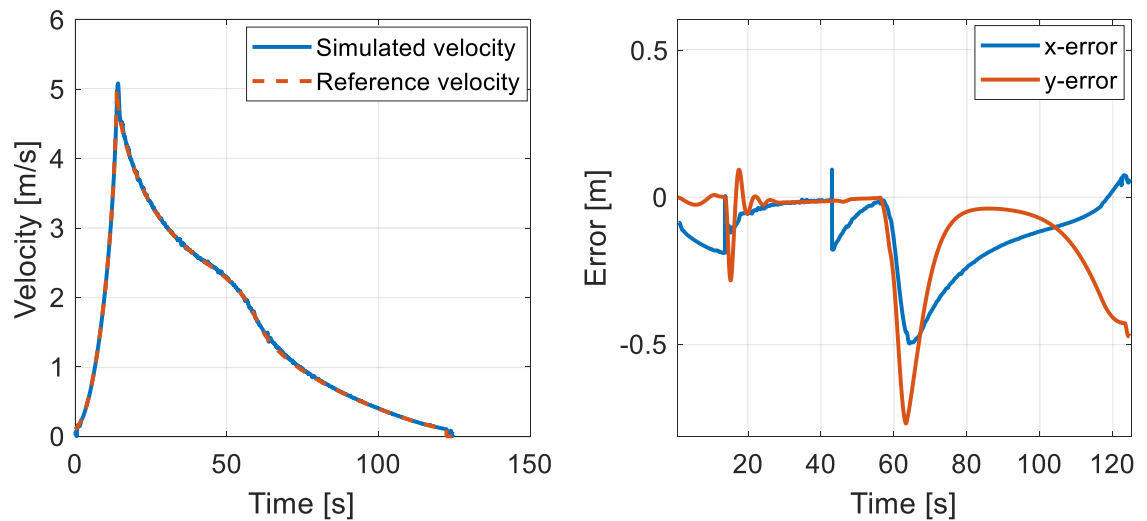


Figure 54: Simulated and reference velocity and measured position errors from a high velocity variation path-following scenario presented in figure 53.

Another high velocity path-following scenario results of Ponsse Caribou S10 are presented in figures 55 and 56.⁵ In this case, it is important to notice the scale of the generated path with respect to the previously presented case. In this simulation, all path curvatures possess turning radii of more than 10 meters. Effects of this can be seen straight from the normal y error results, where the error never exceeds a value of 0.20 m. The mean absolute y and x errors of the simulation are 1.5 cm and 4.7 cm, respectively.

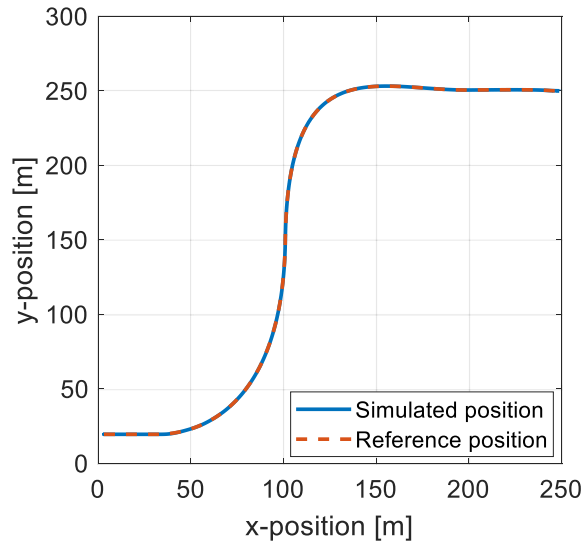


Figure 55: Simulation results from a high velocity variation path-following example scenario of Ponsse Caribou S10 under high path curvature radii.

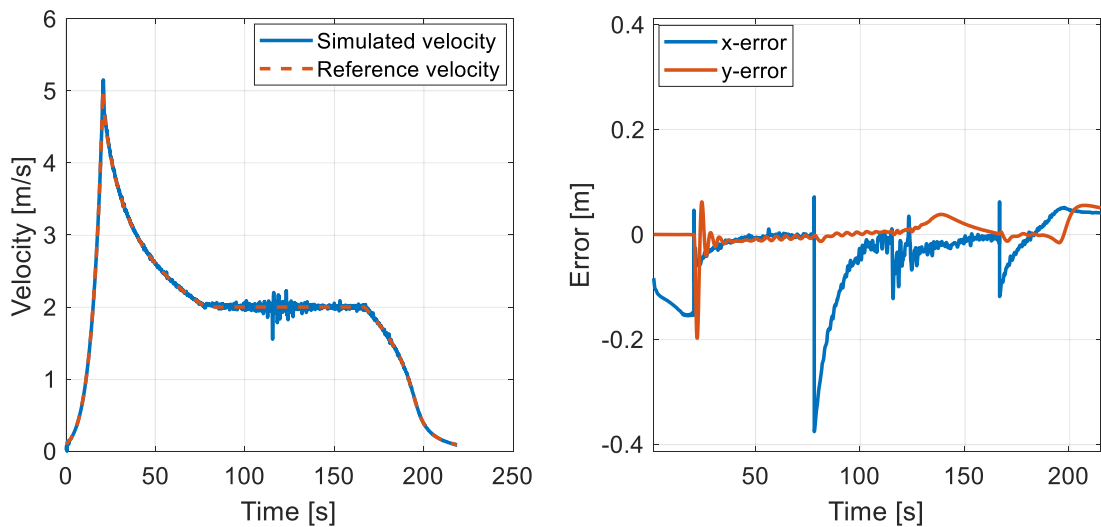


Figure 56: Simulated and reference velocity and position errors from a high velocity variation path-following scenario presented in figure 55.

Simulation results of the scenario prove the effectiveness of the controllers during high velocity variation under simulation environment. During well-behaved path curvatures, high velocities proved to not be an issue for the PF controller, which was able to adjust the heading rate and velocity to also maintain a tangential x error less than 0.5 m during most of the simulations.

⁵ Ponsse Caribou S10 Autonomous High-Speed Path-Following: <https://youtu.be/jL8CxCWkitY>

4.3.4 Four-Wheel Drive and Steering and Path-Following

Four-wheel steering is a massive advantage during tight cornering situations where the robot is desired to turn on a strict area. Simulation results from a full 4WDS scenario of Haulotte 16RTJ PRO are presented in figures 57 and 58. An illustrating video of the exact simulation case was also generated.⁶

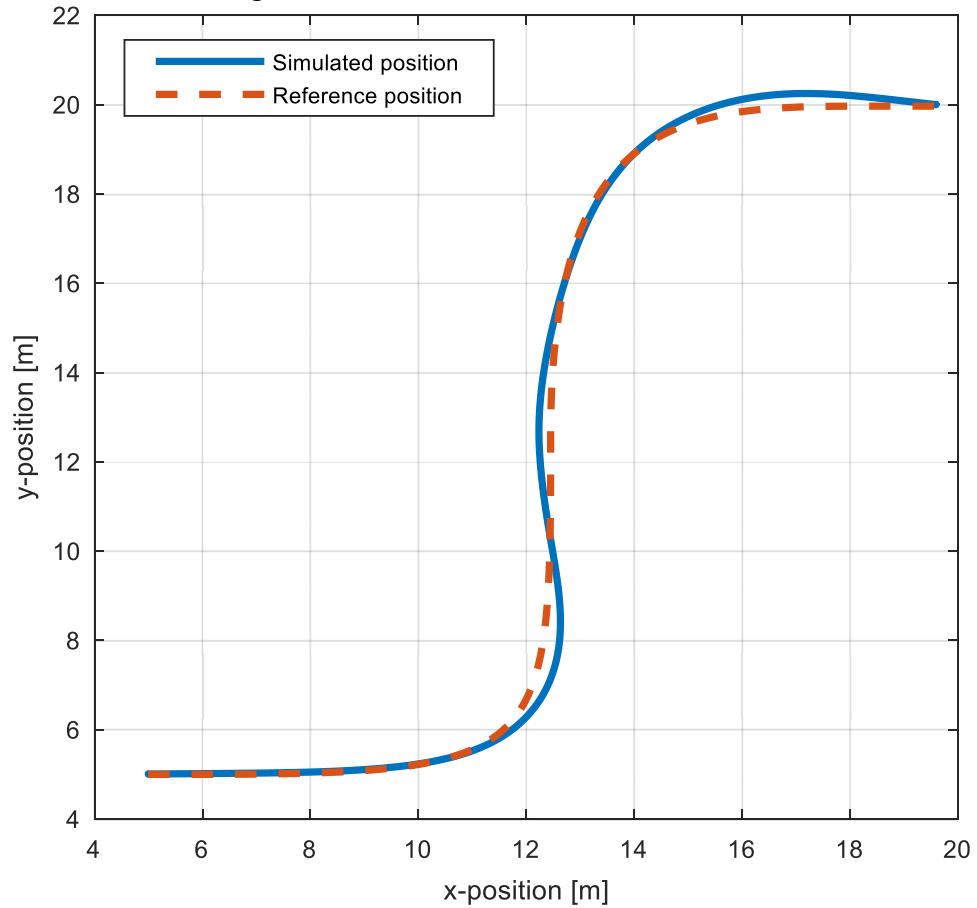


Figure 57: Simulated and reference position of the robot during 4WDS.

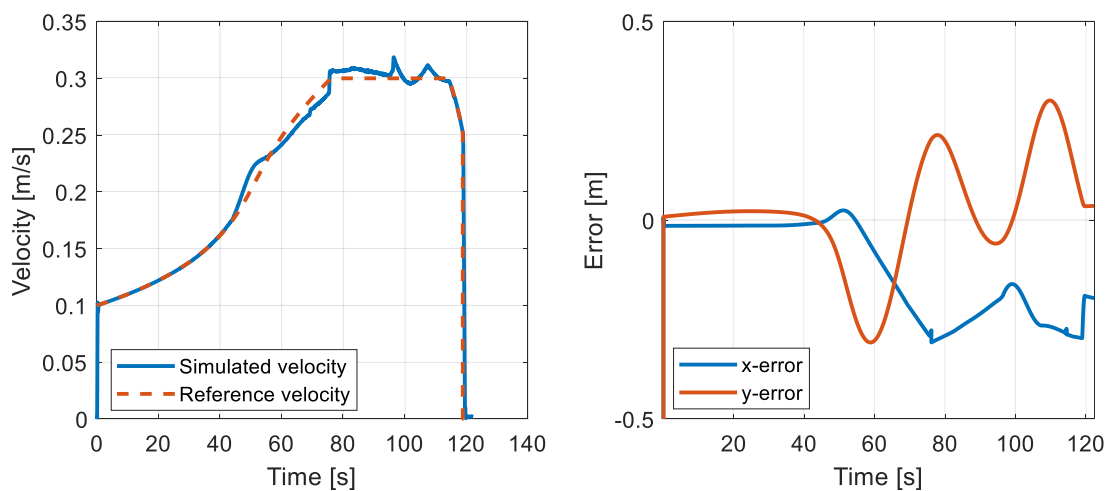


Figure 58: Simulated and reference velocity and position errors of the simulation case presented in figure 57.

⁶ Haulotte 16RTJ PRO 4WDS Autonomous Path-Following: <https://youtu.be/zTwpnINJfFo>

The results show that in a turn with radius of approximately 2.5 m the robot manages to follow the path with a lateral y error less than 0.3 m due to the ability of four-wheel steering. At the time of 80 s, the robot achieves its maximum 4WDS velocity, and steers through the second tight curve also with a lateral error less than 0.3 m. The mean absolute error values for the normal x and tangential y error are 12 cm and 17 cm.

Automating the selection of the controller between the 2WDS and 4WDS is designed for a scenario where the path is designed to have both tight curvatures and easy-drivable sections. An example simulation results from this kind of a path-following scenario are presented in figure 59. Simulated and reference position of the whole path and the 4WDS section are presented in top left and right of the figure, respectively. Simulated and reference velocity and lateral y position error are presented on bottom left and right.

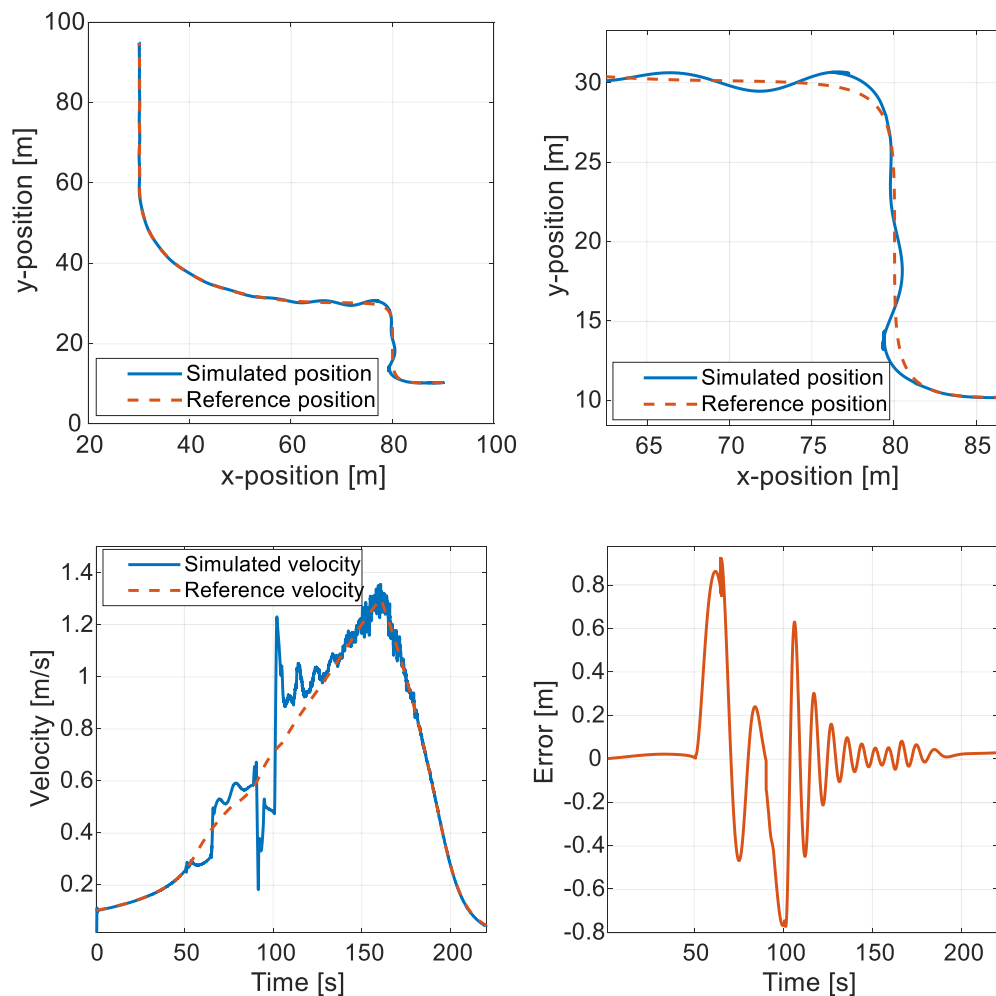


Figure 59: Simulation results from an example automated controller selection between 2WDS and 4WDS of Haulotte 16RTJ PRO.

At the start of the path, the robot starts the following with the nominal 2WDS control. When the robot enters the first curve, the desired turning radius of curve gets a value lower than the minimum achievable turning radius of the 2WDS. At this point, the control is automatically switched to synchronously control the velocities and steering angles of

all four wheels of the robot. Due to the use of the 4WDS, the robot manages to follow the path through the tight curvatures with a maximum lateral error magnitude of 0.8 m. When the curvature of the path is wide enough for 2WDS, the control is switched back to the nominal control, and rest of the path can be driven with higher velocity and accuracy. Even after the positioning error caused by the oscillation, the mean absolute lateral error of the simulation is 14 cm.

The path-following results of 4WDS prove that by the means of the mode the robot can drive through paths with lower turning radii. However, due to the sudden change of the control point from the rear wheel axle to the centre of the longitudinal axle, the position errors increase. One solution for the problem could be modifying the path planning to produce paths, which take the change of the CP into account and continue the path-following from the exact point where the new CP is currently located.

5. Conclusions and Future Work

Objectives of the thesis were to develop a simulation model for two different types of heavy-duty vehicles, to design high-level controllers based on inverse kinematics for commanding their driving and steering actuators, and to analyse the closed-loop behaviour of the vehicles using well-known path-following methods. The model was generated under Matlab Simulink and Simscape Multibody Dynamics environments. The thesis constructed of three main sections: theory, modelling, and simulation.

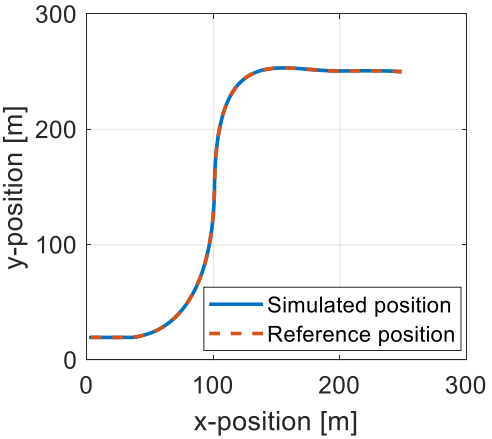
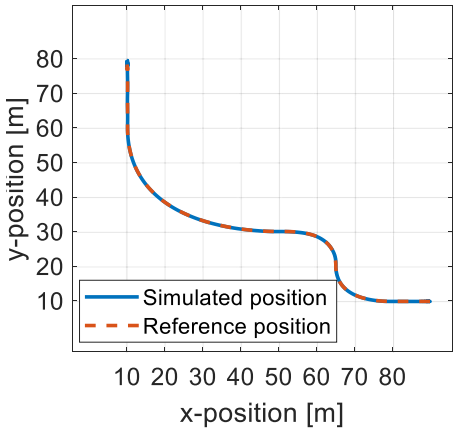
Mathematical representations and crucial mechanical structures of the vehicles with respect to the modelling were presented in chapter 2. Understanding kinematics of several steering architectures was a crucial factor for design of the high-level inverse kinematics controllers. Main objectives in designing the inverse kinematic control were to provide a synchronous and coordinated motion control of the vehicles' actuators and a solution, which could be used together with generic path-following controllers. Profound knowledge on hydrostatic power transmission and hydraulic modelling were needed for modelling the internal dynamics of the vehicles. Furthermore, understanding the different mechanical interactions among the vehicles components and environment was crucial during the implementation of the physical robot models.

Modelling of the system was presented in chapter 3. The control system architecture was divided into four main modules: Control Points from Database, Path Generator, High-level Controllers and Vehicle Models. The theories and definitions presented in chapter 2 were utilized at this implementation phase. Control Points from Database was intentionally detached from other modules to visualize the possibility for wireless communication of the path control points with any external source. To keep the path mathematically valid, it passes through the path generator to supply desired set points at each control instance. The controller drives the vehicle dynamics toward the desired values based on the internal feedbacks and –artificially generated – localization feedback. Comparison of the dynamic model outcome versus the desired path and velocities are subjects of study for chapter 4.

Simulation studies were conducted in chapter 4. At first, the HSTs of the robots were verified at some level by comparing the simulated results to the data provided by the manufacturers, calculated theoretical values, and publications concerning modelling of hydrostatic transmissions. Next, open loop path-following scenarios were driven to observe the behaviour of the robots and low-level actuators' control and to validate the simulations. Finally, the path-following controllers were tuned, diverse challenging path-following scenarios were simulated, and behaviour of the robots were examined thoroughly.

The results showed that control succeeds in following paths with well-behaved curvatures on steady ground profile with admirable accuracy. Maximum error of the entire system in lateral positioning stays lower than 0.2 meters, while the mean errors during the simulations were less than 0.10 m (see subsection 4.3.1). Especially for a heavy-duty vehicle such as Ponsse, tracking error of 0.1 m is less than 10 % of the wheel axle length and 5 % of its full length. Maximum absolute position errors of Haulotte during the 2WDS mode on well-behaved path curvatures were generally less than 0.1 m (see figures 49 and 50), and the mean absolute errors were under of 0.05 m. While using both of the driving modes, 2WDS and 4WDS, the mean absolute errors were under of 0.2 m. In overall, the mean absolute errors in all of the simulations, excluding the steering saturation scenarios, were under 0.2 m. One of the bests path-following results of both study robots are presented in table 4. Furthermore, video material was also created for better, yet simple, visualization of some of the study results.⁷

Table 4: Results from path-following of both study robots.

Ponsse Caribou S10		Haulotte 16RTJ PRO	
Simulated and reference path			
			
Mean absolute position errors			
x [cm]	y [cm]	x [cm]	y [cm]
4.7	1.5	4.7	2.3

According to the authors in [32], real life experiments from path-following of a car, multiple times lighter than the study vehicles, provided results with a typical crosstrack RMS position error of under 0.1 m. Similar path-following controller implemented in [32] also won the DARPA Grand Challenge in 2005 (see subchapter 2.6). Furthermore, according

⁷ Results from autonomous path-following of the study robots (accessed on 29.06.2018):

<https://youtu.be/TF0MCzMuoB0>, <https://youtu.be/zTwpnlNJfFo>, <https://youtu.be/jL8CxCWkitY>

the paper [33], maximum constant positioning accuracy achieved with a robot, which was close to the same calibre as the study robots, was 0.1 m.

With the study's path-following controller and constant high and low-level controllers' gains, the accurate path-following could be maintained up to the near maximum velocity of the vehicles. Due to the Haulotte's limitation of maximum speed of 5.6 km/h, the constant gaining of its controllers proved to not be an issue. Even the high velocity path-following scenarios of Ponsse Caribou S10 proved that, at least under hydraulic/dynamic simulation environment, well-defined constant gain parameters provided accurate and well-behaved path-following results under well-designed path curvatures (as shown in figures 55 and 56). The selected controller proved to be effective also in returning to the path after sharp curve that causes steering saturation. When the steering saturated, the path-following controller adjusted the steering command to its maximum and the robots returned to the path after a short period of time, usually with a small oscillation of which magnitude depended on the sharpness of the curve and controller's gains.

One of the fundamental issues in this type of control formulation is lack of path parameters for the path generation progress for cubic Bezier curves. With the current path parameter normalization and velocity interpolation, the generation of the path is adjusted to strictly follow the generation speed provided for each part of the path. This discontinuity of the time derivatives also happens for the beginning of the tests. When the position errors grew, this caused the path-follower to increase velocity of the robot to catch the reference pose, even on a tight cornering situation. This could be seen at the steering saturation simulation cases conducted in the thesis.

During the implementation of the dynamic robot models, simplifications were made for the sake of rapid development. More realistic modelling of the hydraulic load sensing variable displacement pumps instead of constant, ideal pressure controlled pumps, might provide more realism to the dynamic robot models. Furthermore, more developed tire model and variation of the ground profile might be interesting features to further develop, since the current model of the Ponsse already contains all necessary degrees of freedom for moving on an uneven and rough terrain.

Other subjects to be discussed when moving from the simulation phase to testing the algorithms in real machines are localization accuracy and perception/communication delays. Under simulation environment, the localization accuracy can be considered to be ideal and the system delays were modelled only as a localization delay of 20 ms, which cannot be considered to be robustly achievable maximum delay while using real systems under real environments. Imprecise and noisy localization feedback can cause unexpected behaviour of the system, which may only be revealed by the procedure of testing the algorithms under real environments.

In the further, advanced path-following controllers and implementation of algorithms into actual robotic vehicles under real conditions are the main subjects of research. More advanced variable speed control with constrained open-loop velocity control and more intelligent property, where the path generator slows down the generation progress if the robot falls behind, are the key features in minimizing position and heading errors. Path-following control of the vehicles under real environments shall provide answers for the previously presented localization subject, and, furthermore, more deeply validate the obtained results of the study.

In conclusion, the study showed promising results in modelling and control of the path-following of heavy-duty vehicles by using the designed high-level control structure and implemented path-follower. Defining inverse kinematics based on the steering structure of the vehicle provides a chance for the path-following controller architecture to be generically designed independent of the vehicle's steering structures. Furthermore, reutilizing the designed dynamic robot models provides valuable possibilities for follow-up research and prototyping and observing the effects of new more advanced path-following control structures, before any real system implementations.

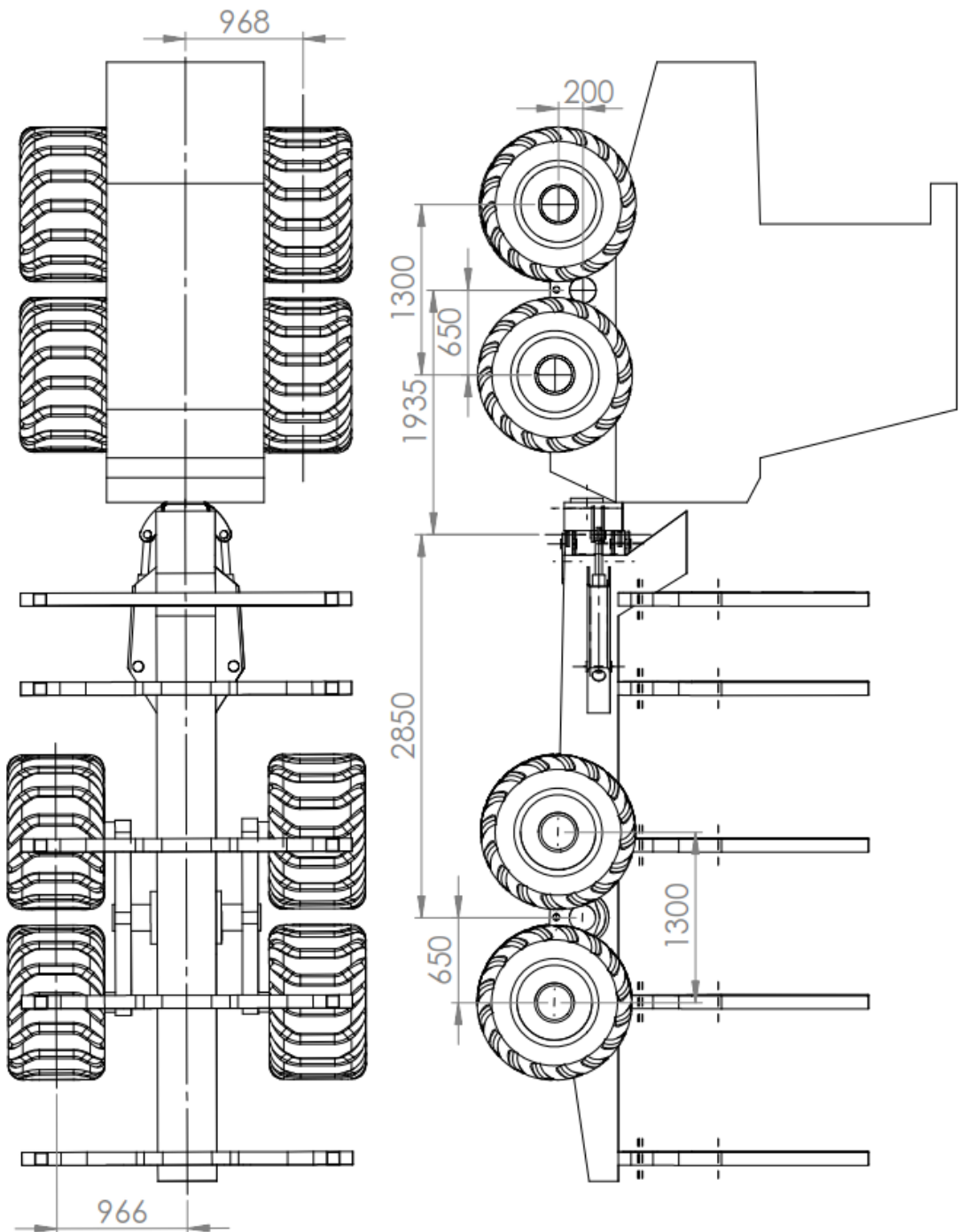
BIBLIOGRAPHY

- [1] R. Velazquez, A. Lay-Ekuakille, A Review of Models and Structures for Wheeled Mobile Robots: Four Case Studies, The 15th International Conference on Advanced Robotics, Tallinn, Estonia, 2011, pp. 524–529. Available (accessed on 19.04.2018): <https://www.researchgate.net/publication/241624194>
- [2] O. Miglino, H.H. Lund, S. Nolfi, Evolving Mobile Robots in Simulated and Real Environments, *Artificial Life*, Vol. 2, July 1995, pp. 417–434. Available (accessed on 19.04.2018): <https://www.mitpressjournals.org/doi/10.1162/artl.1995.2.4.417>
- [3] S. Scheduling, G. Dissanayake, E. M. Nebot, H. Durrant-Whyte, An experiment in autonomous navigation of an underground mining vehicle, *IEEE Transactions on Robotics and Automation*, Vol. 15, Iss. 1, 1999, pp. 85–95. Available (accessed on 31.05.2018): <https://ieeexplore.ieee.org/document/744605/>
- [4] C. Altafini, A Path-Tracking Criterion for an LHD Articulated Vehicle, *The International Journal of Robotics Research*, Stockholm, Sweden, 1999, pp. 435–441. Available (accessed on 31.05.2018): <http://users.isy.liu.se/en/rt/claal20/Publications/pathfIJRR.pdf>
- [5] K.Huhtala, Modelling of Hydrostatic Transmission – Steady State, Linear and Non-Linear Models, *Mechanical Engineering Series No. 123*, Tampere, Finland, 1996, 101 p.
- [6] J. Fonselius, Comparing Different Control Strategies of Hydrostatic Transmission System, *Mechanical Engineering Series No. 151*, Tampere, Finland, 2001, 83 p.
- [7] K.M. Lynch, F.C. Park, *Modern Robotics, Mechanics, Planning and Control*, University Printing House, Cambridge, United Kingdom, 2017, 528 p.
- [8] P. I. Corke, P. Ridley, Steering kinematics for a center-articulated mobile robot, *IEEE Transactions on Robotics and Automation*, Vol. 17, Iss. 2, 2001, pp. 215–218. Available (accessed on 31.05.2018): <https://ieeexplore.ieee.org/document/928568/>
- [9] R. Ghabcheloo, M. Hyvönen, Modeling and motion control of an articulated-frame-steering hydraulic mobile machine, 17th Mediterranean Conference on Control and Automation MED '09, Thessaloniki, Greece, 2009, pp. 92–97. Available (accessed on 11.12.2017): <https://ieeexplore.ieee.org/document/5164520/>

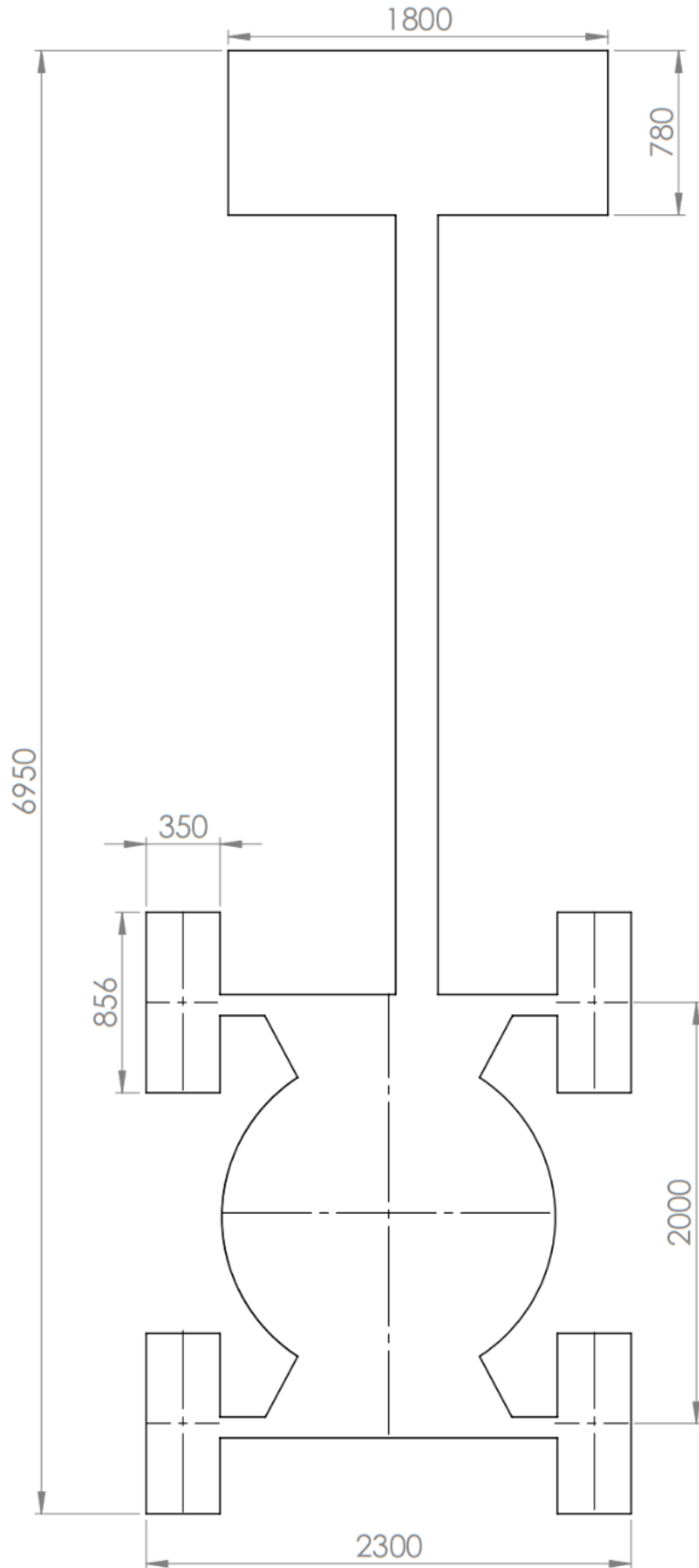
- [10] M. M. Aref, R. Ghabcheloo, A. Kolu, M. Hyvönen, K. Huhtala, J. Mattila, Position-based visual servoing for pallet picking by an articulated-frame-steering hydraulic mobile machine, 6th IEEE Conference on Robotics, Automation and Mechatronics (RAM), Manila, 2013, pp. 218–224. Available (accessed on 31.01.2018): <https://ieeexplore.ieee.org/document/6758587/>
- [11] M. F. Selekwa, J. R. Nistler, Path tracking control of four wheel independently steered ground robotic vehicles, 50th IEEE Conference on Decision and Control and European Control Conference, Orlando, FL, USA, 2011, pp. 6355–6360. Available (accessed on 24.04.2018): <https://ieeexplore.ieee.org/document/6160677/>
- [12] K. Huhtala, Mobilehydraulics, Course Handout, unpublished, Laboratory of Automation and Hydraulics Engineering, Tampere University of Technology, Tampere, Finland, 2018.
- [13] M. Hyvönen, Modeling of Fluid Power Components, Course Handout, unpublished, Intelligent Hydraulics and Automation, Tampere University of Technology, Tampere, Finland, 2015, 149 p.
- [14] B. Zardin, M. Borghi, F. Gherardini, N. Zanasi, Modelling and Simulation of a Hydrostatic Steering System for Agricultural Tractors, MDPI energies, Modena, Italy, 2018, pp. 1–20. Available (accessed on 24.04.2018): <http://www.mdpi.com/1996-1073/11/1/230>
- [15] J. Tirkkonen, Haulotte 16RTJ Pro Hydraulics Systems, unpublished, Laboratory of Automation and Hydraulics Engineering, Tampere University of Technology, Tampere, Finland, 2018, 59 p.
- [16] Miller, Steve (2017), Simscape Multibody Contact Forces Library (<https://www.mathworks.com/matlabcentral/fileexchange/47417>) MATLAB Central File Exchange. Retrieved on 18.12.2017.
- [17] Ponsse Oy, Ponsse Caribou S10 Owner’s Manual, unpublished, Laboratory of Automation and Hydraulics Engineering, Tampere University of Technology, Tampere, Finland, 2008.
- [18] N. H. Amer, H. Zamzuri, K. Hudha, Z.A. Kadir, Modelling and Control Strategies in Path Tracking Control for Autonomous Ground Vehicles: A Review of State of the Art and Challenges, Journal of Intelligent & Robotic Systems, Vol. 86, 2017, pp. 225–254. Available (accessed on 24.04.2018): <https://link.springer.com/article/10.1007/s10846-016-0442-0>

- [19] R. Wallace, A. Stentz, C. Thorpe, H. Moravec, W. Whittaker, T. Kanade, First Results in Robot Road-Following, Proceedings of the International Joint Conference on Artificial Intelligence, Los Angeles, California, USA, 1985.
- [20] O. Amidi, Integrated Mobile Robot Control, The Robotics Institute, Carnegie Mellon University, Pittsburgh, Pennsylvania, USA, 1990.
- [21] R.C Coulter, Implementation of the Pure Pursuit Path Tracking Algorithm, The Robotics Institute, Carnegie Mellon University, Pittsburgh, Pennsylvania, USA 1990.
- [22] J.S. Wit, Vector pursuit path tracking for autonomous ground vehicles, University of Florida, Florida, USA, 2000.
- [23] J.S. Wit, C.D. Crane, D. Armstrong, Autonomous ground vehicle path tracking, Journal of Robotic Systems, Vol. 21(8), 2004, pp. 439–449.
- [24] T. Hellström, O. Ringdahl, Follow the Past: a path-tracking algorithm for autonomous vehicles, Int. J. Vehicle Autonomous Systems, Vol. 4, Nos. 2-4, 2006, pp. 216–224.
- [25] G.M. Hoffmann, C.J. Tomlin, D. Montemerlo, S. Thrun, Autonomous Automobile Trajectory Tracking for Off-Road Driving: Controller Design, Experimental Validation and Racing, American Control Conference, 2007, pp. 2296–2301.
- [26] A. Ollero, B.C. Arrue, J. Ferruz, G. Heredia, F. Cuesta, F. Lopez-Pichaco, C. Nogales, Control and perception components for autonomous vehicle guidance. Application to the ROMEO vehicles, Control Engineering Practice, Vol. 7, Iss. 10, 1999, pp. 1291–1299. Available (accessed on 24.04.2018): <https://www.sciencedirect.com/science/article/pii/S096706619900091X>
- [27] A. Ollero, A. Garcia-Cerezo, J.L. Martinez, Fuzzy supervisory path tracking of mobile reports, Control Engineering Practice, Vol. 2, Iss. 2, 1994, pp. 313–319.
- [28] M.K. Agoston, Computer Graphics and Geometric Modelling: Implementation & Algorithms, Springer, London, United Kingdom, 2005, 907 p.
- [29] 1004-40TW Diesel Engine, Perkins, website. Available (accessed on 31.05.2018): <https://www.perkinsqm.ca/en/1000-series/1004-40tw-engine>
- [30] M. Hyvönen, J. Vilenius, A. Vuohijoki, K. Huhtala, Mathematical Model of the Valve Controlled Skid Steered Mobile Machine, 2nd International Conference on Computational Methods in Fluid Power, FPNI, 2006, 10 p.

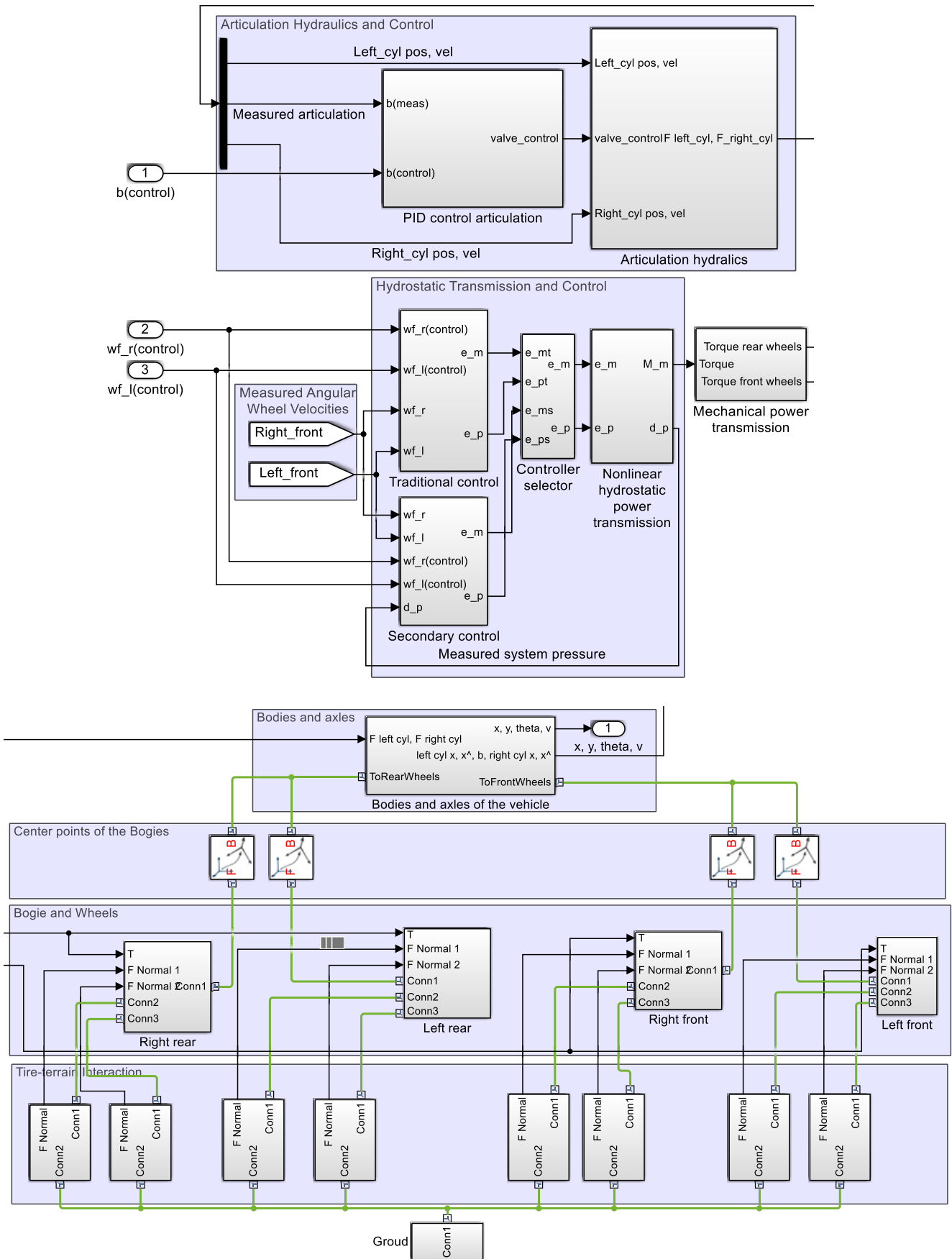
- [31] J. Vilenius, Characteristics of Valve Controlled Hydraulic Power Transmission in Teleoperated Skid Steered Mobile Machine, Tampere University of Technology, Tampere, Finland, 2007, 88 p.
- [32] G.M. Hoffmann, C. J. Tomlin, M. Montemerlo, S. Thrun, Autonomous Automobile Trajectory Tracking for Off-Road Driving: Controller Design, Experimental Validation and Racing, American Control Conference, New York City, USA, 2007, 6 p.
- [33] M.M. Aref, R. Chabcheloo, A. Kolu, J. Mattila, A Multistage Controller with Smooth Switching for Autonomous Pallet Picking, IEEE International Conference on Robotics and Automation (ICRA), Stockholm, Sweden, 2016, 8 p.

APPENDIX A: PONSSE CARIBOU S10 MAIN DIMENSIONS

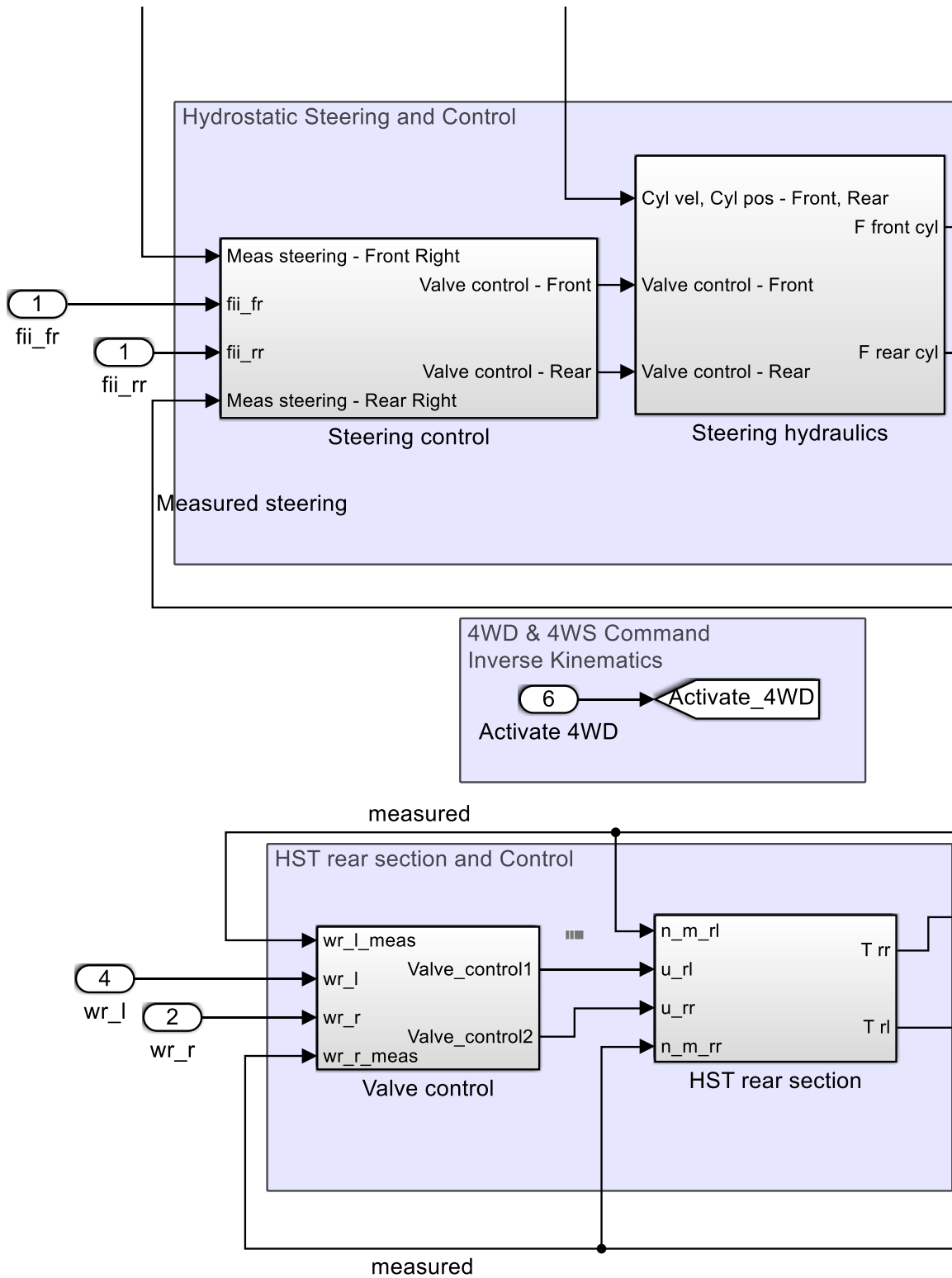
APPENDIX B: HAULOTTE 16RTJ PRO MAIN DIMENSIONS

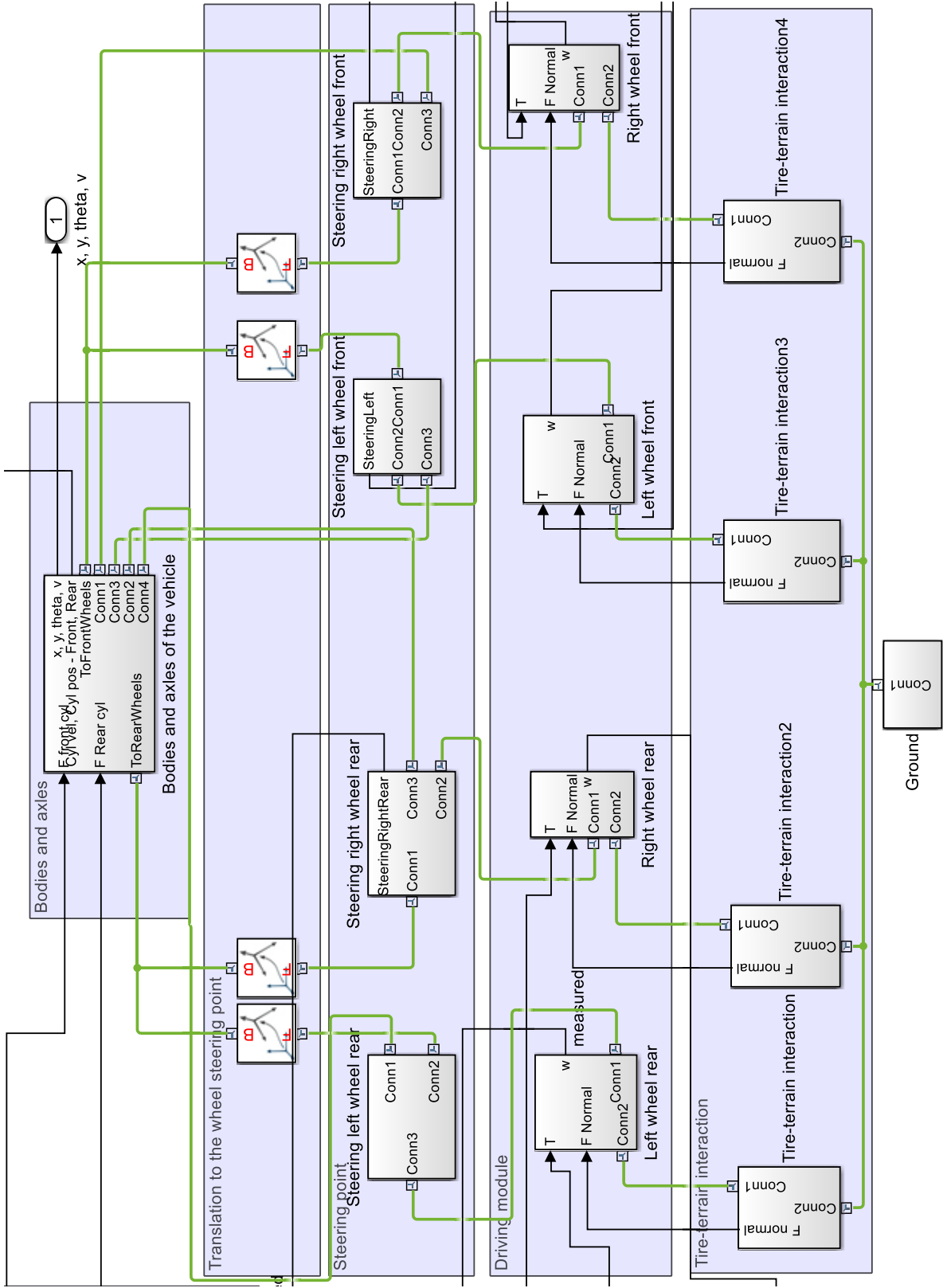


APPENDIX C: PONSSÉ CARIBOU S10 HIGH-LEVEL MODEL STRUCTURE



APPENDIX D: HAULOTTE 16RTJ PRO HIGH-LEVEL MODEL STRUCTURE





APPENDIX E: PONSSE CARIBOU S10 HST CALCULATIONS

Initial values:

$$\begin{aligned}
 V_{gpm_{max}} &:= 90 \text{ cm}^3 & V_{gm_{max}} &:= 160 \text{ cm}^3 & \eta_{vp} &:= 0.96 & \eta_{tp} &:= 0.8 \\
 P &:= 91 \text{ kW} & \eta_{ng} &:= 0.8 & \eta_{vm} &:= 0.95 & \eta_{hmm} &:= 0.91 \\
 n_p &:= 2200 \frac{1}{\text{min}} & \Delta p_{max} &:= 340 \text{ bar} & n_{m_{max}} &:= 4300 \cdot \frac{1}{\text{min}} \\
 r_{wheel} &:= \frac{1.150 \text{ m}}{2} = 0.575 \text{ m} & & & v_{max} &:= 27 \frac{\text{km}}{\text{hr}}
 \end{aligned}$$

Traditional control based calculations

Point 1

$$\begin{aligned}
 Q_{p1} &:= \frac{P}{\Delta p_{max}} \cdot \eta_{tp} = 0.0021412 \frac{\text{m}^3}{\text{s}} \\
 V_{pp1} &:= \frac{Q_{p1}}{n_p \cdot \eta_{vp}} = 60.829 \text{ cm}^3 \\
 T_{m1} &:= \frac{V_{gm_{max}} \cdot \Delta p_{max}}{2 \cdot \pi} \cdot \eta_{hmm} = 787.881 \text{ N} \cdot \text{m} \\
 n_{m1} &:= \frac{Q_{p1} \cdot \eta_{vm}}{V_{gm_{max}}} = 12.713 \frac{1}{\text{s}} \\
 Q_{max} &:= V_{pp1} \cdot n_p \cdot \eta_{vp} = 128.471 \frac{\text{l}}{\text{min}}
 \end{aligned}$$

In speed area of 0-27 km/h, gear ratio is reduced with coefficient 1/3 compared to low speed area of 0-8 km/h, where maximum traction force according vehicle's datasheet is 130 kN. Therefore, maximum traction force in high speed area respectfully is:

$$\begin{aligned}
 F_{max} &:= \frac{130 \text{ kN}}{3} = 43.333 \text{ kN} \\
 i_g &:= \frac{F_{max} \cdot r_{wheel}}{T_{m1} \cdot \eta_{ng}} = 39.531 \\
 F_{max} &:= \frac{T_{m1} \cdot i_g \cdot \eta_{ng}}{r_{wheel}} = 43.333 \text{ kN} \\
 v_{maxF} &:= \frac{2 \cdot \pi \cdot n_{m1} \cdot r_{wheel}}{i_g} = 4.183 \frac{\text{km}}{\text{hr}}
 \end{aligned}$$

Point 2

$$Q_{p2} := V_{gpmax} \cdot n_p \cdot \eta_{vp} = 0.003168 \frac{m^3}{s}$$

$$p_2 := \frac{P \cdot \eta_{tp}}{Q_{p2}} = 229.798 \text{ bar}$$

$$n_{mmax} := \frac{v_{max} \cdot i_g}{2 \cdot \pi \cdot r_{wheel}} = 82.064 \frac{1}{s}$$

$$V_{gmmin} := \frac{Q_{p2} \cdot \eta_{vm}}{n_{mmax}} = 36.674 \text{ cm}^3$$

$$T_{m2} := \frac{V_{gmmin}}{2 \cdot \pi} \cdot p_2 \cdot \eta_{hm} = 122.057 \text{ N} \cdot \text{m}$$

$$F_2 := \frac{T_{m2} \cdot i_g \cdot \eta_{ng}}{r_{wheel}} = 6.713 \text{ kN}$$

$$v_2 := \frac{2 \cdot \pi \cdot n_{mmax} \cdot r_{wheel}}{i_g} = 27 \frac{km}{hr}$$

Theoretical maximum velocity with maximum displacements of pump and motor, no losses, and with selected diesel engine rotation speed of 2200 rpm:

$$n_{mv} := \frac{V_{gpmax}}{V_{gmmax}} \cdot n_p = 20.625 \frac{1}{s}$$

With gear ratio of 90:

$$v_{mv} := \frac{2 \cdot \pi \cdot n_{mv} \cdot r_{wheel}}{90} = 0.828 \frac{m}{s}$$

With gear ratio of 40:

$$v_{mv} := \frac{2 \cdot \pi \cdot n_{mv} \cdot r_{wheel}}{40} = 1.863 \frac{m}{s}$$

Theoretical displacement ratio of the hydraulic motor at vehicle's full speed:

$$e_{m_vmax} := \frac{V_{gmmin}}{V_{gpmax}} = 0.229$$

APPENDIX F: OPEN LOOP CONTROL RESULTS

Scenario 1: Straight Drive

Inputs			Outputs		
	$\dot{\phi} \left[\frac{rad}{s} \right]$	$v \left[\frac{m}{s} \right]$	$u_{rl} \left[\frac{rad}{s} \right]$	$u_{rr} \left[\frac{rad}{s} \right]$	$R [m]$
Ponsse Caribou S10					
Calculated	0	0.5	0.87	0.87	-
Simulated	0	0.5	0.87	0.87	-
Calculated	0	2	3.478	3.478	-
Simulated	0	2	3.479	3.479	-
Calculated	0	5	8.696	8.696	-
Simulated	0	5	8.701	8.701	-
Haulotte 16RTJ PRO					
Calculated	0	0.3	0.701	0.701	-
Simulated	0	0.3	0.701	0.701	-
Calculated	0	0.5	1.17	1.17	-
Simulated	0	0.5	1.17	1.17	-
Calculated	0	0.65	1.52	1.52	-
Simulated	0	0.64	1.50	1.50	-

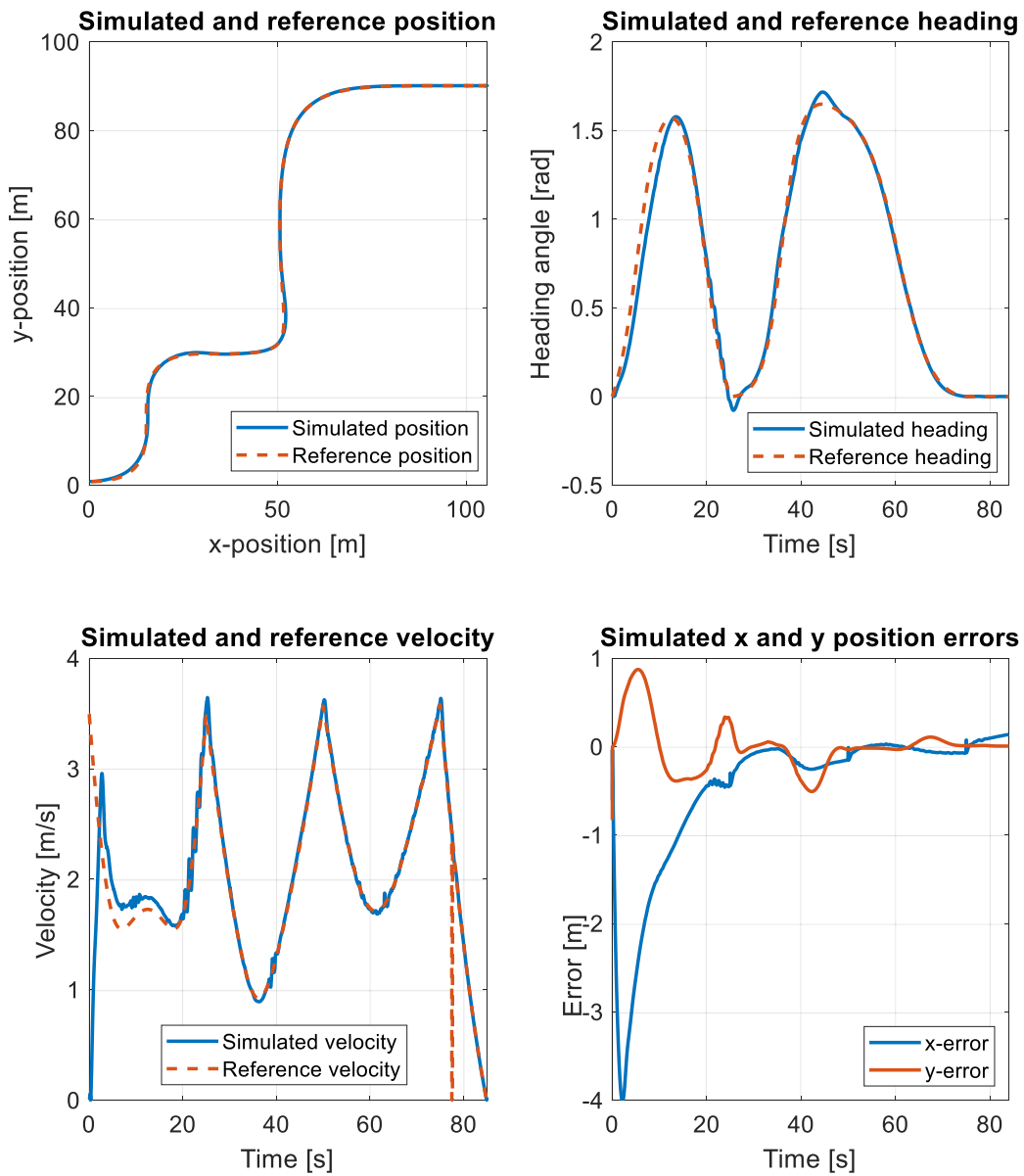
Scenario 2: Turn Left

Inputs			Outputs				
	$\dot{\phi} \left[\frac{rad}{s} \right]$	$v \left[\frac{m}{s} \right]$	$u_{rl} \left[\frac{rad}{s} \right]$	$u_{rr} \left[\frac{rad}{s} \right]$	φ / β [rad]	R [m]	
Ponsse Caribou S10					β [rad]		
Calculated	0.10	2.0	3.322	3.634	0.238	20.00	
Simulated	0.10	2.0	3.331	3.631	0.241	20.83	
Calculated	0.30	6.0	9.967	10.902	0.238	20.00	
Simulated	0.30	6.0	9.952	10.841	0.233	20.79	
Calculated	0.16	1.0	1.49	1.99	0.705	6.4	
Simulated	0.16	1.0	1.54	1.94	0.704	7.7	
Haulotte 16RTJ PRO					φ_{fr} [rad]	φ_{fl} [rad]	
Calculated	0.10	0.50	0.94	1.40	0.32	0.46	5.0
Simulated	0.10	0.50	0.96	1.40	0.32	0.39	5.4
Calculated	0.03	0.20	0.40	0.54	0.26	0.34	6.7
Simulated	0.03	0.20	0.39	0.54	0.26	0.29	6.9
Calculated	0.1	0.3	0.47	0.93	0.25	0.46	3.0
Simulated	0.1	0.3	0.53	0.93	0.25	0.29	3.6

Scenario 3: Turn Right

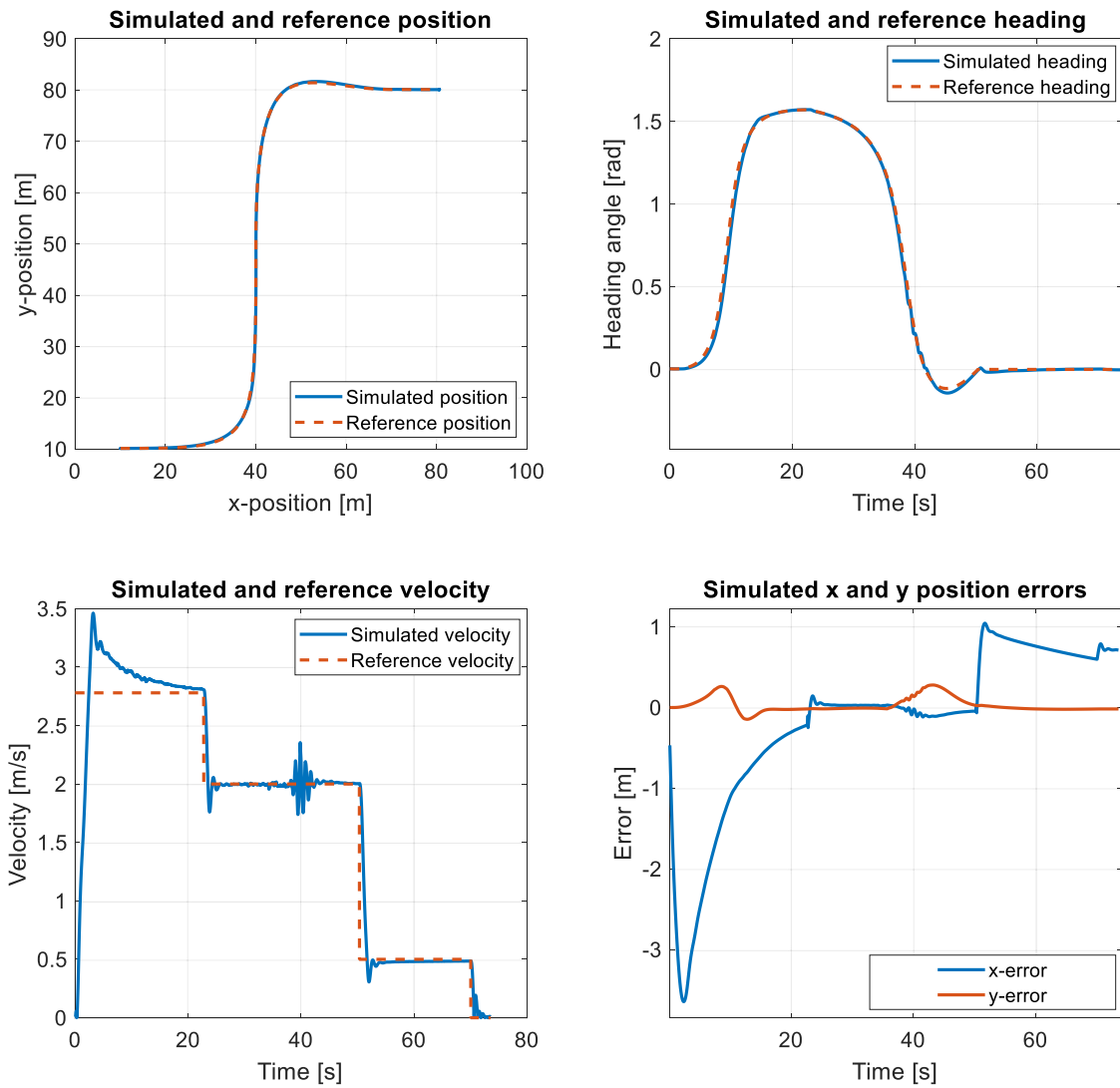
Inputs			Outputs				
	$\phi \left[\frac{rad}{s} \right]$	$v \left[\frac{m}{s} \right]$	$u_{rl} \left[\frac{rad}{s} \right]$	$u_{rr} \left[\frac{rad}{s} \right]$	β [rad]	R [m]	
Ponsse Caribou S10					β [rad]		
Calculated	-0.1	1	1.895	1.583	-0.4697	10	
Simulated	-0.1	1	1.883	1.593	-0.4701	10.86	
Calculated	-0.1	2	3.634	3.322	-0.238	20	
Simulated	-0.1	2	3.628	3.334	-0.2351	21.3	
Calculated	-0.2	3	5.529	4.906	-0.316	15	
Simulated	-0.2	3	5.437	4.970	-0.334	15.1	
Haulotte 16RTJ PRO					φ_{fr} [rad]	φ_{fl} [rad]	
Calculated	-0.025	0.6	1.46	1.35	-0.087	-0.080	24
Simulated	-0.025	0.6	1.46	1.35	-0.087	-0.075	25.5
Calculated	-0.05	0.5	1.28	1.05	-0.218	-0.180	10
Simulated	-0.05	0.5	1.28	1.05	-0.218	-0.194	9.9
Calculated	-0.075	0.3	0.87	0.53	-0.584	-0.382	4
Simulated	-0.075	0.3	0.87	0.53	-0.584	0.459	3.77

APPENDIX G: CLOSED LOOP PATH-FOLLOWING RESULTS OF PONSSE CARIBOU S10



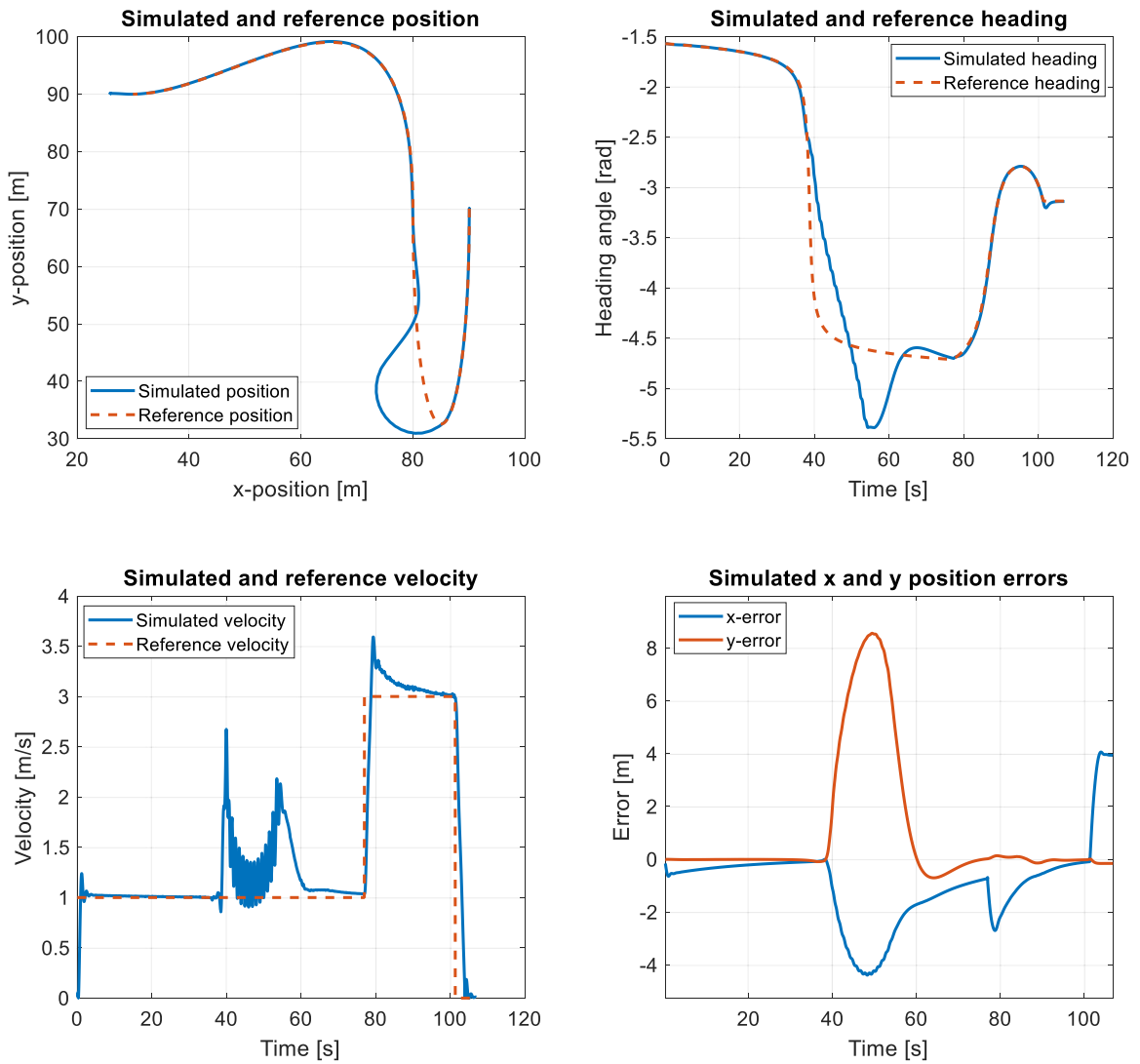
Case Analysis

At the start of the simulation, the robot was instantly asked to accelerate to high velocity and the reference path is generated too fast, which can be seen as a rising x error at the beginning. The robot accelerates as fast as possible and PF controller adjusts the velocity to be higher than current reference, until the measured errors are driven close to zero at the time point of 20 s. After this, the PF controller adjusts the velocity and heading rate of the robot accordingly till the end of the path, while the maximum magnitudes of the position errors are less than 0.40 m.



Case Analysis

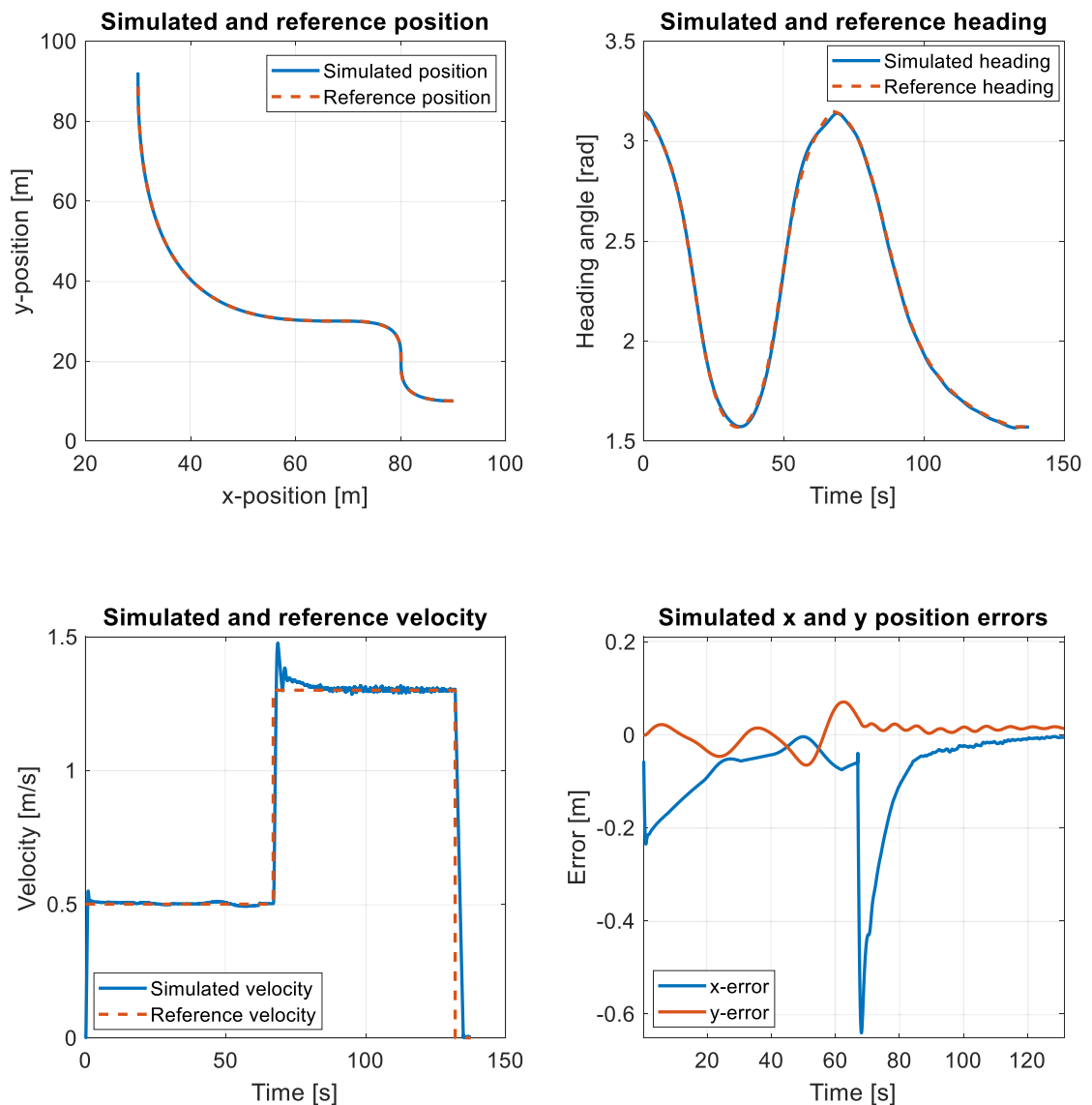
A velocity command of 3 m/s is given at the start of the path generation, which can be seen as fast rising x error and fast acceleration of the robot. The robot gains speed higher than the reference until the position errors are decreased close to zero. From this point forward, the velocity commands are being varied and the robot succeeds in accurate path-following until the end, where the x error rises to a value of 1 m because of too aggressive deceleration command from 2 to 0.5 m/s. Normal y position error can be seen to be less than 0.2 m during the whole simulation.



Case Analysis

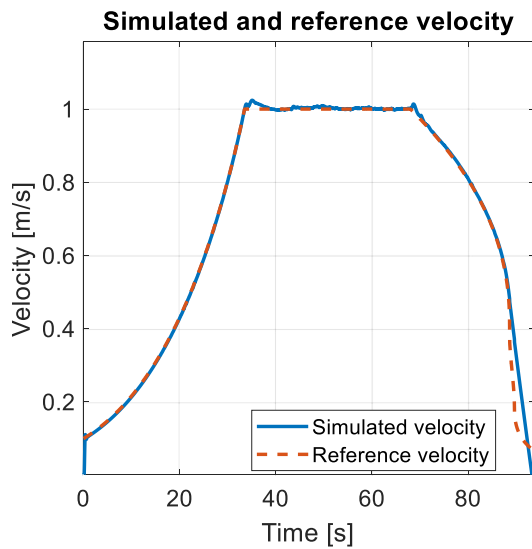
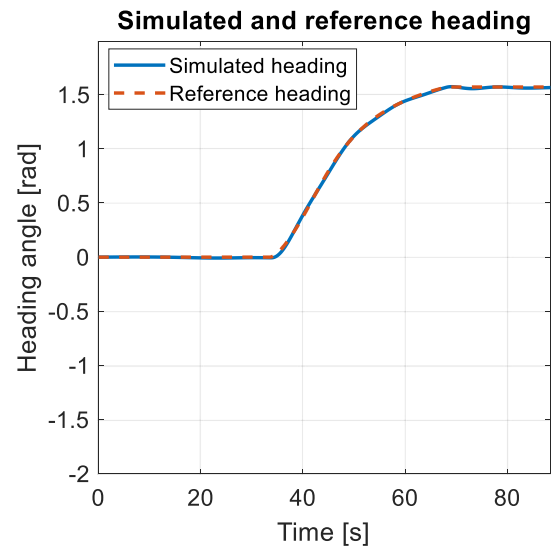
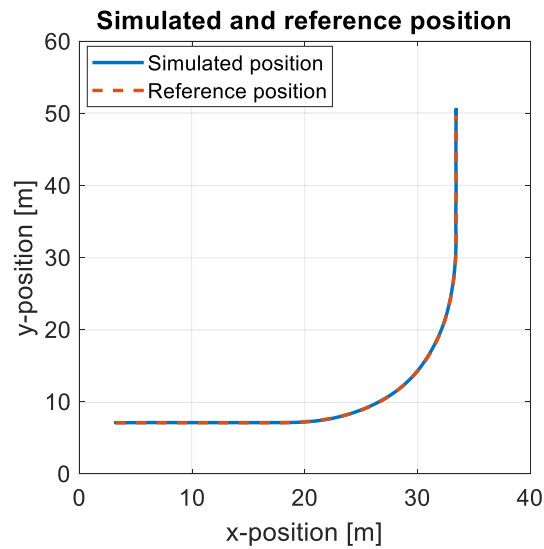
This case is simulated for observing the effects caused by steering saturation. At first, the robot is accurately following the path with a constant velocity of 1 m/s. At the time point of 40 s, the designed path curvature proves to be too sharp for the structural limitations of the robot, thus the steering will saturate to the maximum. The robot steers with maximum angle until point of [75, 43], approximately. When the steering is no longer limited, the PF controller adjusts the velocity and heading of the robot accordingly and a smooth returning to the path-following can be seen approximately at point [80, 55]. From this point forward, the robot continues accurate path-following until the end, where the deceleration command is set to be too fast and the robot manages to stop only after braking of 4 m over the final path point.

APPENDIX H: CLOSED LOOP PATH-FOLLOWING RESULTS OF HAULOTTE 16RTJ PRO



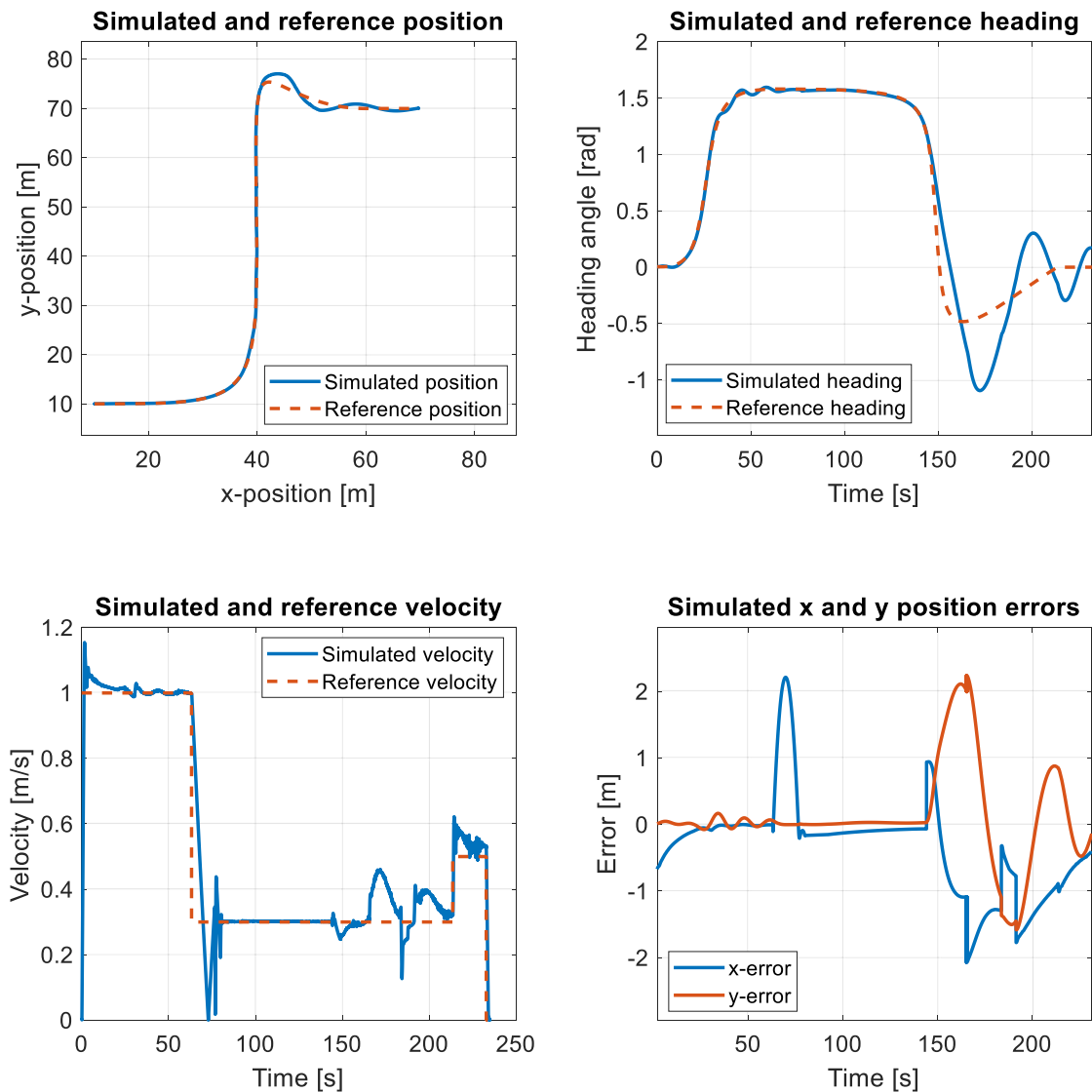
Case Analysis

The path generation is started with the reference velocity of 0.5 m/s. Due to the low velocity, the longitudinal x error during the start does not exceed magnitude of 0.25 m. During the reference velocity change at the time point of 70 s, the magnitude of longitudinal x error can be seen to rise, until the PF controller manages to accelerate the vehicle to gain the reference and drive the position error close to zero. The normal error y is less than 0.05 m during the whole simulation.



Case Analysis

In this scenario, the velocity profile of the vehicle is interpolated with respect to the path parametrization. With these smooth reference velocity transitions, the both position errors during a simple one turn scenario are less than 0.11 m. Compared to the other results, the major advance of this kind of velocity interpolation results in lower longitudinal x error values.



Case Analysis

This scenario was originally designed to observe the functionality of the 4WDS activation. By using the mode, the robot is capable to turn in sharp turns with better accuracy due to the smaller minimum turning radius of the robot. From the start until point of [40,77] the path-following of the robot is accurate with lateral error less than 0.1 m. From this point forward, the designed path curvature was too sharp for the robot to handle. Even with the use of 4WDS, the lateral error increased to a value of 2.1 m, until the steering was no longer saturated. Next, the robot tried to reduce the lateral error too aggressively, which lead to an oscillation with an approximate error amplitude of 1 m. However, the PF controller managed to stabilize the steering of the robot in time, and to accurately stop at the desired ending point of the path with longitudinal x error less than 0.5 m.